

Electronic Thesis and Dissertation Repository

12-12-2012 12:00 AM

Synthesis and characterization of copper nanoparticles and copper-polymer nanocomposites for plasmonic photovoltaic applications

Sabastine Chukwuemeka Ezugwu
The University of Western Ontario

Supervisor
Prof. Giovanni Fanchini
The University of Western Ontario

Graduate Program in Physics

A thesis submitted in partial fulfillment of the requirements for the degree in Master of Science

© Sabastine Chukwuemeka Ezugwu 2012

Follow this and additional works at: <https://ir.lib.uwo.ca/etd>

 Part of the [Condensed Matter Physics Commons](#)

Recommended Citation

Ezugwu, Sabastine Chukwuemeka, "Synthesis and characterization of copper nanoparticles and copper-polymer nanocomposites for plasmonic photovoltaic applications" (2012). *Electronic Thesis and Dissertation Repository*. 1025.

<https://ir.lib.uwo.ca/etd/1025>

This Dissertation/Thesis is brought to you for free and open access by Scholarship@Western. It has been accepted for inclusion in Electronic Thesis and Dissertation Repository by an authorized administrator of Scholarship@Western. For more information, please contact wlsadmin@uwo.ca.

SYNTHESIS AND CHARACTERIZATION OF COPPER NANOPARTICLES AND
COPPER-POLYMER NANOCOMPOSITES FOR PLASMONIC PHOTOVOLTAIC
APPLICATIONS

by

Sabastine C. Ezugwu

Graduate Program in Physics

A thesis submitted in partial fulfillment
of the requirements for the degree of
Master of Physics

The School of Graduate and Postdoctoral Studies
The University of Western Ontario
London, Ontario, Canada

© Sabastine C. Ezugwu 2013

THE UNIVERSITY OF WESTERN ONTARIO
School of Graduate and Postdoctoral Studies

CERTIFICATE OF EXAMINATION

Supervisor

Examiners

Dr. Giovanni Fanchini

Dr. Peter Simpson

Dr. Michael Cottam

Dr. Mark Workentin

The thesis by

Sabastine Chukwuemeka Ezugwu

entitled:

**SYNTHESIS AND CHARACTERIZATION OF COPPER
NANOPARTICLES AND COPPER-POLYMER NANOCOMPOSITES FOR
PLASMONIC PHOTOVOLTAIC APPLICATIONS**

is accepted in partial fulfillment of the
requirements for the degree of
Master of Physics

Date

Chair of the Thesis Examination Board

Abstract

Deposition techniques for the fabrication of metal nanostructures influence their morphological properties, which in turn control their optical behavior. Here, copper nanoparticles (np-Cu's) were grown using a deposition system that was specifically set up during this work, and is based on a radio frequency (RF) sputtering source that can operate at high temperature and under bias voltage. The effect of deposition conditions (RF power, chamber pressure and substrate bias voltage) on RF sputtered np-Cu's using RF sputtering has been studied. The study included a comparison between the morphological and optical properties of as-grown np-Cu's and thermally treated samples. The characterization of np-Cu's is carried out by atomic force microscopy, UV-visible transmission spectrophotometry, scanning electron microscopy and scanning near field optical microscopy (SNOM) techniques. The results of the experiment showed that the combined effects of low RF power (25 W – 75 W), high chamber pressure (17 Pa – 23 Pa) and substrate DC bias voltage (300 V – 400 V) are required for obtaining dispersed np-Cu's. Under these conditions, copper nanoparticles grow by aggregation of initial island nuclei due to a reduction in sputtering rate. Significantly, higher dispersed np-Cu's are obtained when a set of samples grown at 25 W and 33 W RF power is subjected to thermal treatment in an oxygen-free glove box. Optical properties of np-Cu's show improvement in the visible region (535nm – 580 nm) related to transmission enhancement in as-deposited samples and plasmonic enhancement in thermally treated ones. Furthermore, an approach to determine the position of the np-Cu induced scattered wave was explored using SNOM (x, z) measurements. In bare np-Cu's the path length of the scattered wave is further from the np surface, measured orthogonally. We demonstrated experimentally a method that uses an SiO₂ thin film as a spacer to broaden the scattered wave up to 500 nm from the np-Cu/SiO₂ composite surface. The study provides an improved insight that helps to understand the physical mechanisms that may hinder the expected performance in plasmonic solar cells. With these results, the potential of incorporating np-Cu's in plasmonic thin film solar cell structures looks very promising.

Keywords:

Copper nanoparticle, sputtering, optical properties, scanning near field optical microscopy

Acknowledgement

Firstly, I would like to express my gratitude to my supervisor, Prof. Fanchini Giovanni for his support throughout this project and especially during the analysis of results. Prof. Giovanni not only provides direction, he is also very generous with his time in attending to and offering useful discussions.

I would like to thank the members of Giovanni's group: M. Shafiq Ahmed, Reg Bauld, Arash Akbari Sharbaf and Faranak Sharif, all Ph.D students working under Prof. Giovanni. I would like to thank all these people for their insightful views and help in time of difficulties.

Many thanks to Prof. Kanthi Kaluarachchi, for words of encouragement.

Acknowledgements are also due to members of my Supervisory Committee; Prof. Peter Simpson and Prof Lyudmila Goncharova. Many thanks for your candid advice.

Similarly, I would like to acknowledge the foundation to my graduate studies laid by Dr. F.I. Ezema and all the support received from Dr. P.U. Asogwa, both of The University of Nigeria, Nsukka. I am indebted to both of you for the progress and achievement in my academic pursuit.

Many thanks to 3M Canada Inc. for the provision of some of the materials used for the composite studies reported in chapter 5 of this thesis.

Finally and most importantly, I would like to express my utmost gratitude to my family for their love, prayer and support especially, my lovely wife, Angela. I love and cherish you, my Angel!

Table of Contents

CERTIFICATION OF EXAMINATION.....	ii
Abstract.....	iii
Acknowledgment.....	iv
Table of Contents.....	v
List of Tables.....	ix
List of Figures.....	x
Chapter 1.....	1
1 Optical properties and application of metallic nanoparticles.....	1
1.1 Plasmons in metals and metallic nanostructures	2
1.1.1 Bulk plasmons.....	2
1.1.2 Surface plasmons.....	4
1.1.3 Localized surface plasmons.....	10
1.2 Conclusions and Thesis overview.....	13
1.3 References.....	14
Chapter 2.....	16
2 Sputtering operation for nanoparticles deposition.....	16
2.1 Introduction.....	16
2.2 Sputtering deposition technique.....	16
2.2.1 RF Sputter Deposition from conducting target.....	17

2.2.2 RF Sputter Deposition from insulating target.....	20
2.2.3 Nucleation of metallic nanoparticles by sputtering.....	21
2.3 Introduction of Argon in the growth chamber.....	24
2.4 Substrate bias voltage.....	26
2.5 Experimental facility developed for this project.....	27
2.6 Conclusion.....	33
2.7 References.....	33
Chapter 3.....	35
3. Morphological and Optical properties of copper nanoparticles obtained from radio frequency sputtering	35
3.1 Deposition and protection of copper nanoparticles.....	35
3.1.1 Sample Stage.....	35
3.1.2 Preparation for copper nanoparticle deposition.....	36
3.1.3 Variation of process parameters and deposition of copper nanoparticles.....	37
3.1.4 Energy dispersive x-ray spectroscopy measurements.....	39
3.2: Characterization equipment.....	40
3.2.1 Atomic force microscopy	40
3.2.2 UV-VIS transmission spectrophotometry	43
3.3 Results and discussion on dispersed and semi-continuous copper nanoparticles.....	44
3.3.1 Determination of mean particle size and area fraction in dispersed and semi-continuous copper nanoparticles.....	44

3.3.2 Optical transmittance of semi-continuous copper nanoparticles.....	50
3.4 Properties of thermally treated copper nanoparticles.....	53
3.4.1 Parametric study as a function of treatment temperature.....	53
3.4.2 Parametric study as a function of treatment time.....	56
3.4.3 Transmittance of thermally treated copper nanoparticles.....	58
3.5 Properties of thermally treated copper nanoparticles grown at different RF power.....	61
3.6. Conclusion.....	64
3.7 References.....	65
Chapter 4.....	67
4 Scanning near field optical studies of copper nanoparticles.....	67
4.1 Scanning near field optical microscopy	67
4.2 The Witec Alfa 300S SNOM system.....	69
4.3 Role of (X, Z) SNOM images in designing np-Cu for plasmonic solar cell applications.....	71
4.4 Results and Discussion.....	73
4.5 Properties of np-Cu/SiO ₂ nanocomposites.....	80
4.6 Concluding remarks.....	87
4.7 References.....	88
Chapter 5.....	90

5 Electro-optical properties of metal- polymer and polymer-polymer nanocomposites.....	90
5.1 Graphite nanosheet with embedded copper nanoparticles.....	90
5.1.1 Preparation of nanocomposite of Graphite nanosheet and copper nanoparticles....	90
5.1.2 Morphology and composition of Graphite nanosheets with embedded copper nanoparticles	92
5.1.3 Measured Optical spectra of Graphite nanosheets with embedded copper nanoparticle.....	96
5.1.4 Electrical characterization of Graphite nanosheets with embedded copper nanoparticles.....	97
5.2 Properties of a Poly(3,4-thylenedioxythiophene):poly (styrenesulfonate) composite medium with graphene nanoplatelet inclusions.....	98
5.2.1 The spin coating operation and sample characterization.....	98
5.2.2 Morphology characterization of PEDOT:PSS/TCF nanocomposites.....	99
5.2.3 Optical properties of PEDOT:PSS composite medium with graphene nanoplatelet inclusion.....	104
5.2.4 Electrical characterization of the nanocomposite of PEDOT:PSS and graphene nanoplatelet inclusion.....	107
5.3 Conclusion.....	108
5.4 References.....	109
Chapter 6.....	110
6.1 Conclusions and Future work.....	110
C.V.....	113

List of Tables

Table 3.1: Sputtering parameters for deposition at different RF powers	37
Table 3.2: Sputtering parameters for deposition at different substrate bias voltages	38
Table 3.3: Sputtering parameters for deposition at different argon flow rates.....	38
Table 3.4: Properties of contact, tapping and non –contact modes of AFM configuration.....	42
Table 3.5: Sputtering parameters for samples to be annealed under different environment.....	55
Table 3.6: Average particles diameter and area fraction of np- Cu annealed in the glove box at 300°C and 400°C for 1 hour.....	56
Table 4.1: Weight and atomic % of elements observed from the EDX for SiO ₂ sputtered on Si (100) for 2 hrs.....	85
Table 4.2: Weight and atomic % of elements observed from the EDX spectra for SiO ₂ sputtered on Si (100) for 4 hrs.....	85
Table 5. 1: The elemental composition of bare glass substrate, np-Cu and graphite nanosheet/np-Cu nanocomposite obtained from EDX analysis.....	94

List of Figures

Fig. 1.1: Reflectance of selected metals as a function of wavelength.....4

Fig.1.2: Propagation of electromagnetic wave at an interface between metal and dielectric media with relative dielectric constants $\epsilon_m(\omega)$ and ϵ_d respectively.....6

Fig. 1.3: Schematic of (a) exponential dependence of the field intensity on the distance away from the interface, (b) surface EM wave propagating at a metallic and dielectric interface with different dielectric constants and.....7

Fig. 1.4: Plot of the dispersion relation for light propagating in vacuum and for plasmonic waves propagating along a metallic surface.....9

Fig.1.5: Schematic depiction of influence of external light field on randomly oriented charges in a metallic nanoparticle. The incident electromagnetic wave excites charge separation to create an electric dipole.....10

Fig.2.1: Schematic illustration of the fundamental principles of sputtering.....17

Fig.2.2: Schematic of RF sputtering assembly, used in our project, including RF power generator, capacitive matching network, coaxial cable for RF power transfer, sputter vacuum chamber and DC voltage power supply (used in some of the depositions).....18

Fig. 2.3: Collision event arising from ions-target atoms interaction. Onset of cascade starts with the near surface atoms.....20

Fig. 2.4: Variation of film thickness against the deposition time to determine the sputtering rate of our RF deposition system from an insulating target.....21

Fig. 2.5: Schematic diagram of three heterogeneous growth modes described as (a) Frankvan der Merwe (b) Volmer-Weber and (c) Stranski-Krastanov.....22

Fig. 2.6: Schematic of the deposition system, showing the possible orientation of sample stage relative to the target.....23

Fig. 2.7: AFM images of np-Cu's on Si substrate showing morphological evolution for three different sputtering times of (a) 1 min, (b) 3 min. and (c) 5 min deposited with constant RF power.....	24
Fig. 2.8: Schematic of the flow meter used for our experiment.....	25
Fig. 2.9: Picture of the mass flow controller used to control argon flow rate during RF deposition.....	25
Fig. 2.10: Schematic representation of the three regions in an RF deposition chamber and the voltage close to the target V_{sh} , self-bias voltage on the sample V_{sb} and the external bias voltage V_b	26
Fig. 2.11 Picture showing an overview of the experimental facility used for our project.....	27
Fig. 2.12 Picture showing a close view of the deposition chamber used for our project.....	28
Fig. 2.13: Picture of the basic components of our sputtering system that includes the matching network, tuning network, RF power supply and the sputtering cathode.....	29
Fig. 2.14: Picture of the deposition apparatus showing a close view of the DC bias power supply, cold cathode gauge, mechanical vacuum pump, Variac and isolation transformer.....	30
Fig. 2.15: Schematic of isolation transformer showing the connection to grid power and resistive heater.....	31
Fig. 2.16: Picture of Trace Oxygen Analyzer (left) and Computer monitor interfaced with the Glove box.....	32
Fig.3.1: Schematic representation of (a) regular and (b) perforated sample stages that can be mounted in the deposition chamber.....	36
Fig. 3.2: Variation of sputtering chamber pressure with the argon flow rate.....	39

Fig. 3.3: EDX spectral showing the composition of np-Cu sputtered on Si substrates for the case of (a) sample protected in the glove box, (b) samples exposed to oxidation environment for 24 hours prior to the analysis. (c) Comparison of (a) and (b).....	40
Fig. 3.4: Schematic of AFM during operation, with control and feedback mechanisms.....	41
Fig. 3.5: Atomic interaction forces between the AFM tip and the sample surface, which define the modes of AFM operation into contact, non-contact and tapping modes.....	41
Fig.3.6: Schematic diagram of a spectrophotometer.....	44
Fig. 3.7: Treated AFM topographic image of np-Cu deposited in constant RF power at different chamber pressure of (a) 9, (b) 12, (c)15, (d) 17, (e) 21 and (f) 23 Pa.....	45
Fig.3.8: Size dispersion of np-Cu's deposited in constant RF power at different chamber pressures of (a) 9, (b) 12, (c)15, (d) 17, (e) 21 and (f) 23 Pa.....	46
Fig. 3.9: Average diameter and out of plane growth height of np-Cu's obtained from AFM images for np-Cu's sputtered at constant RF power and different chamber pressures.....	47
Fig. 3.10: AFM images showing semi-continuous np-Cu's deposited with different RF power of (a) 33 W, (b) 55 W, (c) 75 W, (d) 100 W and (e) 120 W.....	48
Fig. 3.11: Processed AFM topographic images of semi-continuous np-Cu sputtered at different RF power of (a) 33 W, (b) 55 W, (c) 75 W, (d) 100 W and (e) 120 W.....	49
Fig. 3.12: Plot of substrate area covered by semi-continuous np-Cu as a function of RF power used for the sputtering.....	49
Fig.3.13: Transmittance vs. wavelength for dispersed np-Cu deposited by RF sputtering at different chamber pressures of (a) 23, (b) 21, (c) 17, (d) 15, (e) 12 and (f) 9Pa.....	50
Fig. 3.14: Position of T_{max} vs. chamber pressure for np-Cu's deposited by RF sputtering.....	50
Fig.3.15: Transmittance vs. wavelength for semi-continuous np-Cu sputtered with different RF power.....	51

Fig.3.16: Transmittance vs. wavelength for np-Cu's sputtered under (a) 1min and (b) 3 mins at different substrate bias voltages.....	52
Fig. 3.17: Variation of the position of transmittance peak with substrate bias voltages for np-Cu's deposited with different bias voltages.....	52
Fig. 3.18: AFM topographic images of np-Cu's deposited by RF sputtering with the substrate grounded (a) and biased by (b) - 300V and (c) – 400V DC voltages	53
Fig. 3.19: AFM topographic images of (a) as-deposited, (b) air-annealed and (c) glove box annealed np-Cu's. Thermal annealing was carried out at 300°C for 1 hour in each case.....	54
Fig.3.20: AFM topography of np-Cu's annealed in the glove box for 1 hour at different temperatures. The as-grown sample has been included for reference.....	55
Fig. 3.21: AFM topographic images of np-Cu annealed at 300°C in the glove box at different time intervals.....	57
Fig. 3.22: Plot of average particle diameter and area fraction against the annealing time for np-Cu annealed at 300°C.....	57
Fig.3.23: Particles size distribution of np-Cu obtained from AFM topographic images displayed in Fig. 3.21 for the samples annealed in the glove box for (a) 60 mins and (b) 120 mins. The distribution has been fitted with a Gaussian function (solid curve).....	58
Fig.3.24: Variation of optical transmittance with wavelength for (a) as-deposited, (b) air-annealed and (c) glove box annealed np-Cu. Thermal annealing was carried out at 300°C for 1 hour in each case.....	59
Fig.3.25: Plots of transmittance against wavelength for thermally treated np-Cu under different conditions: (a) np-Cu annealed at different temperatures and (b) np-Cu annealed at different duration.....	60
Fig. 3.26: Full linewidth at half maximum and the area fraction of island of np-Cu vs. annealing time.....	60

Fig. 3.27: AFM topographic images of thermally treated np-Cu deposited with different RF powers.....	62
Fig.3.28: Particles size distribution of np-Cu's obtained from AFM topographic image of sample sputtered with 25 W RF power and thermally treated in the glove box at 400°C for 2 hrs.....	63
Fig. 3.29: Transmittance vs. wavelength of thermally treated np-Cu's deposited with different RF powers.....	63
Fig.3.30: Plots of the plasmonic resonance peak position and the FWHM of transmittance spectra against the area fraction for np-Cu's obtained from thermal treatment of samples deposited with different RF powers.....	64
Fig. 4.1: Light scattered from a particle as a source of near field. The electric field close to the particle is formed by evanescent (near field) and scattered propagating components. Far from the particle ($r \gg \lambda$) the field is radiating by spherical waves.....	68
Fig. 4.2: Schematic of the operation configurations of the Witec Alpha 300S system that was used for the SNOM study of np-Cu's: transmission mode and collection mode.....	69
Fig. 4.3: Schematic diagram of the SNOM configuration during measurements of nanoparticle topography and light scattering in the near field.....	70
Fig. 4.4: Thin film solar cell comprising semi-transparent p-n junction sandwiched between two electrodes.....	72
Fig. 4.5: Thin film plasmonic solar cell showing region of light scattering enhancement using metal nanoparticles.....	72
Fig. 4.6: Topographic (top left) and optical (top right) images obtained from SNOM operation for semi-continuous np-Cu sputtered at chamber pressure of 9 Pa. Also displayed are the $x - z$ intensity mapping (bottom left) and the intensity plot (bottom right) showing the positions of the scattered wave.....	74

Fig. 4.7: Topographic (top left) and optical (top right) images obtained from SNOM measurement on np-Cu sputtered at chamber pressure of 12 Pa. Also displayed are the $x - z$ intensity mapping (bottom left) and the intensity plot (bottom right) showing the positions of the scattered wave.....75

Fig. 4.8: Topographic (top left) and optical (top right) images obtained from SNOM measurement for semi-continuous np-Cu sputtered at chamber pressure of 17 Pa. Also displayed are the $x - z$ intensity mapping (bottom left) and the intensity plot (bottom right) showing the positions of the scattered wave.....76

Fig. 4.9: Topographic (top left) and optical (top right) images obtained from SNOM measurement for semi-continuous Cu nanoparticles sputtered at chamber pressure of 21 Pa. Also displayed are the $x - z$ intensity mapping (bottom left) and the intensity plot (bottom right) showing the positions of the scattered wave.....77

Fig. 4.10: Topographic (top left) and optical (top right) images obtained from SNOM measurement for semi-continuous Cu nanoparticles sputtered at chamber pressure of 23 Pa. Also displayed are the $x - z$ intensity mapping (bottom left) and the intensity plot (bottom right) showing the positions of the scattered wave.....78

Fig. 4.11: Variation of scattered wave peak position with the deposition chamber pressure. $Z_{1-\max}$ represents the first significant peak intensity position of the scattered wave obtained from (x, z) SNOM map. The error bar corresponds to the standard deviation of 6 different intensity plots obtained from SNOM map79

Fig. 4.12: x - y topographic images (top), x - y optical images (middle) and x - z intensity map (bottom) of np-Cu measured in the near field using SNOM technique. The images on the right were obtained from reference bare Cu sample on glass substrate while the images on the left are for the np-Cu/SiO₂ composite.....81

Fig. 4.13: Plot of the scattered wave intensity as a function of the distance from the sample surface (out of plane) for bare np-Cu and np-Cu/SiO₂ composite.....82

Fig. 4.14: Plot of optical transmittance against wavelength for bare np-Cu and np-Cu/SiO ₂ composites. The duration for sputtering of each SiO ₂ and the plasmon resonance positions are indicated on the graph.....	83
Fig. 4.15: Plot of optical transmittance against wavelength for SiO ₂ sputtered on bare glass substrate for two different sputtering times.....	83
Fig. 4.16: EDX spectra of SiO ₂ sputtered on Si (100) for two different sputtering times. The bare Si substrate has been included for comparison.....	84
Fig. 4.17: x-y topographic images (top left), x-y optical image (top right), x-z intensity map (bottom left) and scattered wave intensity as a function of the distance from the sample surface (bottom right) of np-Cu/SiO ₂ composite annealed at 500°C for 1 hr.....	86
Fig. 4.18: Plot of optical transmittance against wavelength for bare np-Cu on glass substrate and np-Cu/SiO ₂ composite fast-annealed at different temperatures for 5 mins.....	87
Fig. 4.19: Schematic illustration of (a) possible positions of light scattered from np-Cu and (b) organic solar cell architectural design aimed at maximizing the light scattered by np-Cu's.....	88
Fig. 5. 1: Transmittance spectra of graphite nanosheets obtained from vacuum filtration of different volumes of solution as indicated.....	91
Fig. 5. 2: SEM image of thermally treated np-Cu on bare glass substrate at magnification of (a) 10K and (b) 72K and that of graphite nanosheet with embedded np-Cu at magnification of (c) 10 K and (d) 50K. The scale bar in the left images represents 1µm and 200 nm.....	92
Fig.5.3: AFM images of thermally treated (a) np-Cu and (b) composite of graphite nanosheet/np-Cu on glass substrate. Sample (b) has been scanned at higher resolutions as indicated in panel (c) and (d).....	93
Fig. 5. 4: EDX spectra of (a) bare glass substrate, (b) np-Cu deposited on glass and (c) nanocomposite on glass composed of graphite nanosheets and np-Cu's. The EDX analysis was carried out after the sample has been annealed in the glove box at 300 nm for 1 hr.....	94

Fig. 5. 5: Copper nanoparticle size distribution obtained from the SEM image presented in fig. 4.1 (b). The distribution has been fit to a Gaussian function.....	95
Fig. 5. 6: Transmittance spectra of graphite nanosheets on glass, copper nanoparticles on bare glass and graphene-like flakes with embedded copper nanoparticles before and after thermal treatment in the glove box.....	96
Fig. 5.7: I-V curves of graphite nanosheets and np-Cu/graphite nanosheets composite recorded from a probe station.....	97
Fig. 5.8: Variation of the thickness of the films with the spin coating speed. The dotted line is the thickness of graphene based TCF on a bare PET substrate.....	99
Fig 5. 9: Scanning electron micrographs of (a) Graphene based TCF on bare PET and PEDOT:PSS films spun at 2500 rpm on (b) Bare PET and (c) Graphene based TCF.....	100
Fig. 5. 10: AFM micrographs of bare PET substrate (left) and Graphene based TCF on PET substrate (right).....	101
Fig. 5. 7: AFM topography images of PEDOT:PSS spin-coated on (a) bare PET at 2500 rpm, (b) TCF coated PET at 2500 rpm, (c) bare PET at 500 rpm and (d) TCF coated PET.....	102
Fig. 5.12: Average values of (a) Surface skewness (SSK) and (b) Root mean squared roughness (RMS) of graphene based TCF layer and PEDOT:PSS films spin coated on bare PET and TCF-coated PET. Measured values of SSK and RMS for bare PET are 0.04 ± 0.01 and 0.21 ± 0.05 nm, respectively. The error bars account for the standard deviation for several measurements carried out on different areas of the same sample.....	103
Fig. 5.13: Normal incidence transmission spectra of (a) bare TCF and PEDOT:PSS spun at varying spinning speeds on bare PET at (b) 2500 RPM and on TCF-coated PET substrates at (c) 2500 RPM, (d) 2000 RPM, (e) 1500 RPM, (f) 1000 RPM (g) 500 RPM. The spectral line labeled (h) is for PEDOT:PSS spun on bare PET at 500 RPM. These spectra were used to extract the optical constants of the films.....	105

Fig. 5.14: Structural diagram of our composite films showing a bottom layer formed by an effective medium composed by a TCF and PEDOT:PSS and a top layer of pure PEDOT:PSS.....105

Fig. 5.15: Refractive indices versus thickness of graphene-based TCF and PEDOT:PSS, calculated from the envelope of transmission maxima and minima.....107

Fig. 5.16: Electrical sheet resistance vs. thickness for films spun at varying spinning speeds on bare PET and TCF-coated PET substrates. The sheet resistance of a bare graphene based TCF on PET has also been included.....107

Chapter 1

1 Optical properties and application of metallic nanoparticles

Metal nanostructures are among the most studied nanomaterials due to their outstanding size dependent properties. In particular, nanoparticles of metals show an interesting optical behavior known as size dependent surface plasmon resonance (SPR) as the nanoparticle diameter becomes comparable with, or smaller than the wavelength of incident light [1,2]. Plasmon resonance is the collective oscillation of conduction electrons and occurs when the frequency of incident light matches the resonance frequency of a gas of free electrons. It is more easily observed in certain noble metals (such as Au) because of the relative oxide free surfaces of these which form a favorable environment for their observation, at a low nanoparticles dielectric constant [3]. In Cu and Au, the position of SPR corresponds to red and yellow photon frequency respectively, in the visible region. For this reason, Cu and Au are the metals of interest for a number of applications where SPR is used for enhancing the amount of reflected light just above the plasmon frequency, especially for plasmonic solar cells and optical surface plasmon sensors. In applications for which costs are important, copper nanoparticles (np-Cu's) offer unequalled advantages over gold.

However, the efficient use of np-Cu's plasmonic solar cells and other similar devices is not without some challenges – stability and reactivity have to be controlled. This is because smaller particle diameters usually result in an increase in surface energy, which favors the aggregation of smaller particles into larger ones. Methods adopting chemical deposition techniques as means of synthesizing np-Cu's are more prone to these challenges, as well as similar challenges such as contamination by residual precursor material and, especially, oxidation. When np-Cu's are contaminated in these ways, interesting optical properties such as surface plasmon absorption resonance are not observed [4]. Physical methods of deposition of np-Cu's, including sputtering can offer a solution to oxidation issues, especially when they are integrated in protected atmosphere inside a glove box. These methods will be the main subject of this study and the applications of the grown nanoparticles in plasmonics will be discussed as well.

1.1 Plasmons in metals and metallic nanostructures

Pioneered by the works of Mie [5] and Ritchie [6] for small particles and planar interfaces respectively, plasmonics developed into widely studied area of condensed matter physics. The optical properties of metallic nanostructures are determined by strong interactions between the incident light and the conduction electrons. Collective oscillations of the conduction electron gas are called plasmons. At the resonance frequency, such collective electron oscillations may result in the enhancement of electric fields in the vicinity of a nanostructured metallic surface [7]. Therefore, surface plasmons have opened an avenue towards the possibility to amplify, concentrate and manipulate light at nanoscale [8].

Plasmonic field enhancements may be highly localized if they are generated in the proximity of small metallic particles of the appropriate shape and size and are mainly near-field in nature [9]. The enhancement that is achieved when nanostructured particles scatter light into the photoactive region of a nearby optoelectronic device may result in a strong absorption of light and the subsequently enhanced generation of electron-hole pairs in such a plasmonically enhanced device. A variety of plasmonic devices, including solar cells, light emitting diode, detectors and lasers have been proposed and constructed [10-12]. Careful optimization is, however, required during the design and fabrication processes to ensure that the scattered light is optically conveyed into the active region. Such optimization forms the basis of plasmonics as we report it in the following sections of this chapter.

Plasmons can exist in the bulk of metals, on thin metallic surfaces or they can be localized inside, or on the surface of metallic nanoparticles. Depending on the specific situation, we may have bulk plasmons (BP), surface plasmons (SP) or localized plasmons (LP). This classification is due to the different boundary conditions associated with different structures [13].

1.1.1 Bulk plasmons

Bulk plasmons refer to collective modes of oscillation of the free electron gas inside a sufficiently large volume of bulk metal. The excitation of bulk plasmons leads to the collective motion of a very large number of free electrons, resulting in small density fluctuations around the average density n , of the unperturbed electron gas. According to the Drude-Sommerfeld free

electron model [14], the quantum behavior of an electron gas is determined by its frequency-dependent complex dielectric function that can be expressed as [15]:

$$\varepsilon_m(\omega) = 1 - \frac{\omega_p^2}{(\omega^2 + i\gamma\omega)} \quad (1.1)$$

Where $\gamma \ll \omega_p$ is the screening factor and the plasmon frequency is defined as

$$\omega_p^2 = \frac{n.e^2}{m.\varepsilon_o} \quad (1.2)$$

Here m and e are the mass and charge of the electron, ε_o is the permittivity of vacuum and ω is the frequency of the incident light. The presence of an imaginary part in ε_m is a consequence of the fact that metals can absorb light. Coherent oscillations of the free electrons are highly screened as long as $Re(\varepsilon_m(\omega)) > 0$ and the frequency of their motion is below ω_p . However, at $\omega \geq \omega_p$, we have $Re(\varepsilon_m) < 0$, the long-range (Coulombic) forces become effective and undamped waves travel through the free electron gas[16]. This has very important consequences for our work. First, it can be observed that the bulk plasmon frequency of a metal depends via eq. (1.2), only on a number of universal constants and on the density of free electrons in a given metal. For instance, silver has a plasmon frequency of approximately $\hbar\omega_p = 3.7$ eV, in the near ultraviolet, and therefore reflects and scatters all of the visible photons. This limits to ultraviolet light the transmittance of a plasmonic layer made out of silver. The active region of a plasmonic device would be poorly illuminated, with detrimental effects on the device efficiency. Instead, copper and gold have a plasmon frequency in the visible photon energy range. For instance, $\hbar\omega_p = 2.3$ eV, in the green – blue range for copper, which results in high transmittance for green, blue and ultra violet photons (that can be, therefore, absorbed in the active layer of an optical device) and high reflectance for red photons, with a possibility of plasmonic enhancement in the red region of the spectrum of visible light, where semiconducting materials exhibit poor absorption of light, which need to be enhanced. In summary, as shown in Fig. 1.1, copper and gold enhance the amount of light in the red and infrared where it is needed because solar cell active materials are poorly absorbing. Instead, copper and gold do not affect the quantity of light that is absorbed in the visible where, solar cells materials are highly absorbing and, there is a sufficient quantity of light because here is the maximum of the solar spectrum.

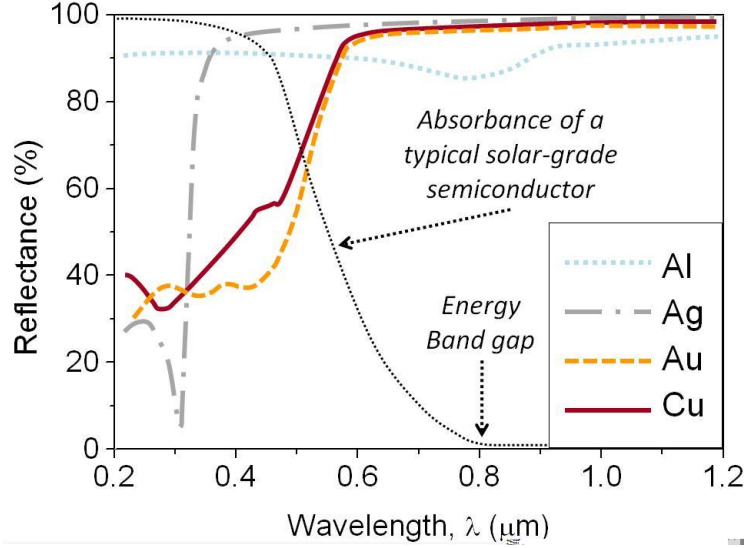


Fig. 1.1: Reflectance of selected metals as a function of wavelength. As a consequence of eq. (1.1) the reflectance is nearly 100% above the metal plasmon frequency, while rapidly decreasing below. Also indicated is a typical trend for the optical absorbance of a typical solar-grade semiconductor (for which the optimal energy band gap for best AM 1.5 solar efficiency is approx. 1.5 eV, corresponding to 0.83 μm) Metals suitable for applications in semiconducting plasmonic devices have a plasmon energy $\hbar\omega_p$ just above the semiconductor band gap energy. Therefore, Au and Cu are optimized for applications in plasmonic solar cells, while Ag and Al (with too high plasmon energies, in the UV range) are not.

1.1.2 Surface plasmons

Surface plasmons are associated with coherent electron oscillations which occur at the interface of a sufficiently thin metallic film and a dielectric medium. Plasmons are in this case confined in the proximity of the metallic surface so that plasmonic waves propagate along the interface of the two media. The spatial and temporal dependence for the electric field of this surface wave can be expressed in terms of plane waves, as

$$\vec{E}(\vec{r}, \omega) = \vec{E}_o \exp(i[\vec{k} \cdot \vec{r} - \omega t]) \quad (1.3)$$

Where $|\bar{E}|$ is the intensity of the electric field and \bar{k} is the wave vector. The planar geometry of the boundary conditions allows to write eq. (1.3) in a way that separates the spatial components of the wave in directions parallel and orthogonal to the surface with wave vectors $\bar{k}_m = (k_x, k_{zm})$ and $\bar{k}_d = (k_x, k_{zd})$ inside the metal and the dielectric medium, respectively. The expressions for the spatial profile of the propagating waves inside the two media (based on the geometry depicted in Fig. 1.2) are then given by:

$$\bar{E}(\bar{r}, \omega) = \bar{E}_0 \cdot \exp(-k_{zd} \cdot z) \cdot \exp[i(k_x \cdot x - \omega t)] \quad (1.4)$$

For this geometry, the Helmholtz equation [13, 17], describing the wave propagation at the interface of the metal and the dielectric medium can be written as:

$$\nabla^2 \bar{E} + k_x^2 \cdot \epsilon_m(\omega) \cdot E = 0 \quad (1.5)$$

Eq. (1.5) can be solved exactly by imposing the appropriate conditions for continuity of the electric field at the interface [18, 19]:

$$\frac{k_{zm}}{\epsilon_m(\omega)} = \frac{k_{zd}}{\epsilon_d}, \quad (1.6)$$

where

$$k_x^2 + k_{zm}^2 = \epsilon_m(\omega) \cdot \left(\frac{\omega}{c}\right)^2, \quad (1.7)$$

and:

$$k_x^2 + k_{zd}^2 = \epsilon_d \cdot \left(\frac{\omega}{c}\right)^2, \quad (1.8)$$

where c is the speed of light in vacuum. In most cases of practical interest for our study, the dielectric material is an optically non-absorbing medium. Therefore, its dielectric constant, ϵ_d , that appears in eqs. (1.6) and (1.8) is real and weakly dependent on ω .

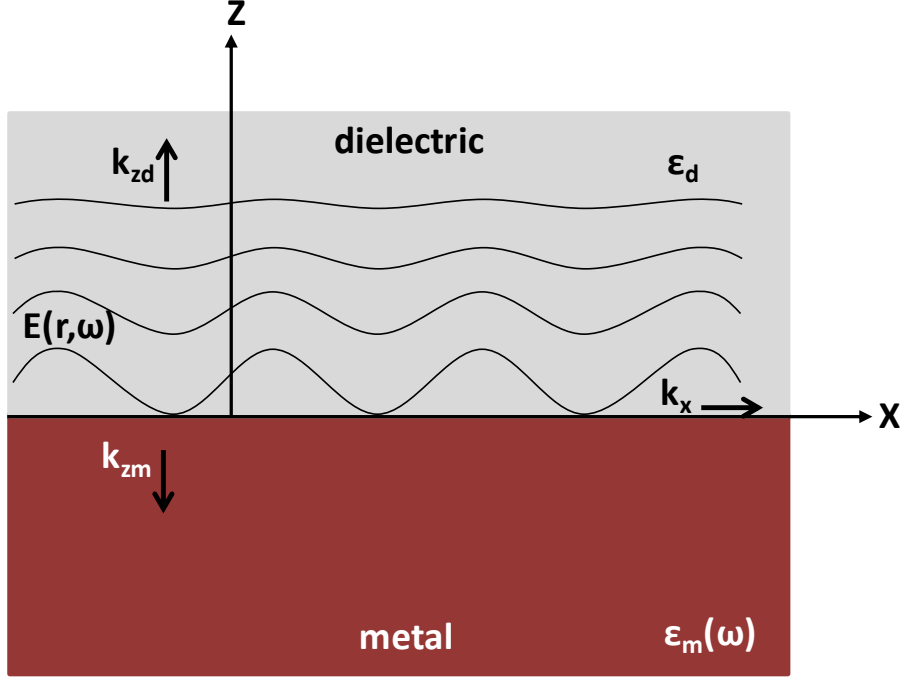


Fig.1.2: Propagation of electromagnetic wave at an interface between metal and dielectric media with relative dielectric constants $\epsilon_m(\omega)$ and ϵ_d respectively.

The dispersion relations that the surface waves must follow due to the presence of the interface and the dependence of ϵ_m on ω are given by:

$$k_x^2 = \frac{\omega^2}{c^2} \cdot \frac{\epsilon_m(\omega) \epsilon_d}{\epsilon_m(\omega) + \epsilon_d} \quad (1.9)$$

$$k_{zm}^2 = \frac{\omega^2}{c^2} \cdot \frac{\epsilon_m^2(\omega)}{\epsilon_m(\omega) + \epsilon_d} \quad (1.10)$$

The above result shows that the excitations of surface plasmons are associated with transverse and longitudinal electric fields that have their maxima at the surface (i.e. $z = 0$). The nature of eq. (1.4) demonstrates that the field decays exponentially with the distance from the interface as $\exp(-k_{zm}|z|)$ [18]. The exponential dependence of the electric field intensity on the distance along z -direction is demonstrated in Fig. 1.3(a) while the subsequent oscillations and the associated surface wave are shown in Fig. 1.3 (b).

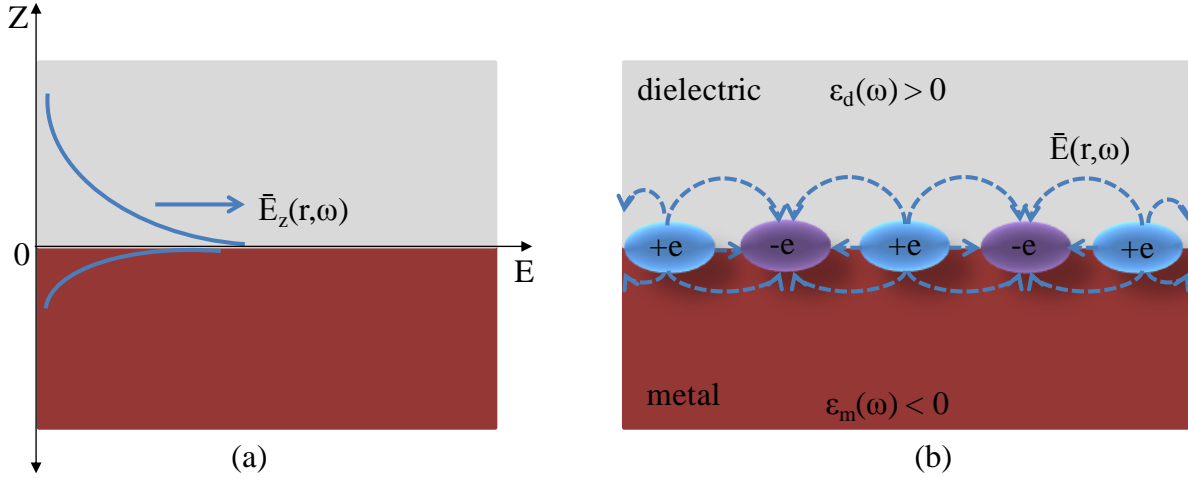


Fig. 1.3: Schematic of (a) exponential dependence of the field intensity on the distance away from the interface, (b) surface EM wave propagating at a metallic and dielectric interface with different dielectric constants.

Fig. 1.3(a) shows that SP is an interface phenomenon that is highly sensitive to the dielectric function of the adjacent dielectric medium. Resonant enhancement of the electric field occurs when $k_x \rightarrow \infty$ and/or $k_{zm} \rightarrow \infty$. According to eqs. (1.9) and (1.10) this happens when the denominator in such equations tends to zero and, therefore, when

$$\text{Re}[\epsilon_m(\omega)] + \epsilon_d = 0 \quad (1.11)$$

Since the dielectric function of the metal is given by eq. (1.1), we can replace it in eq. (1.11) obtaining that collective oscillations of the electric dipoles of the surface occurs at a frequency $\omega = \omega_{sp}$, satisfying the condition

$$1 - \frac{\omega_p^2}{\omega^2} + \epsilon_d = 0, \quad (1.12)$$

and, inverting eq. (1.12), we obtain that surface plasmon resonance occurs at

$$\omega_{sp} = \frac{\omega_p}{\sqrt{1 + \epsilon_d}} \quad (1.13)$$

Since $\epsilon_d \geq 1$ for dielectric media, eq. (1.13) indicates that SPR always occurs at smaller frequencies (and, therefore, larger wavelengths) than bulk plasmon resonance. Eq. (1.13) also

suggests that SPR cannot be observed in the visible photon energy range when metallic surfaces are oxidized, since metal oxides (e.g. CuO_x in the case of copper thin films and np-Cu's) generally possess high dielectric constants, $\epsilon_d \gg 1$. This result is critical for our study because it suggests that the surface of our np-Cu's must be sufficiently clean from oxidation and dielectric impurities in order for the particles to generate a sufficient surface plasmonic enhancement. Therefore, eq. (1.13) recommends the use of vacuum-based physical techniques for the preparation of our nanoparticles and on oxygen-free, controlled, environment for their manipulation and, specifically, a nitrogen-purged glove box.

Instead, for the special case of clean metallic surfaces interfaced with vacuum (for which $\epsilon_d = 1$) eq. (1.1) becomes:

$$\omega_{sp} = \frac{\omega_p}{\sqrt{2}} \quad (1.14)$$

For the metals, the SPR frequency given by eq. (1.14) lies in the ultraviolet photon energy region because of the strong density of free electrons, which produces, via eq. (1.2), values of $\hbar\omega_p$ above 4 eV. However, copper and gold are remarkable exceptions to this rule, as their bulk plasmon resonance lie close to the visible region (see Fig. 1.1) which implies values of $\hbar\omega_{sp}$ in the red – yellow photon energy range and the possibility to use SPR from these metals to reflect light at long wavelengths without absorbing it in the central portion of the visible range.

The surface plasmon resonant frequency given by (1.13) lies in the UV spectral region because of the strong negative dielectric function of metals in this region. As such momentum of surface plasmon k_{sp} is longer than that of plane waves. This can be seen from the dispersion relation shown in Fig. 1.4.

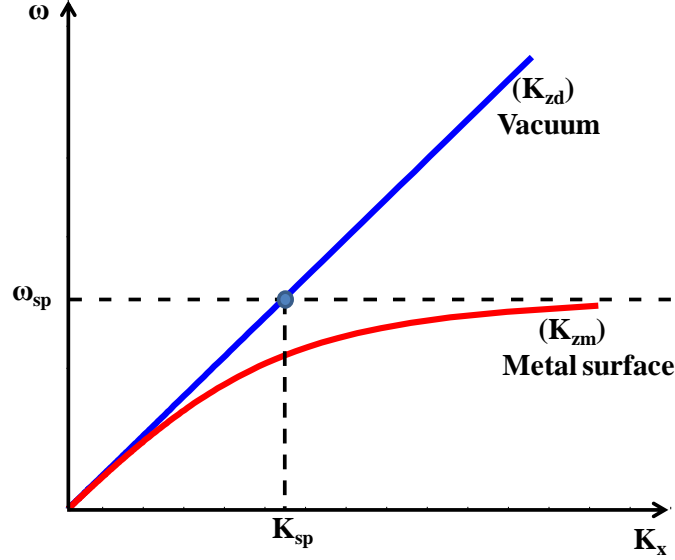


Fig. 1.4: Plot of the dispersion relation for light propagating in vacuum and for plasmonic waves propagating along a metallic surface.

Figure 1.4 compares the dispersion relations $\omega(k_x)$ for plane electromagnetic waves in vacuum, $\omega = c.k_x$, and inside a free electron gas, for which eq. (1.9) can be written. For long wavelengths and low frequencies, the wave number of surface plasmons, is close to the wave number of photon in vacuum and the electric field extends over many wavelengths above the surface of the metals [13]. In the opposite regime of short wavelengths, the frequency of electromagnetic waves in the metal tends to the surface plasmon frequency eq. (1.14), k_x goes to infinity and subsequently, the group velocity tends to zero [13]. The plasmonic mode thus acquires a stationary, evanescent and non-propagating character. This is a remarkable example of evanescent wave, with an associated near-field that is localized in the proximity of a metallic layer of subwavelength thickness. Since the degree of localization only depends on the specific geometry and optical properties of the used materials, near fields can be used to investigate small objects with subwavelength resolution, as we will discuss in some details in the next chapters of this study.

Figure 1.4 also shows that, due to the conservation of momentum, the condition $k_{sp} \approx k_x$ must hold. Thus, a SP cannot be excited by using any possible plane wave and wave number for incident light. The wave vector necessary for SP excitation corresponds to the point on the dispersion curve indicated in Fig. 1.4. Experimentally, this is realized by using special matching techniques, such as prism coupling. These techniques are explained in details in the literature

[20, 21]. However, this condition is relaxed for non-planar surfaces, for instance surface plasmons localized in nanoparticles.

1.1.3 Localized surface plasmons

Unlike the case of a SP, in which an electromagnetic wave coupled to a free electron gas results in a propagating field along a metallic surface, localized plasmons (LP) involve a non-propagating collective excitation of electrons confined in small metallic structures. A sub-wavelength metallic particle can be treated as a spherical region in which electrons are allowed to move freely as shown in Fig. 1.5. Drift of conduction electrons upon excitation by an external electric field results in the formation of polarization charges of opposite sign on the two hemispheres forming the surface of the particle.

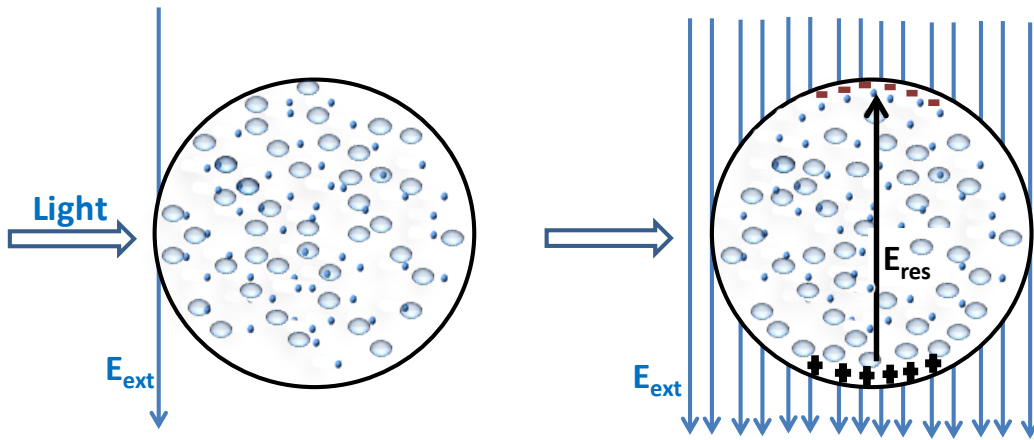


Fig.1.5: Schematic depiction of influence of external light field on randomly oriented charges in a metallic nanoparticle. The incident electromagnetic wave excites charge separation to create an electric dipole

In this model the total polarization P , of the two hemispheres is given by the Clausius-Mossotti relationship [14]:

$$P = \frac{\varepsilon_m(\omega) - \varepsilon_d}{\varepsilon_m(\omega) + 2\varepsilon_d} \quad (1.15)$$

According to eq. (1.15) the polarization depends on the dielectric constant of the surrounding medium and that of the metallic sphere. Thus, it experiences a resonant enhancement under the Frohlich condition [22], when the denominator in eq (1.15) tends to zero:

$$\text{Re}[\varepsilon_m(\omega)] + 2.\varepsilon_d = 0 \quad (1.16)$$

Eq. (1.16) is qualitatively similar to eq. (1.11) that was derived for a planar metallic surface. An expression for the frequency of the surface plasmon resonance localized on a spherical particle can be determined by replacing eq. (1.1) into eq. (1.16):

$$\omega_{LP} = \frac{\omega_p}{\sqrt{1 + 2.\varepsilon_d}} \quad (1.17)$$

Comparing eq. (1.17) to eq. (1.13) we can observe that plasmons confined at the surface of a spherical metal nanoparticle are downshifted at lower frequencies than their two-dimensional counterparts that are delocalized on a flat surface of the same metal. For a generic surface, and for non-spherical particles, it can be demonstrated [14, 23] that the plasmon resonance frequency always assumes intermediate values between those given by eqs. (1.13) and (1.17). Specifically, for nanostructures of ellipsoidal shape, it can be obtained that

$$\omega_{LP}(x) = \frac{\omega_p}{\sqrt{1 + x.\varepsilon_d}} \quad (1.18)$$

where x is a depolarization coefficient that takes into account the shape of the specific nanostructure. Therefore, synthesizing metallic nanoparticles with carefully designed geometry is critical for their optimization for a given application requiring a well defined plasmon frequency. In addition, strong light scattering is associated with excitation of metal nanoparticles at their plasmon frequency. In the limit where the nanoparticle diameter, is small enough compared with the wavelength of incident light, the scattering cross-section for spherical particle is given by [24]:

$$Q_{sca} \approx \frac{24.\pi^3.V^2.\varepsilon_d^2}{c^4} \cdot \left| \frac{\varepsilon_m - \varepsilon_d}{\varepsilon_m + 2.\varepsilon_d} \right|^2 .\omega^4 \quad (1.19)$$

where V is the volume of the spherical particle. Eq. (1.19) indicates that also Q_{sca} is strongly enhanced for $Re[\varepsilon_m(\omega)] + 2\varepsilon_d = 0$, at the LP frequency given by eq. (1.17), because also the denominator of (1.19) goes to zero.

If the spherical nanoparticles are not much smaller than a wavelength the dipole surface plasmon approximation is not satisfied. In this case, the scattered electric field is not purely dipolar in nature, but is formed by an infinite superposition of multipoles [23]. The multipolar nature of the scattered field manifests itself with the fact that the field intensity undergoes a number of oscillations, with maxima and minima at specific distances r from the surface of the particles, while the dipolar field (see eg. Fig. 1.3a) follows a much simpler trend and exponentially decays away from the metal surface. The expression of the scattering cross section for a spherical particle in the more general case in which the multipolar nature of the electric field must be considered has been calculated by Bohren and Huffman [23] and is given by

$$Q_{sca} = \frac{24\pi^3 V^2 \varepsilon_d^2}{c^4} \sum_{n=0}^{\infty} (2n+1) (|a_n|^2 + |b_n|^2) \omega^4 \quad (1.20)$$

Where a_n and b_n express the contribution to the scattering process of the n -th multipole. These coefficients can be written in terms of first-type and second-type Bessel-Riccati functions, $\psi_n(p)$ and $\xi_n(p)$ and their first derivatives:

$$a_n = \frac{m\psi_n(mx)\Psi'_n(x) - \psi_n(x)\psi'(mx)}{m\psi_n(mx)\xi'_n(x) - \xi_n(x)\psi'_n(mx)} \quad (1.21a)$$

$$b_n = \frac{\psi_n(mx)\Psi'_n(x) - m\psi_n(x)\psi'(mx)}{\psi_n(mx)\xi'_n(x) - m\xi_n(x)\psi'_n(mx)} \quad (1.21b)$$

Where $x = 2\pi\sqrt{\varepsilon_d}r/\lambda$ expresses the distance r from the centre of the particle, normalized with the wavelength of light, λ and the dielectric constant of the background medium, while $m = \sqrt{\varepsilon_m/\varepsilon_d}$. Eq. (1.20) vanishes more rapidly, at smaller values of r , while low $-n$ terms are more slowly decaying in space. Important consequences of eq. (1.20) for our work are the spatial oscillations of Q_{sca} and of the intensity of the scattered electric field. These will be qualitatively discussed in chapter 4 of this study, in which these spatial oscillations will be experimentally measured.

1.2 Conclusions and Thesis overview

In conclusion, from our previous considerations, copper and gold nanoparticles are found to be extremely promising for scattering light from the sun into the active layer of semiconductor devices and, especially, into solar cells that convert sunlight into electrical power. The SPR and localized plasmon resonances of gold and copper has been found to be just below the maximum peak of the AM1.5 solar spectrum, which is located in the green ($\lambda_m = 550$ nm, $\hbar\omega_m = 2.25$ eV). This makes np-Au and np-Cu very well suited to concentrate light at $\lambda > \lambda_m$ (and $\omega < \omega_m$) where solar grade semiconductors exhibit a poor absorption coefficient, while not preventing the semiconductor to absorb light at $\lambda \leq \lambda_m$ (and $\omega \geq \omega_m$) the spectral range for which solar-grade semiconductors are generally optimized.

To this end np-Cu's are preferable over np-Au's because of their cost – effectiveness, but copper is more prone to oxidation and contamination. Therefore we have concluded that care will have to be exercised in the preparation and manipulation of np-Cu's for plasmonic solar cell applications, because SP and LP cannot be observed if these nanoparticles are oxidized, or contaminated. We have also concluded that specific experimental analysis will be required to understand the complicated multipolar behavior of the electric field plasmonically scattered by np-Cu of size comparable to the wavelength of incident light.

Therefore, our study will be divided as follows: in chapter 2 we discuss a physical process, that will be used to deposit np-Cu's in vacuum, preventing their oxidation, and we describe the radio-frequency sputtering operations we designed and built for growing np-Cu. Two relevant characteristics of such apparatus are in the possibility to apply a direct current (dc) bias voltage to the substrate (in order to limit the growth rate and obtain np-Cu's at the opposite of Cu films) and the integration of the sputtering chamber with a glove box for ensuring oxygen-free manipulation of the nanoparticles. In chapter 3 we describe the characterization of sputtered np-Cu's with a suite of techniques, including atomic force microscopy, scanning electron microscopy, compositional analysis and UV – visible spectrophotometry, with the objective to correlate the sputter growth parameters used in chapter 2 to the nature, size, shape and density of the particles. In chapter 4, more detailed characterization of the particles is carried out by scanning near field optical microscopy (SNOM) in order to understand the multipolar behavior of the electric field associated to light scattered at frequencies close to the plasmon of the

particles. This is essential to identify what type of the np-Cu's we synthesized are better suited to be incorporated in plasmonic solar cells and to determine the best possible architecture for these devices.

In chapter 5, we demonstrate the importance of the integration of the sputtering system with the glove box for the incorporation of np-Cu on a number of solar grade substrates (including graphene layers) and the additional processing of such substrates by spin coating additional organic layers on them in controlled atmosphere. This work is preliminary to the preparation of organic solar cells incorporating np-Cu inside the glove box. Finally, in chapter 6, we summarize our study and suggest future research directions for our work

1.3 References

- [1] S. Zavyalov, A. Timofeev, A. Pivkina and J. Schoonman, *Nanostructured Materials: Selected Synthesis Methods, Properties and Applications* edited by P Knauth and J Schoonman. Kluwer Academic Publishers, NY (2004)
- [2] A.A. Lushnikov and A.J. Simonov, *Physik A Hadrons and Nuclei*, **270(1)**, 17 (1974)
DOI:10.1007/BF01676788
- [3] Y. Chu, E. Schonbrun, T. Yang and K. B. Crozier, *Appl. Phys. Lett.* **93**, 181108 (2008);
doi:10.1063/1.3012365
- [4] J.J. Brege, C.E. Hamilton, C.A. Crouse and A.R. Barron, *Nano Lett.* **9(6)**, 2239 (2009)
- [5] G. Mie, *Ann. Phys.* **25**, 377 (1908)
- [6] R.H. Ritchie, *Phy. Rev.* **106**, 874 (1957)
- [7] K.R. Catchpole, *Phil. Trans. Royal Soc.A* **36A**, 3493 (2006)
- [8] W.L. Barnes, A. Dereux and T.W. Ebbesen, *Nature* **424**, 824 (2003)
- [9] D. Courjon and C. Bainier, *Rep. Prog. Phys.* **57**, 989 (1994)
- [10] K.R. Catchpole and A. Polman, *Opt. Express* **16**, 21793 (2008)

- [11] X. Gu, T. Qiu, W. Zhang and P.K. Chu, *Nanoscale Res. Lett.* **6**, 199 (2011)
- [12] E.E. Bedford, J. Spadavecchia, C. M. Pradier and F. X. Gu, *Macromol. Biosci.* **12**, 724 (2012)
- [13] S.A Maier, *Plasmonics: Fundamentals and Applications*, Springer (2007)
- [14] N. W. Ashcroft, N.D. Mermin, *Solid State Physics* (College edition), Harcourt College Publisher, (ISBN 0-03-08993-9) (1976)
- [15] Kittel, Charles, *Introduction to Solid State Physics* (8th ed.). Hoboken, NJ: John Wiley & Sons, (ISBN 0-471-41526-X) (1996).
- [16] Raether, Heinz, *Tracts in Modern Physics*, **88**, 4 (1980) Springer
- [17] D. Colton and R. Kress, *Integral Equation Methods in Scattering Theory*, John Wiley & Sons (1983)
- [18] H. Raether, *Surface Plasmons on Smooth and Rough Surfaces and on Gratings*. Springer Tracts in Modern Physics 111. New York: Springer-Verlag ISBN 0-387-17363-3, (1988).
- [19] G. M. Cottam, *Introduction to Surface and Superlattice Excitations*. New York: Cambridge University Press. ISBN[[Special bookSources/100521321549/100521321549]] (1989)
- [20] Y. Y. Teng and E. A. Stern, *Phys. Rev. Lett.* , **19** (9), 511 (1967).
- [21] A. Otto, *Zeitschrift f`ur Physik.* **216**, 398 (1968)
- [22] A. Sihvola, *Progress in Electromagnetic Resesearch*, PIER **62**, 317 (2006)
- [23] C. F. Bohren, D. R. Huffman, *Absorption and Scattering of Light by Small Particles*, Wiley, New York (1983)
- [24] O. Muskens, D. Christofilos, N. D. Fatti and F. Vallee, *J. Opt. A: Pure Appl. Opt.* **8**, S264 (2006)

Chapter 2

2 Sputtering operation for nanoparticles deposition

2.1 Introduction

Copper nanoparticles (np-Cu's) are generally fabricated by chemical routes, such as wet chemical synthesis, or by means of physical deposition processes including thermal evaporation, sputtering and lithographic techniques. The synthesis of np-Cu's by chemical methods is realized by the use of reducing and capping agents, an approach that reduces the effect of particle-particle interaction and the resultant agglomeration in colloidal suspension [1-3]. However, the end product is prone to contamination by the precursor residual material, their by-products or copper oxide [4]. When this happens, several relevant properties of np-Cu's, including the presence of a plasmonic resonance, are not observed [5].

In view of the above, this chapter describes the physical deposition techniques developed in the frame work of this, including the assembling of a sputtering set-up attached to a glove box protected from oxygen contamination, the procedure followed to carry out the deposition of np-Cu's and their preservation from both contamination and oxidation. The experimental apparatus has been specifically designed by us for optimizing the deposition of np-Cu's, followed by their application for the fabrication of mixed np-Cu/organic polymer nanocomposites and their incorporation into plasmonic solar cells.

2.2 Sputtering deposition technique

Sputtering is a very common technique for the preparation of thin films in vacuum [6]. In sputtering, the atomic precursors that will form the desired thin film are ejected from a target material by bombarding it by energetic ions. This technique can be used to deposit a variety of thin films and nanoparticles. Historically, the first recorded observation of sputtering was made by W.R. Grove in 1852 [7]. However, its development into a modern deposition technique for thin films and nanoparticles is due to Langmuir in 1920. Since then, sputtering has emerged as an efficient method, enabling to dispense metals and semiconductors in various forms, including Al and Al- based thin films, Ti, Tin, Si, SiN, nickel, cobalt, gold, etc [6].

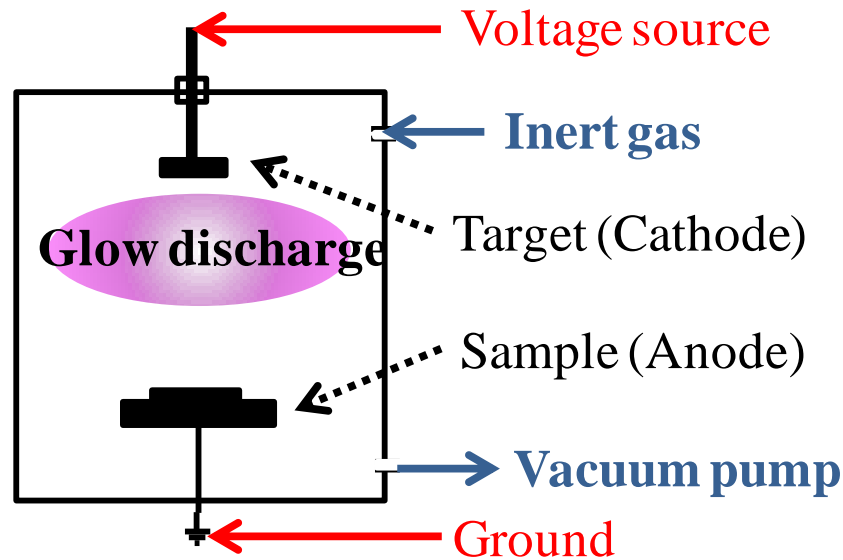


Fig.2.1: Schematic illustration of the fundamental principles of sputtering

Deposition by sputtering can be accomplished by radio frequency (RF) and direct current (DC) sputtering methods. The fundamentals of this technique can be described in terms of a glow discharge between two plates forming a capacitor. As shown in Fig. 2.1, the target made out of the precursor material and the substrate for growing the thin film (or the nanoparticles) are facing each other and are attached to the electrodes. An inert gas, usually argon, is introduced between the two electrodes to serve as a medium for initiating and maintaining the glow discharge. When a sufficiently high DC voltage is applied between the electrodes, electrons are accelerated from the target, that acts as the cathode, onto the anode that bears the substrate. Electrons make collisions with the argon atoms, which cause them to ionize or reach a metastable state. The resulting positive ions (Ar^+), are subsequently accelerated to the target where they dislodge neutral atoms through momentum transfer. These atoms from the target also become part of the discharge and deposit on the substrate, where they form a thin film or a system of nanoparticles, depending on the specific surface energy and temperature of the material being formed.

2.2.1 RF Sputter Deposition from conducting target

The standard radio frequency allowed by international communication authorities for industrial sputtering processes is 13.56 MHz, with the objective to prevent interference with radars, radio – communication and broadcasting systems. In an RF sputtering system, like the one assembled for

our thesis work, an AC power supply is coupled (at the above frequency) to the smallest in size of the two electrodes of the sputtering chamber, where gas ionization and the subsequent generation of the glow discharge takes place. Plasma generation is a critical step in setting up a successful sputtering process. In order to achieve a successful RF sputtering operation, the impedance of the plasma must be equal to the impedance of the power supply so that the entire power produced by the generator is transmitted to the glow discharge and is not dissipated in the environment or reflected back to the generating antenna. As shown in Fig. 2.2, a capacitance-based matching network is required for such operation, so that the impedance of the network minimize the losses in the form of power reflected of the RF generator. Such conditions ensure an efficient RF power transfer from the generator to the process chamber and the adequate generation of plasma needed for the sputtering operation to proceed stably.

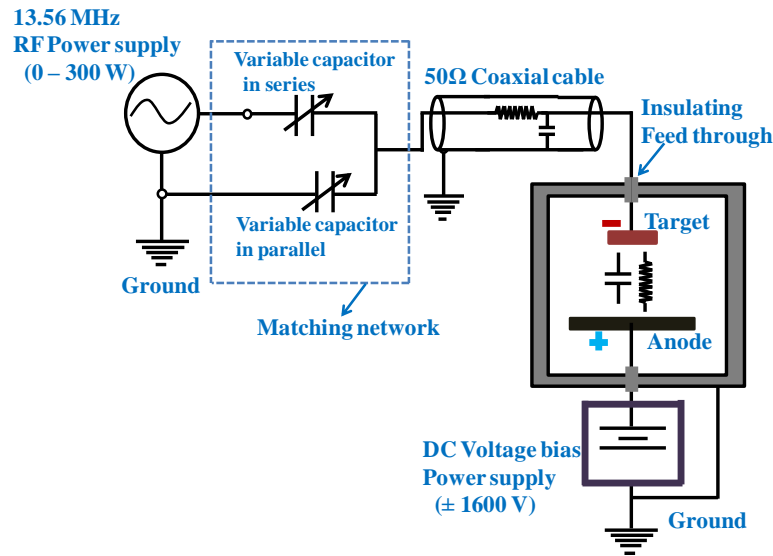


Fig.2.2: Schematic of RF sputtering assembly, used in our project, including RF power generator, capacitive matching network, coaxial cable for RF power transfer, sputter vacuum chamber and DC voltage power supply (used in some of the depositions)

The plasma contains three important species, electrons, ions and neutral atoms. Since electrons have a relatively light weight, their velocity is significantly higher than that of the ions at a similar kinetic energy. Therefore the motion of the electrons occurs at time scale that is faster than the time scales at which ions and the neutral move and the motion of the ions in an RF glow discharge is determined by the mean electric field from the electrons. Highly mobile electrons

create a negatively charged region next to the sputtering target consisting of a glowing sheath. The sheath voltage depends upon the RF peak voltage V_o , the area A_1 of the target and that of the substrate stage (A_2) according to the relationship [8, 9,]:

$$V_{sh} = V_o \left(1 - \frac{A_1}{A_2} \right)^2 \quad (2.1)$$

Equ. (2.1) indicates that a large value of A_2 is essential in order to raise the target sheath voltage and increase the rate of bombardment of the target by positively charged argon ions, leading to momentum transfer dislodging the target atoms. The effectiveness of momentum transfer for the case of an elastic collision onto the target is described by a transfer function, given in terms of the mass, M_1 of the impinging argon ions and the mass M_2 of the stationary target atoms [6, 10-12]:

$$\frac{E_{th}}{E_s} = \frac{(M_1 + M_2)^4}{4.M_1.M_2.(M_1 - M_2)^2} \quad (2.2)$$

Therefore, sputtering of target atoms begins at a threshold energy E_{th} of the argon ions that depends on the efficiency of momentum transfer to the target surface as well as the binding energy, E_s , of the atoms in the target. A consequence of this process is that the ions transfer all or part of their energy by collisions when they are accelerated onto the target, resulting in what is known as a collision cascade [6]. Figure 2.3 shows the evolution of a collision cascade in a typical ion-target interaction.

The onset of the collision cascade begins with the distribution of the initial energy and momentum of impinging energetic ions among the target atoms. In turn, recoiled target atoms collide with atoms at rest, to expand the collision cascade. When the kinetic energy of the impinging ions is larger than ~ 1 KeV, the cascade results in a series of binary collisions in a stationary matrix [12]. An atom is dislodged from the target if it has a sufficient kinetic energy to overcome the electrostatic force in moving away from the target surface during the collision events. At that point the atom from the target enters the plasma and the multiple collisions (with electrons, Ar ions, neutrals or other precursor ions) will result in a random walk ending with the atom depositing onto the substrate.

Besides sputtering of atoms from the target surface, the ion – surface interaction may lead to other processes, such as ion implantation of colliding particles, enhanced chemical reaction on the target surface, as well as the reflection of the ions back into the plasma. Similarly, inelastic effects may lead to emission of uv/vis or x-rays and secondary electrons. Many of these effects and interaction have been described and observed by many authors [6, 12-17].

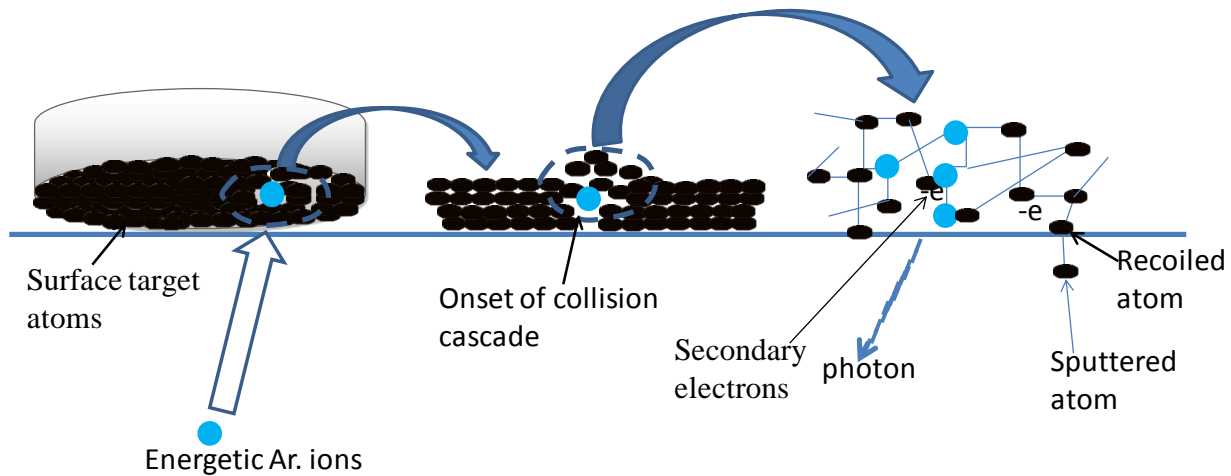


Fig. 2.3: Collision event arising from ions-target atoms interaction. Onset of cascade starts with the near surface atoms.

2.2.2 RF Sputter Deposition from insulating target

A significant advantage of RF sputtering over DC sputtering is that it is suitable for growing materials from both metal and insulating targets. When an insulator is used as the sputtering target, the ions in the plasma bombarding the target will create charging effect on the surface of the insulating target. Positive charges would then accumulate on the target, resulting to a strong electric field in the vicinity of the target. The field strength can be very high and makes it impossible to sustain the plasma by an externally applied DC voltage because the required voltage would be impracticable to generate.

To demonstrate this important advantage of RF sputtering, our system was also utilized for sputtering silicon oxide thin films as will be discussed in details in chapter 4. This was accomplished by attaching a 2-inch diameter silicon oxide (glass) target to our cathode electrode in place of the metallic target. The deposition rate is very important in determining the thickness of a thin film. We determined the deposition rate of SiO₂ thin films grown on a Si substrate by

partially masking the substrate during a set of sputtering depositions at constant growth parameters. Figure 2.4 shows a plot of the thickness of SiO₂ on a Si substrate against the sputtering time. The slope of this graph gives the sputtering rate as 54Å/min for RF power of 90W.

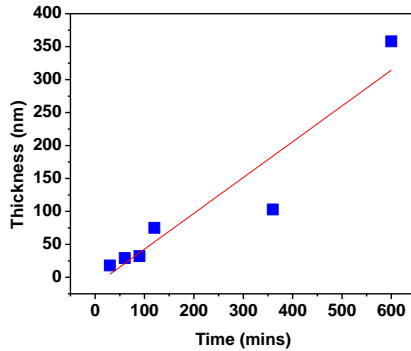


Fig. 2.4: Variation of film thickness against the deposition time to determine the sputtering rate of our RF deposition system from an insulating target

2.2.3 Nucleation of metallic nanoparticles by sputtering

The fabrication of nanoparticles and thin films of technological importance begins with the nucleation of precursor species on a substrate (heterogeneous nucleation) or in the vapor phase (homogeneous nucleation). In heterogeneous nucleation, three different growth modes are involved. The three modes, which are illustrated schematically in Fig. 2.5 includes layer by layer growth or Frank-van der Merwe [18], island growth or Volmer-Weber (V-W) [19] and Stranski-Krastanov, which is an intermediate combination of layer by layer and island growth [6]. As shown in Fig.2.5a, Frank-van der Merwe growth type involves a 2-dimensional growth of the nucleating particles, on a substrate, to form homogeneous and uniform film. It is an ideal growth mechanism when planar sheets are required and typically results from the fact that atoms are more strongly bound to the substrate than to each other. Example of this growth mode is the single crystal epitaxial growth of semiconductor films [6, 20].

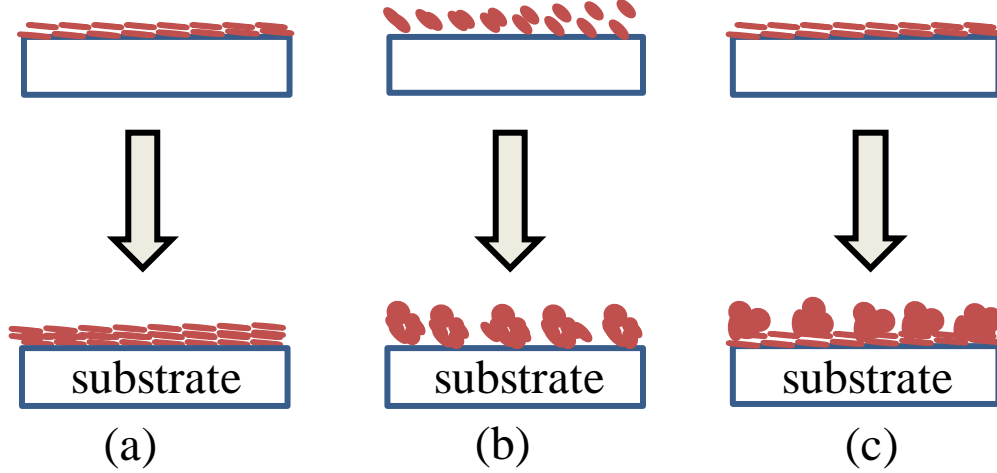


Fig. 2.5: Schematic diagram of three heterogeneous growth modes described as (a) Frankvan der Merwe (b) Volmer-Weber and (c) Stranski-Krastanov

In the case of Volmer-Weber growth mode, the impinging atoms nucleate and form islands on a substrate surface. The island formation is favored because the atoms in the deposit are more strongly bound to each other than to the substrate, as determined by the interfacial free energy and the lattice match between the substrate and the nucleating species. The Young-Dupre equation is used to describe the relationship between the surface energies in a heterogeneous mode of film formation processes [21-23]:

$$\gamma_{sv} = \gamma_{cs} + \gamma_{cv} \cdot \cos(\alpha) \quad (2.3)$$

In lattice-matched systems, island growth is favored over planer thin films due to high substrate-film interfacial energy, γ_{cs} and high film-vacuum surface energy, γ_{cv} . The relationship between these energies that favors island formation is described by an inequality equation:

$$\gamma_{sv} < \gamma_{cs} + \gamma_{cv} \quad (2.4)$$

where γ_{sv} is the substrate-vacuum surface energy.

Equation (2.4) is satisfied when the contact angle, α in eq. (2.3) is greater than zero, at which condition, island growth becomes dominant.

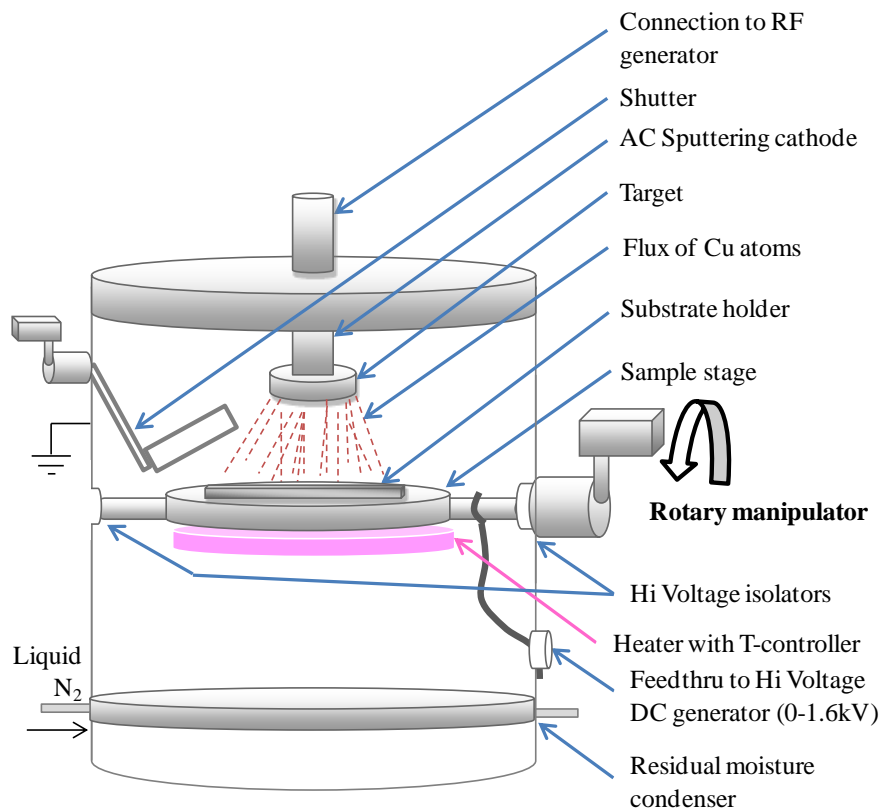


Fig. 2.6: Schematic of the deposition system, showing the possible orientation of sample stage relative to the target.

The formation of np-Cu's in our setup can be understood in terms of the V-W growth mode. Figure 2.6 shows a schematic representation of the sample stage and the sputtering cathode, which form part of our deposition system. Previously cleaned substrate are fastened to the sample holder and clamped to the sample stage. With the rotary manipulator, we can control the start and duration of the substrate exposure to the impinging flux of Cu atoms. We allow 10 minutes stabilization time, after plasma is initiated. During this time, the sample stage and the substrate are turned face down. Evolution of nanoparticles starts as soon as we rotate the substrate to face the target. In the first one minute uniform distribution of high density clusters are formed on the substrate. In other words, when the substrate is exposed to the flux of neutral Cu atoms, the atoms begin to stick on the substrate by nucleation. In this early stage, the prior nuclei incorporate impinging atoms and grow in size. As shown in the AFM topography of Fig. 2.7, the morphological evolution is characterized by a transition from high density but uniformly distributed species to multiply-connected particles to isolated, but relatively large sized, Cu

particles. The morphological evolution is therefore consistent with V-W mode. In this case the isolated particles grow in both in- and out-of-plane direction with further deposition time. The merging together of island by coalescence phenomenon therefore delays the formation of planar or continuous film.

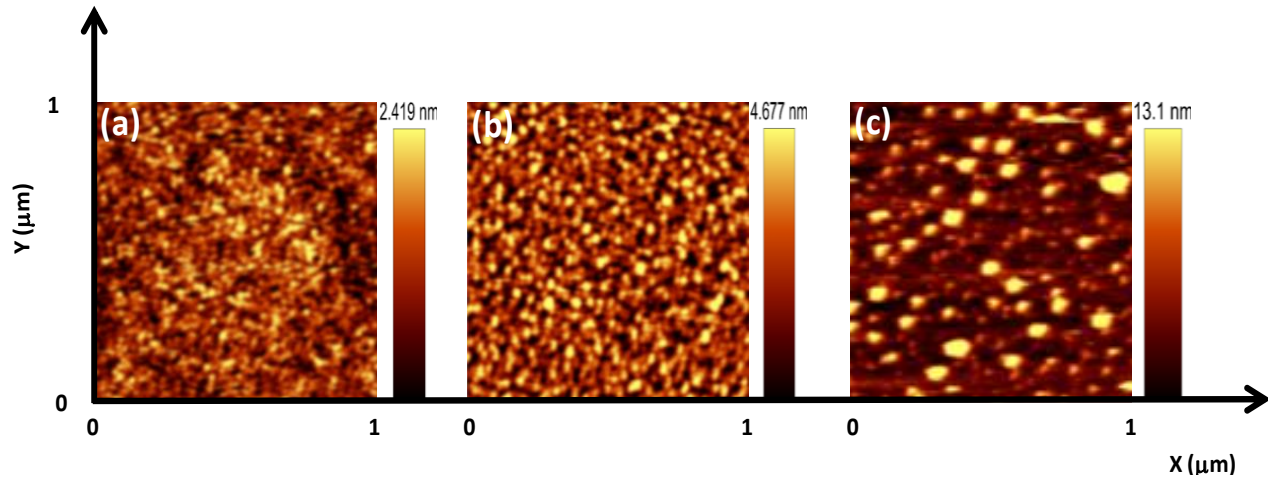


Fig. 2.7: AFM images of np-Cu's on Si substrate showing morphological evolution for three different sputtering times of (a) 1 min, (b) 3 min and (c) 5 min deposited with constant RF power.

2.3 Introduction of Argon in the growth chamber

A flow of gas into the chamber is used to control the chamber pressure during RF sputtering. A mass flow controller is used to regulate the flow of argon gas, used as process gas for our deposition. The mechanism that controls the gas flow rate in a mass flow controller is described schematically in Fig. 2.8.

The sensor circuit, which comprises of a solenoid valve unit, delivers an output voltage that depends on the amount of gas passing through the valve from the by-pass connection. The design of the by-pass ensures that gas flow through the solenoid valve is proportional to the total mass flow in the controller. The flow through the valve produces a temperature gradient that is proportional to the mass flow. The sensor circuit thus generates a linearized DC signals based on this temperature gradient. The signal ranges from 0 – 5 V, with a zero volt signifying 'no flow' and 5 V, a full scale flow. A set point knob in the control unit helps to regulate the flow to the desired flow rate, measured in standard cubic centimeter per minute (SCCM).

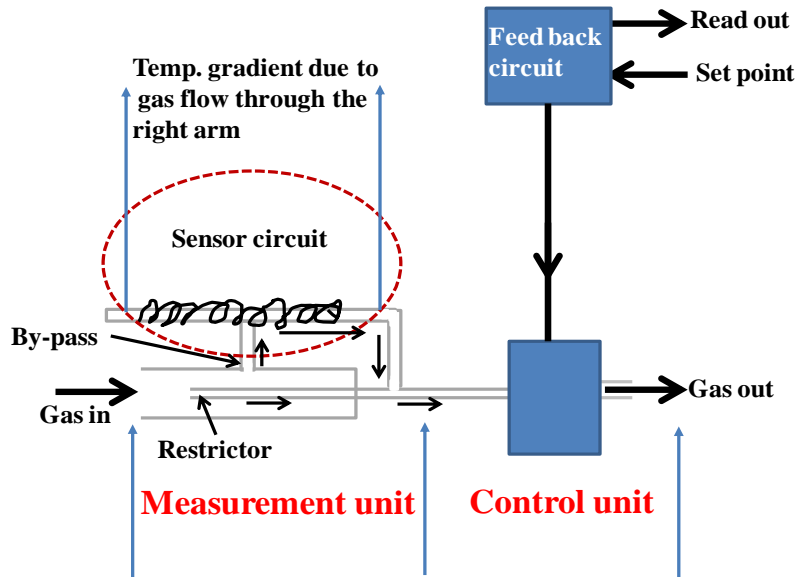


Fig. 2.8: Schematic of the flow meter used for our experiment

In order to control the flow of argon gas into the chamber, we connect the output of the flow meter (OMEGA, FMA5508, range: 0 – 100mL/min) shown in Fig. 2.9 to the chamber with a stainless steel pipe. Argon comes from a 50 – liter-capacity argon cylinder purchased from Praxair Canada Inc.



Fig. 2.9: Picture of the mass flow controller used to control argon flow rate during RF sputter deposition

2.4 Substrate bias voltage

The quality of the films and nanoparticles grown by sputtering depends on the energy of the ions impinging the substrate. Therefore, accelerating the precursor ions towards the substrate can improve/decrease the deposition rate at a constant RF power or, also, affect the density of the films from porous films/nanoparticles into compact films.

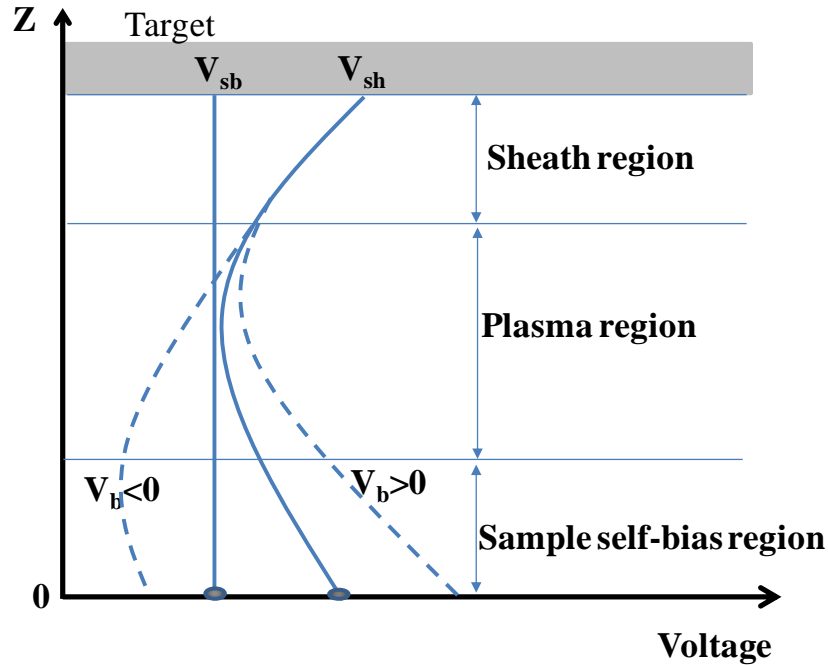


Fig. 2.10: Schematic representation of the three regions in an RF deposition chamber and the voltage close to the target V_{sh} , self-bias voltage on the sample V_{sb} and the external bias voltage V_b .

As shown previously in eq. (2.1) and in Fig. 2.10, the self bias voltage, V_{sb} is smaller than the sheath voltage V_{sh} , close to the target because the sample base is designed to have larger surface area compared to the target. Based on the areas of the two electrodes in our deposition system, the relationship between these two voltages is given by:

$$V_{sb} \approx 0.1xV_{sh} \quad (2.5)$$

However, Fig.2.10 shows that we can change the value of the V_{sb} with additional bias voltage, $V_{ext,b}$ applied to the sample. The total bias voltage then becomes;

$$V_{b,TOT} = V_{sb} + V_{ext,b} \quad (2.6)$$

The $V_{ext,b}$ can be positive or negative. A positive $V_{ext,b}$ increases the values of $V_{b,TOT}$ and hence the energy of the precursor ions accelerating towards the substrate. The opposite effect is achieved when a negative $V_{ext,b}$ is applied to the sample.

2.5 Experimental facility developed for this project

The equipment assembled for this research work is made up by an integrated system composed of the deposition system and the glove box. The deposition system is inside of a large cylindrical steel vacuum chamber. The height of chamber is about 32'' and the diameter is 12''. A viewport and a fast door, each with 4'' glass windows facilitate viewing and easy access to the chamber. A secondary chamber hosts the diffusion pump used to evacuate the deposition chamber. The pictures of the deposition system and all the accessories are shown in Fig. 2.11 – Fig 2.14.

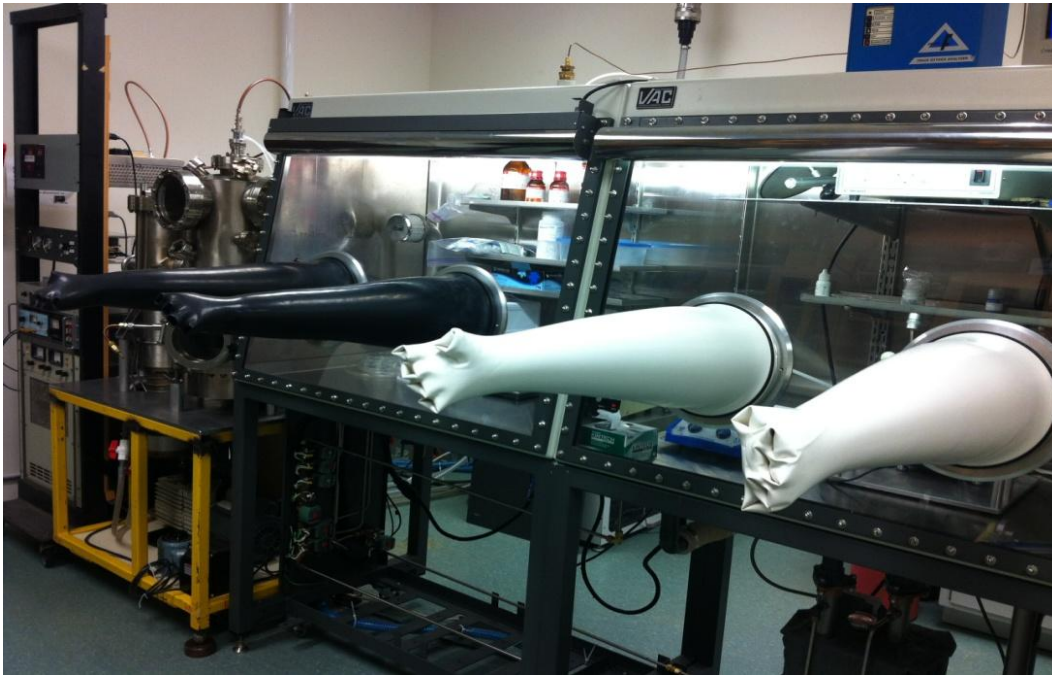


Fig. 2.11 Picture showing an overview of the experimental facility used for our project

The sputtering cathode, obtained from MicroMagnetic Inc. serves as the holder for the sputtering target and couples the radio frequency power to chamber. The cathode is mounted inside the chamber through a stainless steel hybrid adaptor by means of a conflat (CF) flange.

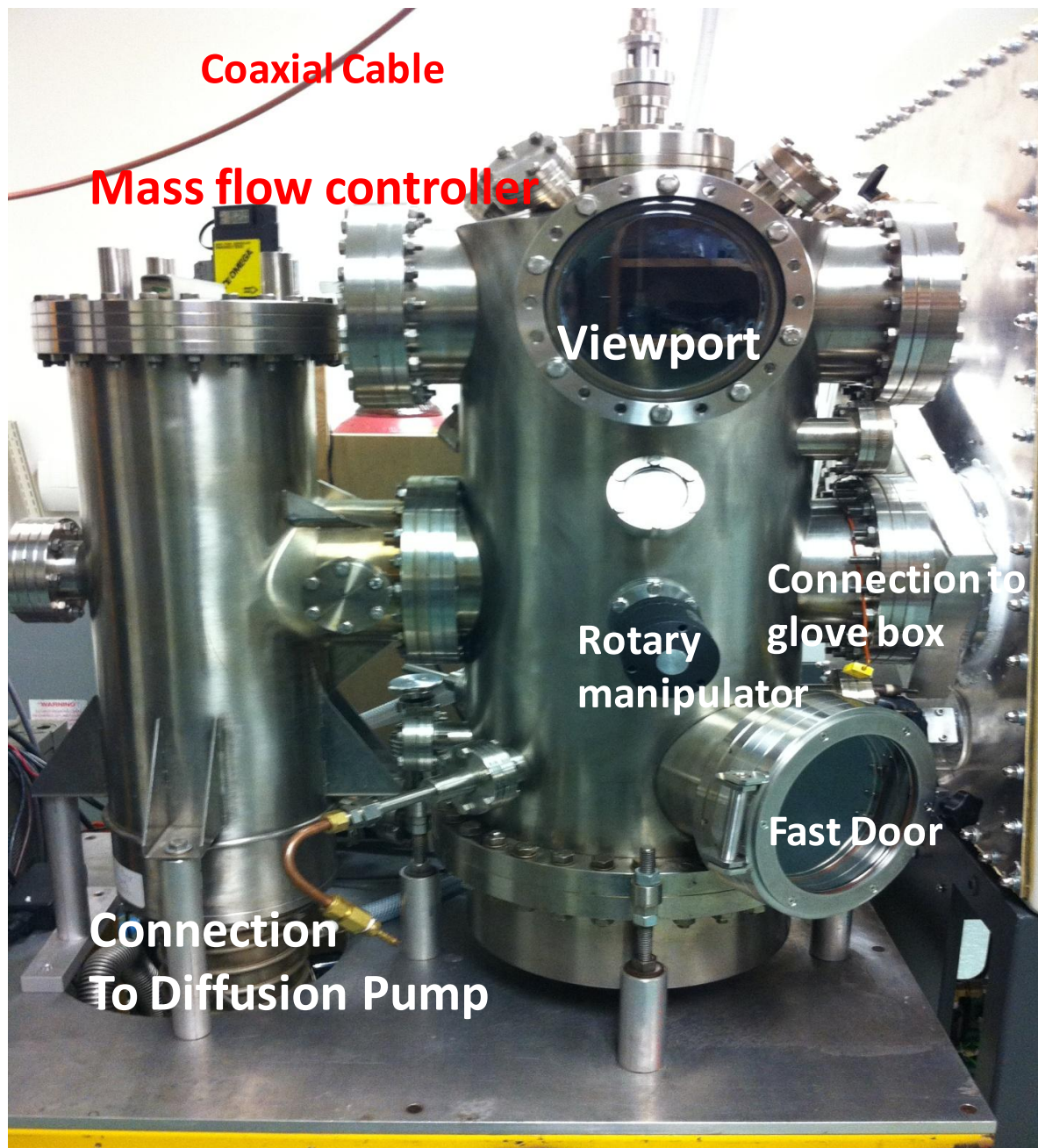


Fig. 2.12 Picture showing a close view of the deposition chamber used for our project

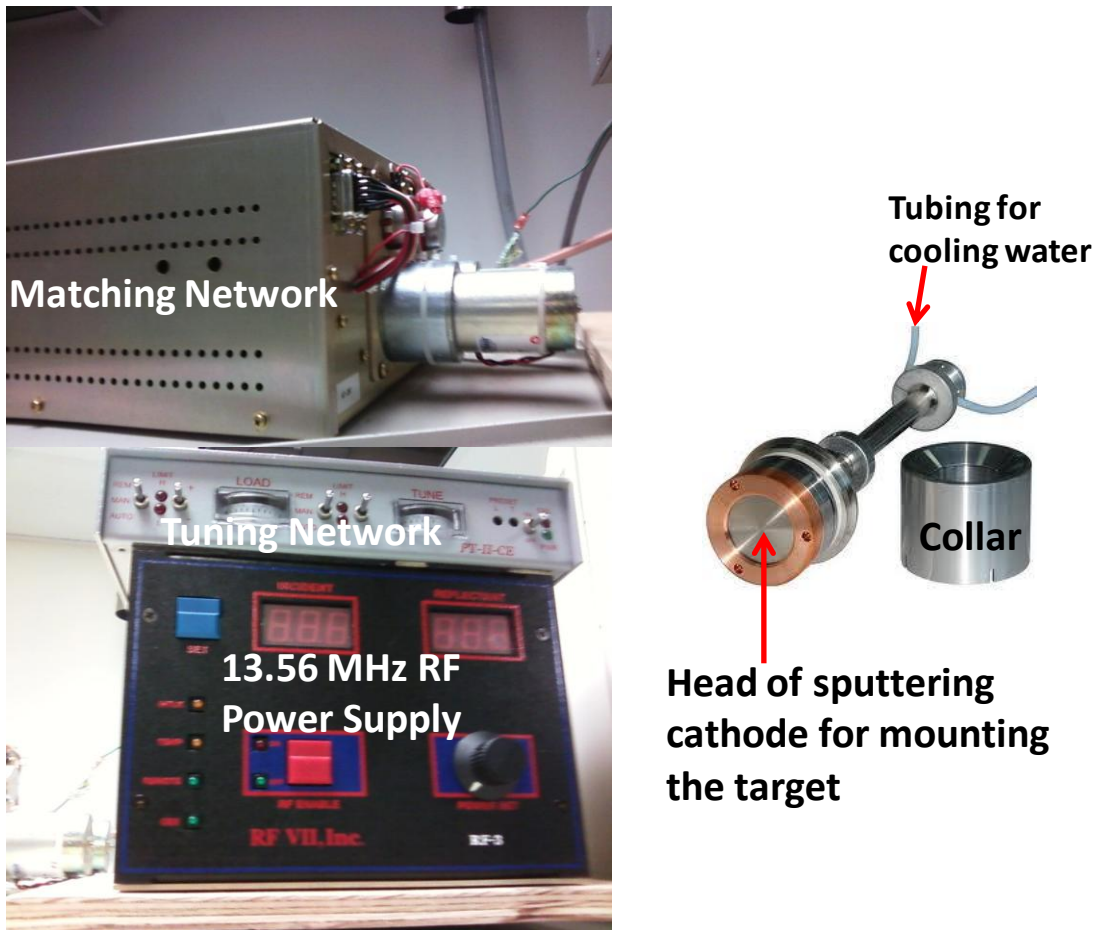


Fig. 2.13: Picture of the basic components of our sputtering system that includes the matching network, tuning network, RF power supply and the sputtering cathode

A vital component of the cathode is the permanent magnet, which in this case is composed of a circular rare earth NdFeB permanent magnet [24]. To ensure that only the target is exposed for sputtering, a stainless steel collar is used to shield the edges of the cathode. Water cooling of the sputter-head is provided in order to prevent heating up the target as well as damaging the system. The cooling water is supplied through a 12'' tubing connected directly to a chiller (HASKRIS, R300) maintained at a constant temperature of 60°F. The chiller itself is supplied with distilled water; to prevent any incidence of short circuiting that may occur while cooling the target. The sputtering head is interfaced with an RF generator through a standard coaxial cable of 50 Ω impedance. The RF generator and the matching network shown in Fig. 2.13 are mounted on a rack positioned very close to the chamber (Fig. 2.14)

In order to deposit np-Cu's, the substrates are mounted on a 3.5'' square substrate holder, made of stainless steel base and brass cover. The sample stage is 6'' from the sputtering cathode and the samples can be shaded during the transitory corresponding to the start up of the discharge with the aid of a rotary manipulator. The attachment to the rotary manipulator as well as the chamber is designed to ensure that the sample stage is electrically floating in the absence of additional electrical connections that are placed only when the substrate is DC – biased. This was realized with the aid of a Teflon rod placed in between two flanges as shown previously in the schematic of Fig. 2.6.

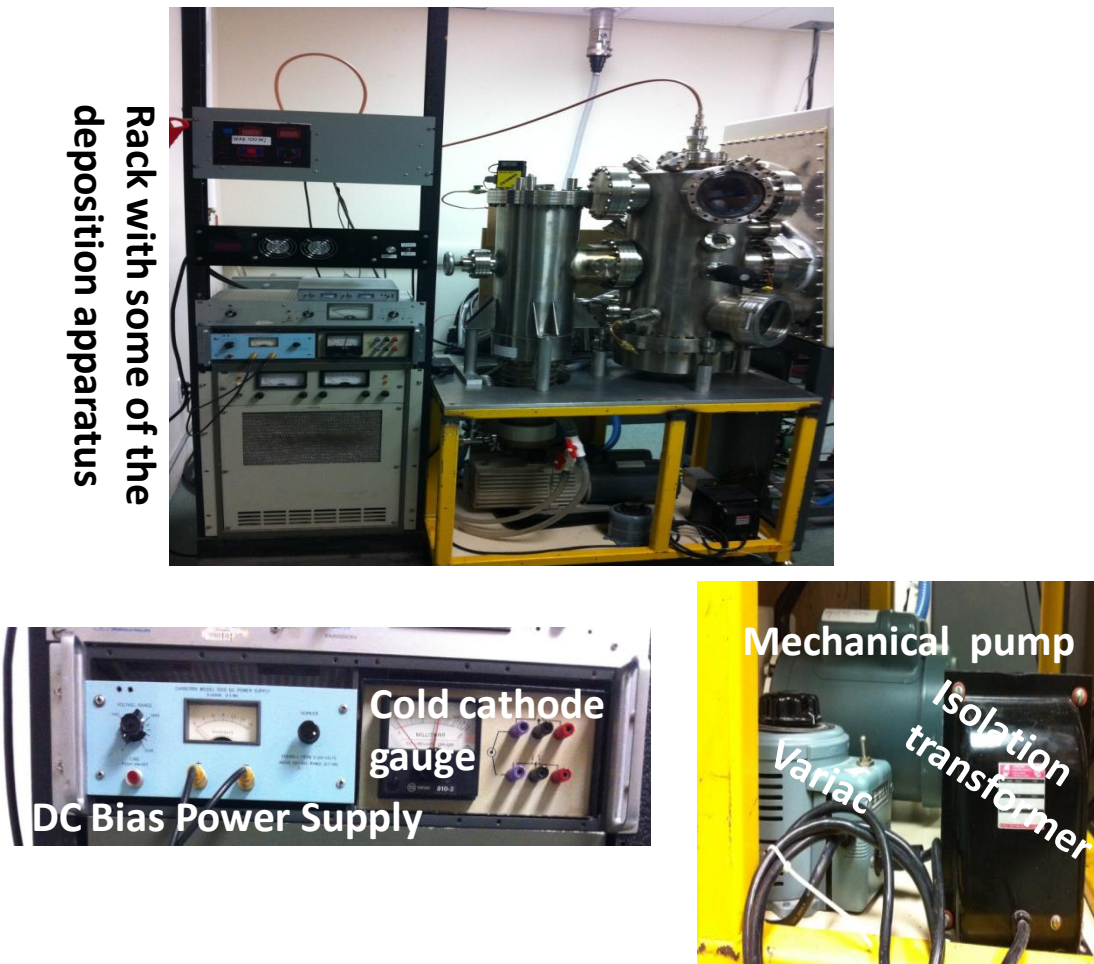


Fig. 2.14: Picture of the deposition apparatus showing a close view of the DC bias power supply, cold cathode gauge, mechanical vacuum pump, Variac and isolation transformer

The sample stage can be biased positively or negatively through the biasing unit. This unit comprises electrical connection and the power supply. The power supply (CANBERRA, 3010 DC power supply) is rated for 1600 V, 5 mA and is secured on the rack as shown in the upper pictures of Fig. 2.14. The biasing voltage is applied to the substrate through the wire attached to the sample stage on one side and connected with the aid of a feed through to the power supply on the outer side. The biasing unit was extensively used during most of the sputtering operations. In particular, it was used to investigate the effect of biasing on the Cu particles size and distribution.

Though substrate heating has not been used during the current project, a substrate heater has also been designed and assembled on the sample stage. In order to maintain the electrical isolation of the sample stage during substrate heating operation, a resistive heater has been attached to the substrate electrode and heating power can be supplied to it through a Variac transformer connected to an isolation transformer. The picture of this unit is shown in Fig. 2.14, and a schematic of the isolation transformer in Fig. 2.15.

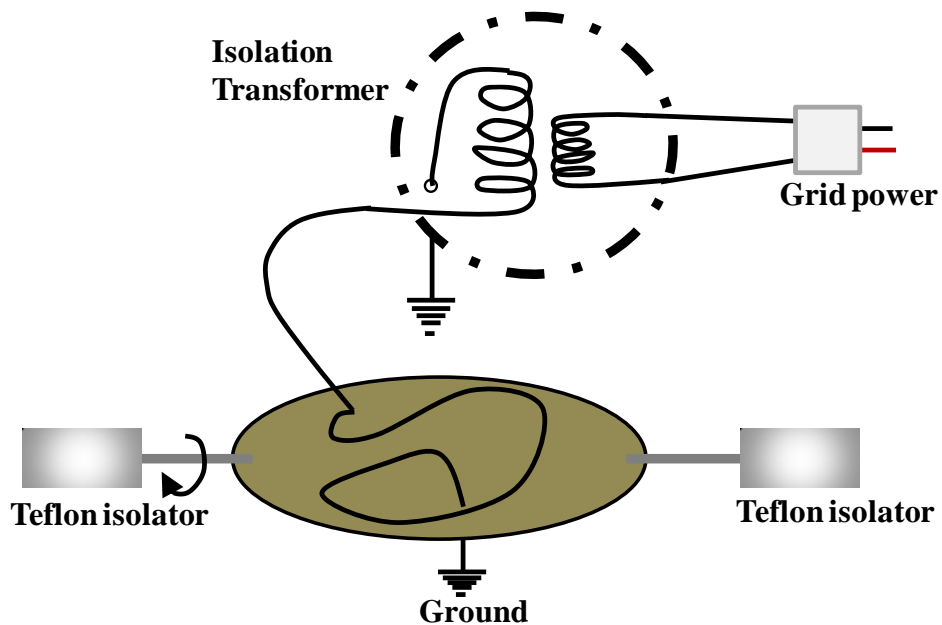


Fig. 2.15: Schematic of isolation transformer showing the connection to grid power and resistive heater

A K-type thermocouple is attached to the substrate using a stainless steel clamp. An ionization gauge attached to the chamber is used to monitor the chamber pressure prior and during any deposition operation. The deposition system is equipped with an oil diffusion pump

(EDWARDS, model No EO2, code No B8013) connected to the lower end of a secondary chamber, shown in Fig. 2.12. A valve connection between two chambers ensures that the deposition chamber can be vented with nitrogen to be accessed while the smaller chamber is constantly kept in vacuum. To reach the required base vacuum for the operation of oil diffusion pump, mechanical pump (ALCATEL, AM632231) is used. Base vacuum is measured with a cold cathode vacuum gauge (VARIAN 810 – 2).

The greatest challenges anticipated were to prevent possible oxidation and degradation associated with exposure of np-Cu's to ambient conditions. The solution to this problem requires that we should be able to interact between the glove box and the deposition system without going through the ambient atmosphere. A high vacuum gate valve was all there is to realize this purpose. The gate valve is connected between the chamber and the glove box (VAC, NEXUS, 100027 - 100062) and can easily be opened when the pressure in both ends is the same. The nitrogen for venting the chamber is taken from the glove box and ensures that no damage is sustained due to pressure imbalance.

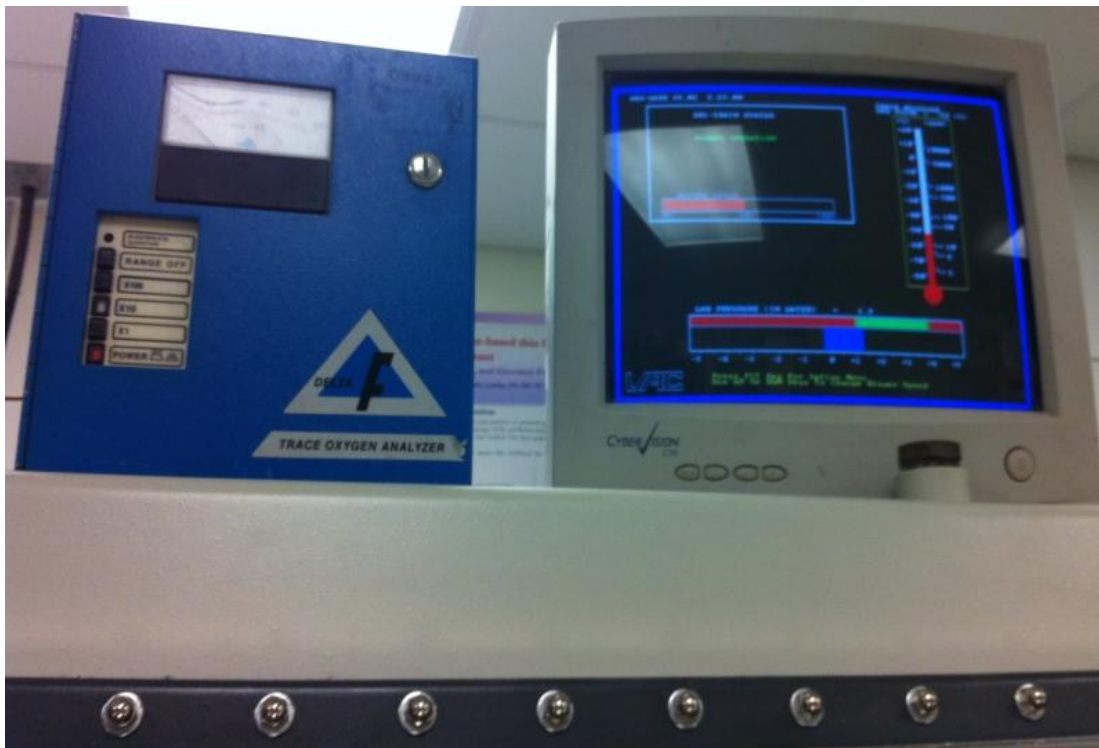


Fig. 2.16: Picture of Trace Oxygen Analyzer (left) and Computer monitor interfaced with the Glove box

In this way, samples can be taken into the chamber and back to the glove box without exposure to the ambient condition. The np-Cu's are thus stored in oxygen free glove box. As shown in Fig.2.16, the oxygen content in the glove box is monitored with an oxygen analyzer (DELTA corp. Trace Oxygen Analyzer, FA3555OSA) while other parameters such as the water pressure in vacuum, purity of the inert environment are monitored through a computer interfaced with the glove box.

2.6 Conclusion

In this chapter, we described the equipment used for the deposition of np-Cu's we report in this project that includes the deposition chamber, RF source and control, the vacuum system, power supply systems, the glove box and the monitoring units. The important aspect of our system design includes integration of the deposition chamber with the glove box that helps to avoid contamination and oxidation of the deposit, control of the ion energy with a DC bias voltage and the installation of isolation transformer that helps to avoid grounding of the deposition chamber, in case of heating the substrate.

2.7 References

- [1] P. K. Khanna, S. Gaikwad, P.V. Adhyapak, N Singh, R. Marimuthu, Mater Lett, **61**, 4711 (2007)
- [2] A. K. Khanna, T.S. Kale, M. Shaikh, N.K. Rao, C.V.V. Satyanarayana, Mater. Chem Phys. Doi:10.1016/j.matchemphys.2008.01.013 (2008)
- [3] M. Kogiso, K. Yoshida, K. Yase, T. Shimizu Chem. Commun. 2492 – 2493 (2002)
- [4] P.K. Khanna, M Priyesh, J Jadish, P. Yogesh and N. Koteswar Rao, J. Nanopart Res. **11**, 793 (2009)
- [5] B.K. Park, S. Jeong, D. Kim, J. Moon, S. Lim and J.S. Kim, J. Colloid Interface Sci. **311**, 417 (2007)
- [6] M. Ohring, *The Material Science of Thin Films*, Academic Press, 1992

- [7] W.R. Grove, Philosophical Transactions, **142**, 87 (1852)
- [8] J. Robertson, Mater. Sci. Eng. **R37**, 129 (2002)
- [9] T. Ghodselahi, M.A. Vesaghi, A Shafiekhani, A. Baradaran, A. Karimi and Z. Mobini, Surface & Coating Techno **202**, 2731 (2008)
- [10] A.B. Glaser and G. E. Subak-Sharpe, *Integrated Circuit Engineering*, Addison- Wesley , Reading, MA (1979).
- [11] J. Roth, in R.E.H. Clark, D.H. Reiter (Eds.), *Nuclear Fusion Research*, Springer, 2005, p.204
- [12] P.Sigmund, Sputtering by ion bombardment: theoretical concepts, in *Sputtering by particle bombardment I*, edited by R. Behrish, Springer-Verlag, 1981
- [13] G.M. McCracken, Rep. Prog Phys. **28**, 241 (1975)
- [14] M.A. Karolewski and R.G. Cavell, Surface Science, **480(1)**, 47 (2001)
- [15] A.H. Dogar and A. Qayyum, Nuclear Instruments and Methods in Physics Research B **247** 290 (2006)
- [16] M.Fqih, E. Ait and P.G.Fournier, Nuclear Inst. and Methods in Physics Research, B, **267(7)**, 1206 (2009)
- [17] K. Wittmaack, Appl. Surf. Sci., **252(19)**, 6413 (2006)
- [18] F.C. Frank and J.H. van der Merwe, Proc. Soc. London A **198**, 205 (1949)
- [19] M. Volmer and A. Weber, Z. Phys. Chem. **199**, 277 (1926)
- [20] A. Y. Cho and J. R. Arthur, Prog. Solid State Chem. **10**, 157 (1975)
- [21] M. Zinke-Allmong, Thin Solid Films **346**, 1 (1999)
- [22] L.E. Murr, *Interfacial Phenomena in Metals and Alloys*, Addison-Wesley, Reading, MA, (1975)
- [23] C.H.P. Lupis, *Chemical Thermodynamics of Materials*, Elsevier, New York, (1983)
- [24] http://www.directvacuum.com/PDF/SpinTron_brochure

Chapter 3

3 Morphological and Optical properties of copper nanoparticles obtained from radio frequency sputtering

In this chapter, I will present the morphological changes of copper nanoparticles (np-Cu's) as a function of growth parameter together with their optical properties and analysis on the results. The optical properties of np-Cu's and, specifically the position of the plasmonic resonance in np-Cu's can be blue – or red – shifted according to the particles sizes and distribution [1]. Hence, an important part of my thesis work has been committed to understanding the parameters that controls the size, shape and distribution of np-Cu's deposited by radio frequency (RF) sputtering. We studied the effect of process parameters such as substrate biasing, the chamber partial pressure (controlled by the argon flow rate) as well as the RF (source) power used during the sputtering process.

3.1 Deposition and protection of copper nanoparticles

3.1.1 Sample Stage

The sample stage used for the growth of np-Cu's is a platform where the substrate holder is mounted inside the sputtering chamber. In Fig. 2.6, it is showed that in our apparatus, the stage is heed by two non-conducting Teflon rods. This arrangement is important in order to have the substrate that can be electrically floating or biased by a dc voltage as may be desired and not necessarily connected to the ground through the body of the vacuum chamber. During the course of this research, two different sample stages were assembled and used for the deposition of np-Cu's. Each one is made of four-inch-diameter metal plate. The regular stage (used for most of the deposition) is made of stainless steel metal; with a clamp for attaching the substrate holder during deposition. A schematic of this sample stage is shown in Fig. 3.1(a). The second sample stage (and all of the related accessories) was fabricated out of a copper metal sheet and rods and is shown in Fig. 3.1(b). The circular portion of the stage is made from 99.99% copper sheet. The copper plate (99.99% purity) is perforated on all sides except at the central portion of about 2 by 4 inch dimension. Substrates are mounted directly on this part, as shown in the schematic of

Fig.3.1 (b). This special sample stage was designed in an attempt to overcome the problem of high density of interconnected np-Cu ensembles while using the regular deposition stage. In this case, the substrate is turned upside down (backing the target) while strong bias voltage is applied to it during sputtering. Copper atoms accelerating through the tiny holes on the copper plate follow the lines of field due to the strong potential applied to the copper plate to deposit on the substrate.

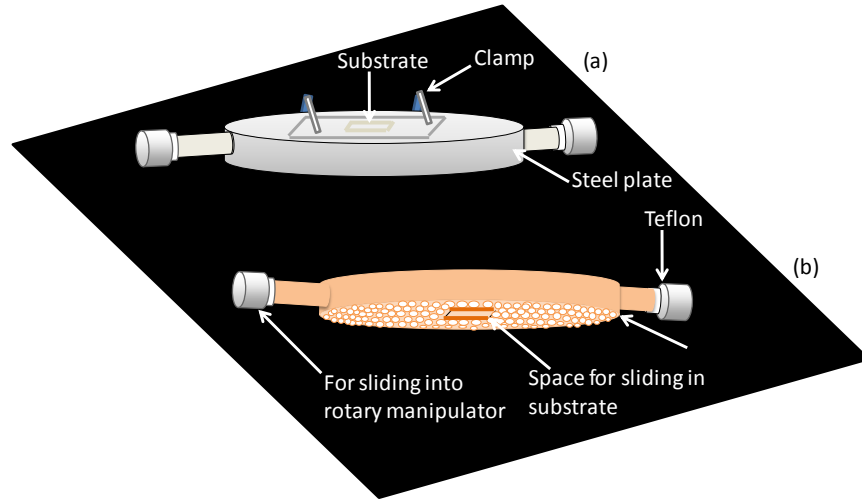


Fig.3.1: Schematic representation of (a) regular and (b) perforated sample stages that can be mounted in the deposition chamber

3.1.2 Preparation for copper nanoparticle deposition

The deposition was carried out on microscope glass and Si substrates. With the aid of a diamond cutter, the Si wafer (100)Si are cut into $\frac{1}{2} \times \frac{1}{2}$ inch square that fit into the substrate holder. This is followed by ultrasonic cleaning of all of the substrate in water with detergent, acetone and methanol for 15 minutes each. The substrates are then exposed to UV/ozone radiation (UV3 Novascan) for 20 minutes to get rid of any oxide residues. UV/ozone treated substrates are immediately introduced into the glove box through the antichamber. From the glove box, the substrates are placed on the deposition substrate holder and covered with a shadow mask which ensures that they remain in position even when turned upside down inside the chamber. To introduce the substrate into the chamber, the chamber pressure is first raised to the same value as

that of the glove box by using the venting system, whose source is also the glove box. It is only in this condition that the gate valve connecting the two systems can be safely opened.

3.1.3 Variation of process parameters and deposition of copper nanoparticles

All the sputtering operation was carried out at a base vacuum better than 5×10^{-6} torr. Sufficiently low vacuum is required in the deposition chamber prior to sputtering to reduce the effect of contamination and oxidation, especially for the case of Cu. Low pressure is also desirable during the actual sputtering operation in order to raise the mean free path of the sputtered species and increase the sputtering rate. Sputtering is initiated by allowing a flow of argon gas into the plasma chamber, at a flow rate determined by the mass flow controller. As previously described, the substrate can float, biased or connected to ground as may be desired.

Three different set of depositions were performed: first set at varying RF power, second set at increasing substrate bias voltage and a third set at increasing argon flow rate (see Tables 3.1 – 3.3). In the set grown at different RF powers, the sputtering time was 2 minutes because of increased rate of sputtering at RF power greater than 75 W. The substrates for the deposition were microscope glass and Si (100). In the set at varying argon flow rate, the change in gas flow also varied the gas pressure as shown in Fig. 3.2.

Table 3.1: Sputtering parameters for deposition at different RF powers

Ar flow rate (SCCM)	RF power (W)	Sputtering Time (min)	Substrate bias voltage (V)	Stage used (see Fig. 3.1)	Substrate Temp. (°C)
10	33	2	Float	Regular	85
10	55	2	Float	Regular	122
10	75	2	Float	Regular	160
10	100	2	Float	Regular	197
10	120	2	Float	Regular	225

Table 3.2: Sputtering parameters for deposition at different substrate bias voltages

Ar flow rate (SCCM)	RF power (W)	Sputtering Time (min)	Substrate bias voltage (V)	Stage used (see Fig. 3.1)	Substrate Temp. (°C)
20	55	3	0	Regular	134
20	55	3	- 100	Regular	129
20	55	3	- 150	Regular	117
20	55	3	- 200	Regular	105
20	55	3	- 300	Regular	82
20	55	3	- 400	Regular	69

Table 3.3: Sputtering parameters for deposition at different argon flow rates

Ar flow rate (SCCM)	RF power (W)	Sputtering Time (min)	Substrate bias voltage (V)	Stage used (see Fig. 3.1)	Substrate Temp. (°C)
6	75	3	Grounded	Regular	239
9	75	3	Grounded	Regular	224
12	75	3	Grounded	Regular	208
15	75	3	Grounded	Regular	190
18	75	3	Grounded	Regular	180
20	75	3	Grounded	Regular	125

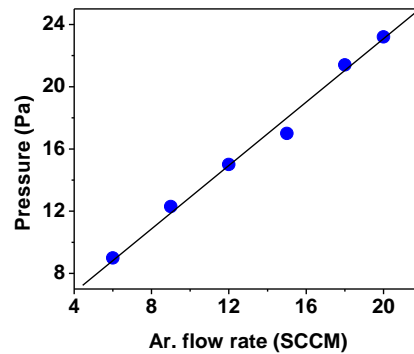


Fig. 3.2: Variation of sputtering chamber pressure with the argon flow rate

3.1.4 Energy dispersive x-ray spectroscopy measurements

In order to protect the deposited np-Cu's from oxidation due to exposure to normal atmospheric condition, the deposited samples were stored in the glove box after they are retrieved from the sputtering chamber. To verify the level of damage the exposure can cause, we carried out energy dispersive x-ray spectroscopy (EDX) analysis of two samples deposited under exact similar conditions using LEO (Zeiss) 1530 field emission scanning electron microscopy (SEM). SEM produces topographical information as well as providing chemical composition information near the surface of material.

The first sample was taken out of the glove box immediately before being measured (with a dwell time no more than 10 minutes before being admitted in the SEM/EDX chamber) while the second sample was exposed in air for 24 hours prior to the EDX analysis. The result of these measurements is displayed in Fig. 3.3. The ratio of atomic content of Cu and O shows that the sample exposed to air for 24 hours has been severely oxidized. For the case of the sample taken directly from the glove box, the observed O in the EDX spectra occurs in trace quantity and therefore may not necessarily be associated with copper oxide. It may have come as a residual content of the substrate prior to sputtering. From these measurements, we conclude that the samples are relatively protected from oxidation as long as they remained in the glove box.

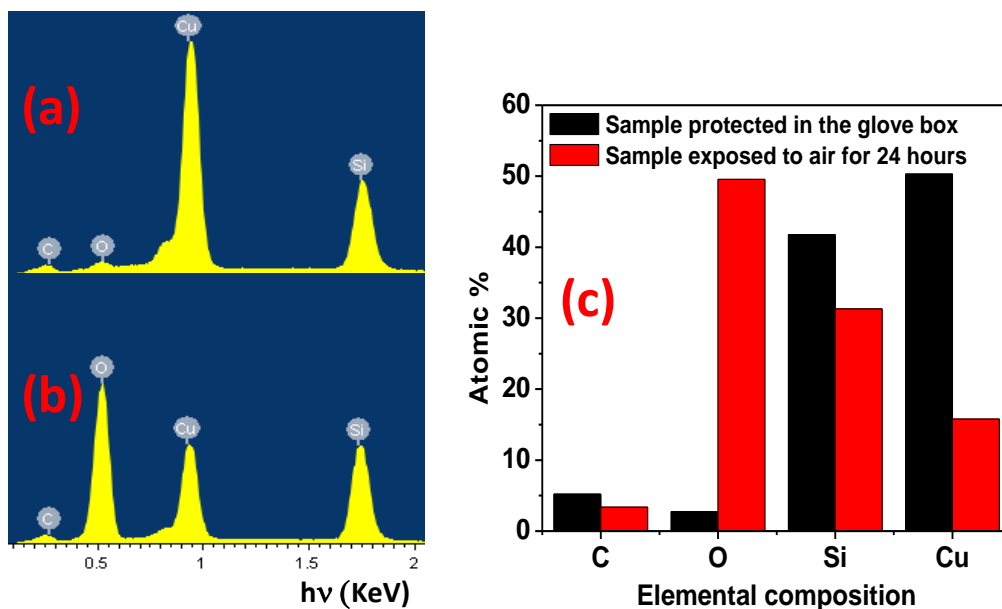


Fig. 3.3: EDX spectral showing the composition of np-Cu sputtered on Si substrates for the case of (a) sample protected in the glove box, (b) samples exposed to oxidation environment for 24 hours prior to the analysis. (c) Comparison of (a) and (b)

3.2 Characterization equipment

3.2.1 Atomic force microscopy

The surface analysis and morphological mapping on the nanoscale for np-Cu's were studied using a Witec Alpha 300S atomic force microscope. The system can be used to perform a wide range of experiments such as Atomic Force Microscopy (AFM), Scanning Near Field Optical Microscopy (SNOM), Confocal Raman Imaging and Electrostatic Force Microscopy (EFM). In this work, the AFM and SNOM techniques were used to determine the surface topography and near field optical imaging of the samples. During normal operation, an atomic force microscope is very sensitivity to mechanical vibrations, electromagnetic waves as well as acoustic noise. For this reason, the AFM is placed in an anti-damping box, with an air-pressured based and aluminum foil protection during all of the operations we report in this thesis.

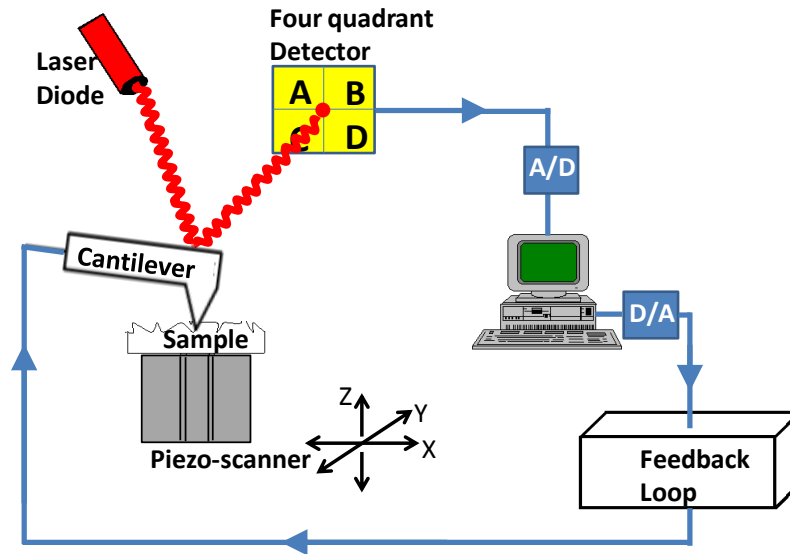


Fig. 3.4: Schematic of AFM during operation, with control and feedback mechanisms

As shown in Fig. 3.4, the basic components of AFM set up consists of probes, laser diode, four quadrant detector, feedback loop and piezoelectric scanner. The system is interfaced with a desktop computer for controlling the different parts and, for collating data. The investigation of sample surface topography can be performed in three different modes as shown in Fig. 3.5. These three modes of operation differ mainly by the amount of the interaction force between the probe tip and the sample surface [2].

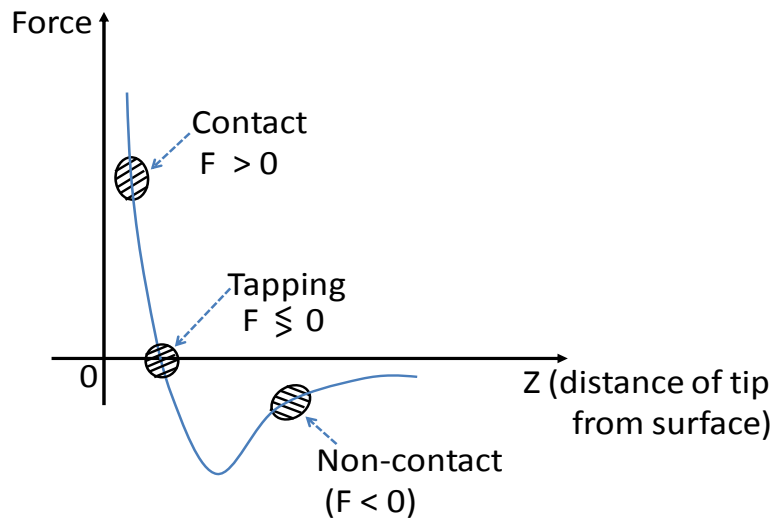


Fig. 3.5: Atomic interaction forces between the AFM tip and the sample surface, which define the modes of AFM operation into contact, non-contact and tapping modes.

As shown in Table 3.4, when an AFM tip is within a few angstrom distances from the sample surface a repulsive force, due to the overlap of electronic orbitals at atomic distances, appears between the two interacting objects (i.e. between the tip and the sample). This repulsive force which becomes predominant as the tip gets very close to the sample can be very strong and, the tip is assumed to be in contact with the sample surface. On the other hand, operation in tapping and non-contact modes is based on a feedback mechanism of constant oscillation amplitude with the tip – surface force defined as shown in Table 3.4.

Table 3.4: Properties of contact, tapping and non –contact modes of AFM configuration

Contact	$F > 0$	Decreasing with Z
Tapping	$F \lesseqgtr 0$	$F > 0$ at $Z < Z_0$ $F < 0$ at $Z > Z_0$
Non Contact	$F < 0$	Increasing with Z

For most of the results presented in this thesis, the AFM was operated in tapping mode. During a sample scan in this mode, the cantilever is oscillating at a fixed frequency, f close to the resonance frequency, f_0 (i.e. $f = f_0 \pm \delta f$) and the amplitude set as $\sim 50 - 60\%$ of free amplitude A_0 . The tip-sample interaction force initiate changes in the cantilever vibration amplitude A , which depends on the distance to the sample surface (Fig. 3.5). The feedback mechanism operates in a way that adequately maintains constant cantilever vibration amplitude, by adjusting the vertical position of the piezo-scanner on which the sample is mounted. For each of the scans, the topography is mapped by maintaining a constant damping of the amplitude defined by A/A_0 [3]. The cantilevers have to be stiff enough in order to detach the cantilever from the surface (cantilever spring constant $k_c > 1\text{N/m}$) and the resonance frequency of the cantilever is selected to be far above the resonance frequency of any other mechanical component of the instrument ($f_0 > 10\text{kHz}$, typically larger than 50kHz) [3]. In order to probe the motion of the tip, the beam of a laser diode is aligned to the cantilever, which is then reflected to the four quadrant detector as the

sample surface is scanned. The signal on the four quadrant detector is used for the feedback control of vertical position of the scanner. The driving amplitude as well as the set point is selected to achieve clear and noise free topographic images. The set point indicates the closeness of the tip to the sample surface.

3.2.2 UV-VIS transmission spectrophotometry

UV-VIS transmittance of our samples was measured at normal incidence in a range of wavelengths between 350 nm and 800 nm using a Varian DMS80 spectrophotometer. A schematic diagram showing the major optical components of a spectrophotometer is shown in Fig. 3.6. A broad spectrum of white light from a tungsten source is selectively focused on the rotating beam splitter by the mono-chromator. Part of the light from the beam splitter serves as the reference beam while the second part serves as the sample beam. The instrument records directly the transmittance of a test sample by measuring the percentage of light transmitted through the sample relative to that of a reference beam at specific wavelengths. If I_o is the intensity of reference light beam and I the intensity of the transmitted light through the sample, then the transmittance T can be defined by

$$T = \frac{I}{I_o} \quad (3.1)$$

A routine procedure is to perform a scan of the reference substrate in the range of wavelength of interest. Repeat measurement is then carried out with the test sample placed in the sample cuvette while the reference substrate remains in the reference beam.

The transmittance data of our samples were obtained at a step scan of 10 nm per second in a range of wavelengths between 350 nm and 800 nm. Transmittance data is acquired with the use of matlab program and stored directly in the relevant folder for further analysis.

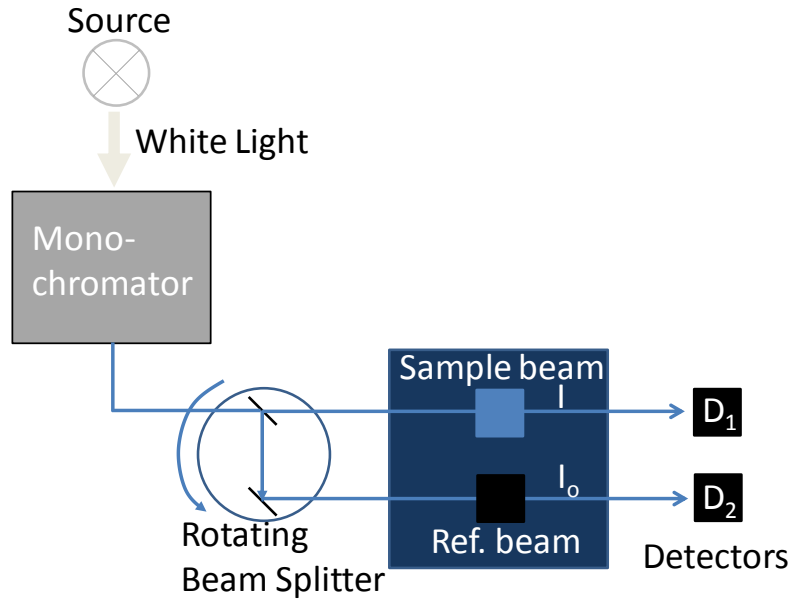


Fig.3.6: Schematic diagram of a spectrophotometer

3.3 Results and discussion on dispersed and semi-continuous copper nanoparticles

In this section the results of the morphological and optical characterization of np-Cu's are presented. AFM is used to obtain the dispersion of np-Cu's deposited on glass substrates for different parameter variations. Image J, a free program package for image processing and manipulation [4] was used to process the particle morphology acquired from the AFM scans to obtain the properties and fraction of substrate area covered by the particles. Unfortunately, it is more difficult to obtain the particle size distribution in the case of highly connected copper particles of small size. Such samples are only discussed in terms of fractional substrate area coverage and are called semi-continuous np-Cu's.

3.3.1 Determination of mean particle size and area fraction in dispersed and semi-continuous copper nanoparticles

Fig. 3.7 is a representation of AFM images of np-Cu's deposited as in Table 3.3 for different pressures of the deposition chamber and treated by Image J. The variation in the chamber pressure affects the size and degree of dispersion of np-Cu's as demonstrated in Fig. 3.7.

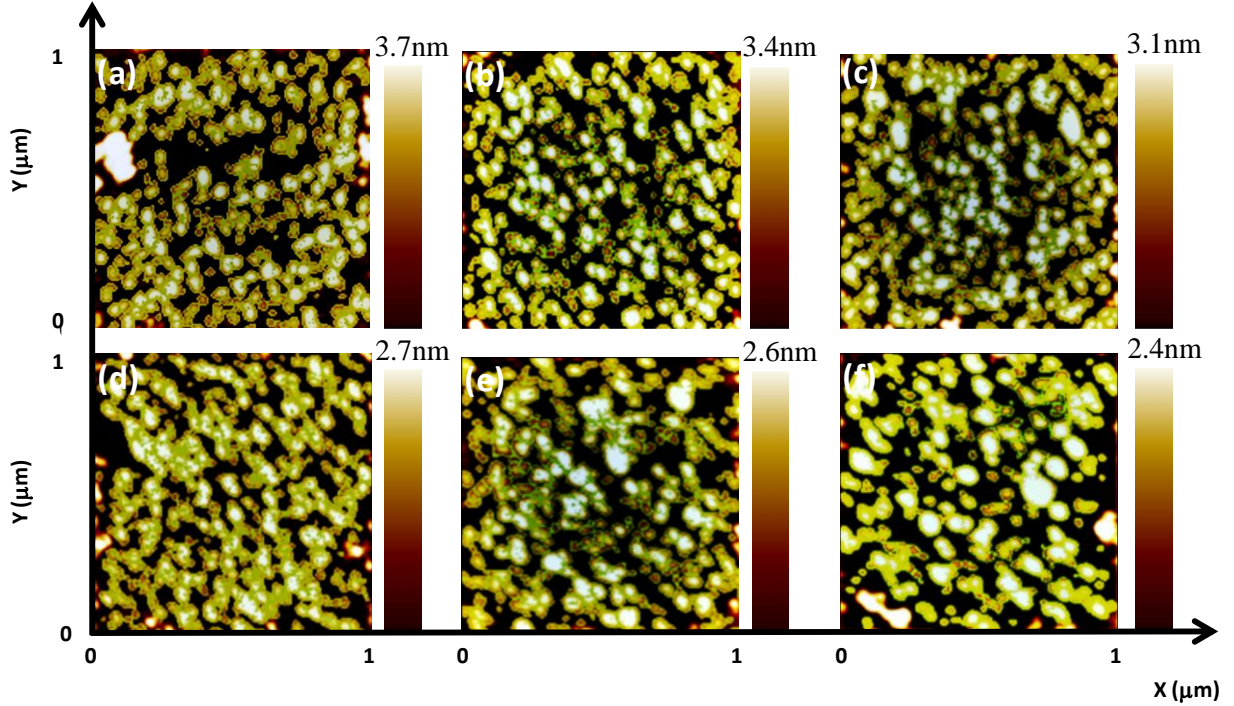


Fig. 3.7: Treated AFM topographic image of np-Cu's deposited in constant RF power at different chamber pressure of (a) 9, (b) 12, (c)15, (d) 17, (e) 21 and (f) 23 Pa

Particles grown at higher pressures exhibit larger particle diameter and are less dense than those grown at lower pressures. The increase in the particles size can be explained in terms of the relationship between the mean free path l (cm), of gaseous Cu atoms and the sputtering chamber pressure P (Pa), as follows:

$$l = 2.330 \times 10^{-20} \cdot \frac{T}{(P \cdot \delta_m^2)} \quad (3.2)$$

Where T is the temperature in Kelvin and δ_m is the molecular diameter of the clusters or molecules that are aggregating in the gas, expressed in cm [5]. From this equation it is clear that higher pressures, obtained at higher argon flow rates, result in smaller mean free path of the gaseous Cu atoms. Consequently the sputtered copper atoms are prone to a large number of collisions and have a higher probability of agglomeration before impinging the substrate. Besides, the mean free path of the gaseous species in the chamber influences the rate at which Cu target is sputtered. Argon ions lose energy by collisions when they are accelerated close to the

target [6]. Therefore the lower the pressure, the more particles involved in the coalescence phenomena that are taking place in the proximity of the substrate surface. This explains the high density of particles and increased growth rate for particles deposited at lower pressures. In view of the above argument, one can say that the size distribution of np-Cu's, shown in Fig. 3.7, results from different mean free path. The observations are summarized in Fig. 3.8. The mean diameter of the particles is presented in Fig. 3.9 as a function of pressure. Coalescence and increase in size is clearly favored at higher sputtering pressure.

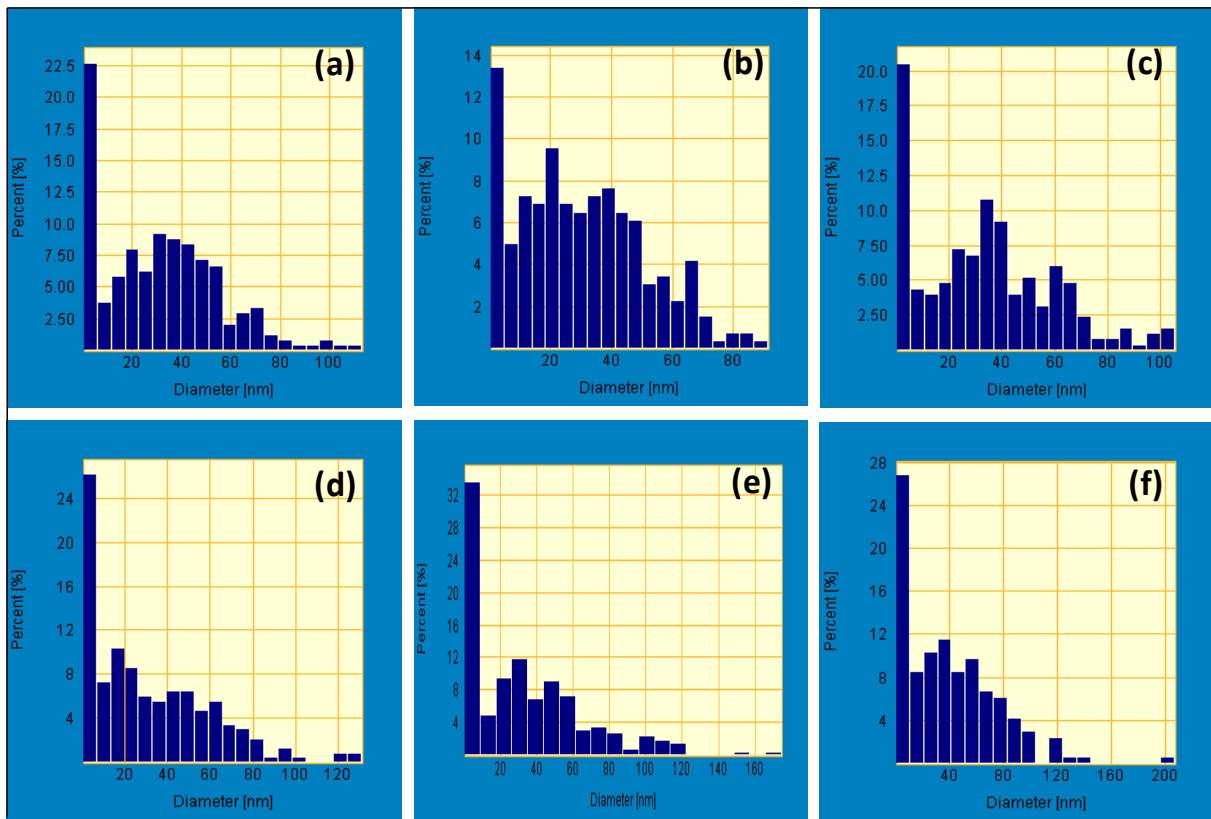


Fig.3.8: Size dispersion of np-Cu's deposited in constant RF power at different chamber pressures of (a) 9, (b) 12, (c)15, (d) 17, (e) 21 and (f) 23 Pa

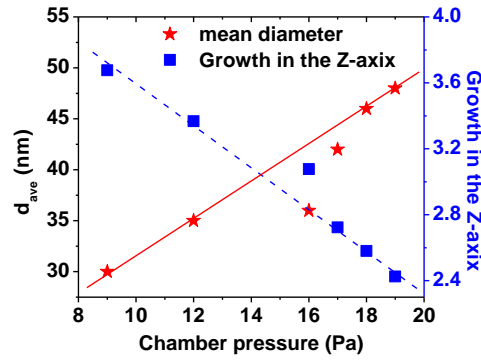


Fig. 3.9: Average diameter and out of plane growth height of np-Cu's obtained from AFM images for np-Cu's sputtered at constant RF power and different chamber pressures

In order to investigate the effect of RF power on the dispersion of the np-Cu's, we will now present our results on samples grown at different RF power, namely, 33, 55, 75, 100 and 120 W, as in Table 3.1. AFM topographic images for this set of samples are displayed in Fig. 3.10. The particles are generally interconnected in these cases. This implies that coalescence prevents island formation and instead, a semi-continuous film is formed. Power is an important parameter that increases the sputtering rate. The sheath voltage V_{sh} (also known as self-bias voltage) close to the target electrode increases with RF power W , since $V_{sh} \sim W/P^{1/2}$, where P is the chamber pressure [7]. Therefore, at a constant chamber pressure, the sputtering rate increases with RF power due to increase of the efficiency at which the argon ions bombard the target. More Cu atoms are subsequently dislodged at higher RF power. The topographic images processed using the Image J software is shown in Fig. 3.11. The figure shows that when the RF power increases at a constant chamber pressure, the particles become more interconnected and grow in size. At even higher RF power, large particles combine together to interconnect across the sample.

The area fraction of the substrate that is covered by copper nanoparticles increases with increasing RF power. The coverage area as a function of RF power is reported in Fig. 3.12. Clearly, sputtering carried out at RF power of 100 W and above, results in large fraction of covered area and may not be suitable for applications requiring high transmission of light through the sample and surface plasmon enhancement. Therefore, all our future experiments will be restricted to 75 W RF power or below.

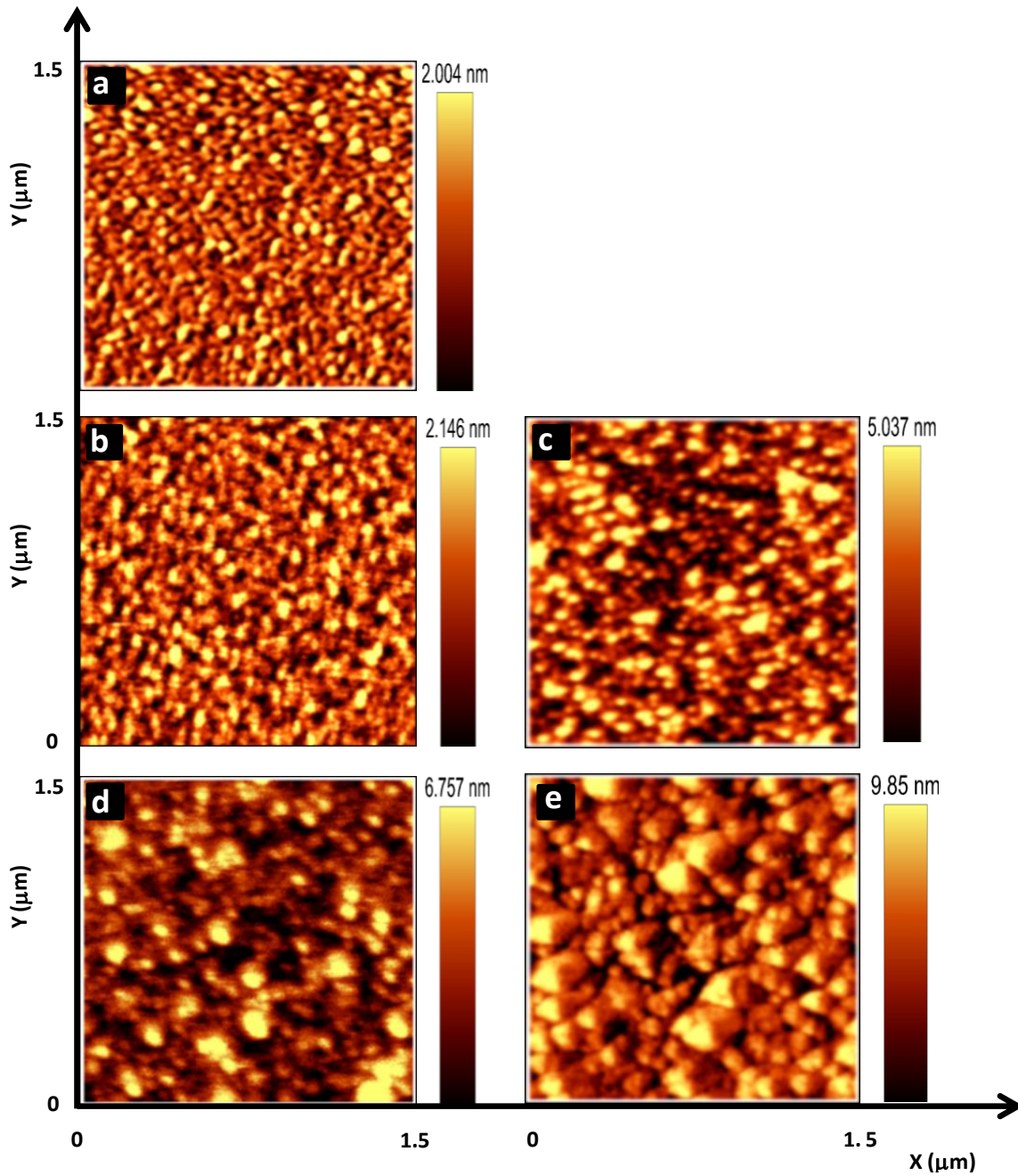


Fig. 3.10: AFM images showing semi-continuous np-Cu's deposited with different RF power of (a) 33 W, (b) 55 W, (c) 75 W, (d) 100 W and (e) 120 W

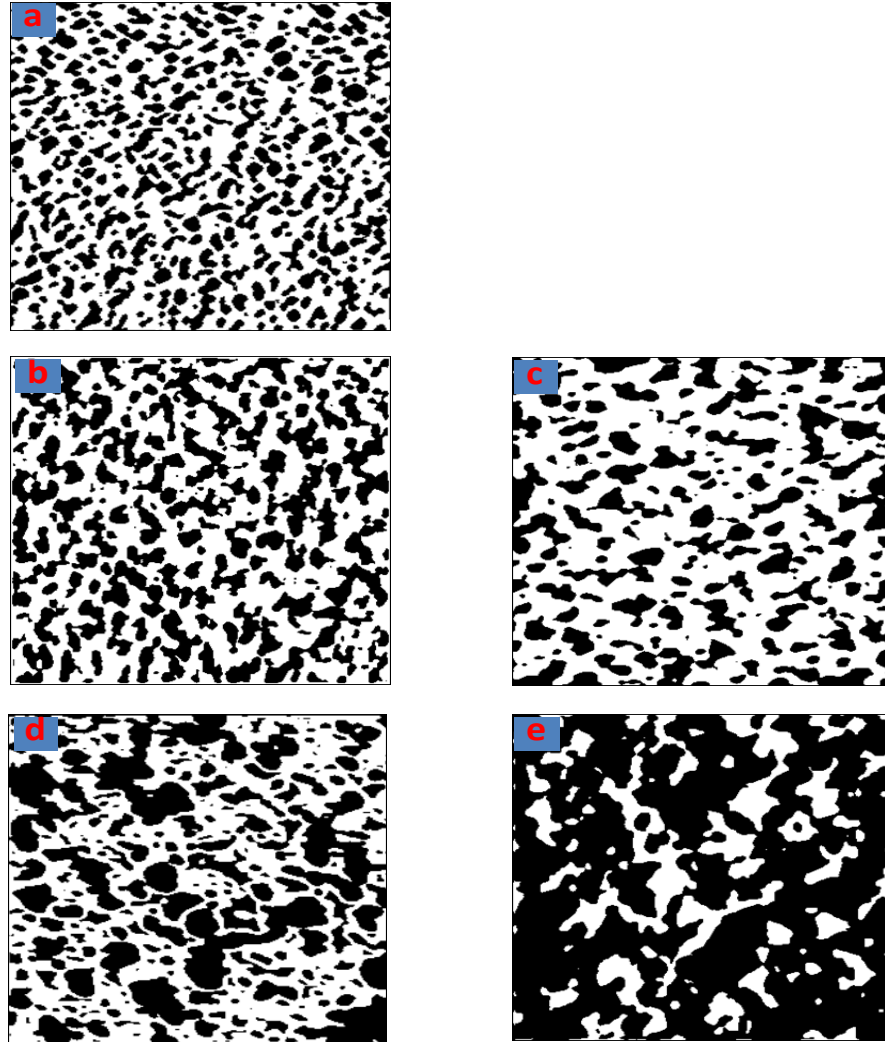


Fig. 3.11: Processed AFM topographic images of semi-continuous np-Cu's sputtered at different RF power of (a) 33 W, (b) 55 W, (c) 75 W, (d) 100 W and (e) 120 W

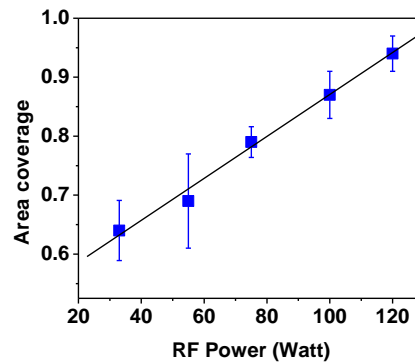


Fig. 3.12: Plot of substrate area covered by semi-continuous np-Cu's as a function of RF power used for the sputtering.

3.3.2 Optical transmittance of semi-continuous copper nanoparticles

The sets of samples used for these experiments are the same as the ones shown earlier in Tables 3.1 – 3.3. For each of these sets, the transmittance of the np-Cu's shows a transmittance enhancement (i.e. a peak in transmittance) at the opposite of plasmonic enhancement (i.e. a dip in transmittance, corresponding to a peak in reflectance) [8, 9]. The transmittance enhancement corresponds to metallic behavior in these samples – the morphology of the np-Cu's shows that the nanoparticles are highly inter-connected.

In Fig. 3.14, we show that the position of the transmittance peak (obtained from Fig. 3.13) decreases up to 548 nm at 17 Pa and then increases for the set of np-Cu's deposited at different pressures (set 3, as in Table 3.3). However, the intensity of the peaks monotonically increases as the sputtering chamber pressure increases, which led to samples with lower density of particles.

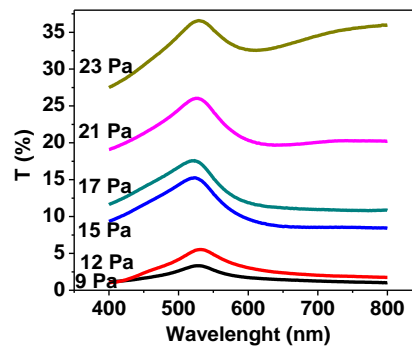


Fig.3.13: Transmittance vs. wavelength for dispersed np-Cu deposited by RF sputtering at different chamber pressures.

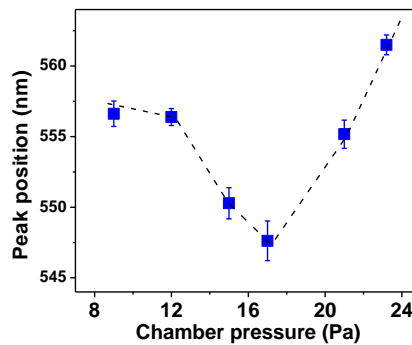


Fig. 3.14: Position of T_{\max} vs. chamber pressure for np-Cu's deposited by RF sputtering

Instead, in the case of samples deposited with different RF powers (Fig. 3.15, set 1 as in Table 3.1), the transmission spectra show a change in intensity with little variation in the peak position. For all of the samples deposited with different RF powers, the particles are evenly spread and the fraction of the substrate covered with np-Cu's is very high; more than 0.6 (see Fig. 3.12). Consequently all the samples have a similar fraction of holes and voids, which are assumed to be responsible for the position of the transmission peak.

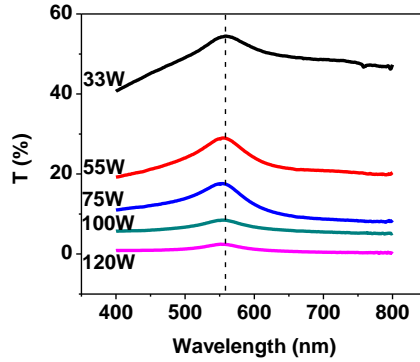


Fig.3.15: Transmittance vs. wavelength for semi-continuous np-Cu's sputtered with different RF power.

Let us now consider the set of samples grown at varying bias voltage (set 2 as in Table 3.2). Fig. 3.16(a) shows that the transmittance peak appears at ~ 540 nm in all of these samples irrespective of the substrate bias voltage. This represents an early stage during the growth process when initial copper nuclei establish on the substrate surface. As the sputtering proceeds, nucleation and coalescence leads to aggregation of the clusters of copper nuclei resulting in morphological variations related to substrate biasing. This is responsible for the shift in the position of the transmittance peak as observed in Fig. 3.16(b).

As shown in the AFM topographic images of Fig.3.18, the samples deposited with high value of substrate bias voltages of -300 V and -400 V have the highest fraction of holes and voids. The transmittance enhancement can be attributed to the nanoparticles morphology in a way that its position depends on the size of the voids and holes that appear in the samples. Since the samples deposited with the substrate grounded appear to have smaller voids and holes, the transmittance peak position shifts to smaller wavelength. The wavelength at which the transmittance reaches a maximum (λ_{\max}) is plotted as a function of the substrate bias voltage in Fig. 3.17, where it can be observed that λ_{\max} increases linearly and fast up to 548 nm for the

sample grown with the substrate bias voltage of -200 V and then slowly increase to 550 nm for the sample grown with the highest applied negative bias voltage.

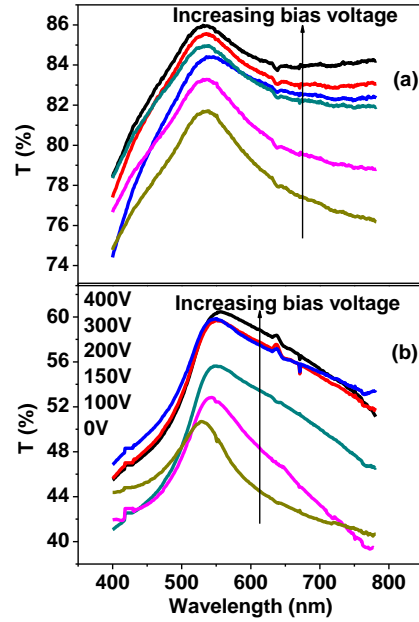


Fig.3.16: Transmittance vs. wavelength for np-Cu's sputtered under (a) 1min and (b) 3 mins at different substrate bias voltages.

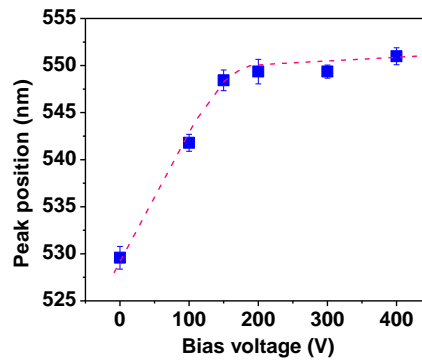


Fig. 3.17: Variation of the position of transmittance peak with substrate bias voltages for np-Cu's deposited with different bias voltages.

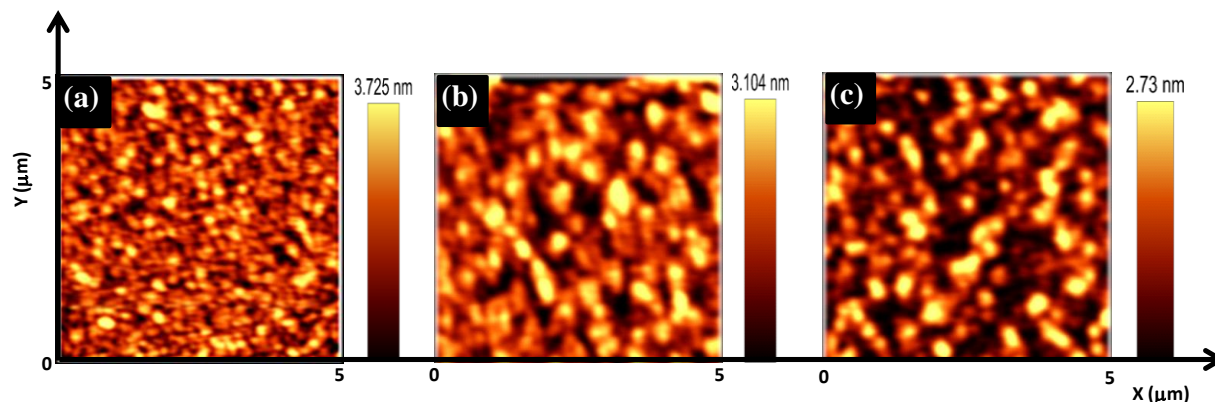


Fig. 3.18: AFM topographic images of np-Cu's deposited by RF sputtering with the substrate (a) grounded and biased by (b) – 300V and (c) -400 V DC voltage.

3.4 Properties of thermally treated copper nanoparticles

3.4.1 Parametric study as a function of treatment temperature

Thermal treatment is an efficient means to activate complete coalescence in semi-connected network of metallic nanoparticles and form metal islands [10 - 12]. However, annealing of np-Cu's in an oxygen environment can lead to its oxidation. To overcome the problem of oxidation during the annealing operation we, again rely on the control of atmospheric conditions in our glove box. For all the heat treatments carried out inside the glove box, the oxygen content was no greater than 5 ppm.

In order to make a comparison, two identical samples were annealed at 300°C for 1 hour, one in the glove box and the second in air. The morphology of the sample was first obtained with AFM prior to thermal treated and re-scanned after it has been annealed. As seen in Fig. 3.19 both samples annealed at different environment conditions show an increase in height, indicating that particle growth has taken place. However, the sample annealed in air did not yield the needed islands of particles but rather a mesh-like network, not quite different from as-grown sample. The sample annealed in the glove box produced significant growth in the height and well separated island of particles. It is evident that the aggregates and semi-connected network of np-Cu's observed in Fig. 3.19(a) completely coalesce during thermal treatment in inert condition.

The particle coalescence has been thermally activated by annealing in oxygen free environment. Particle agglomeration is activated by increased temperature, so the aggregates coalesce with each other to grow in size.

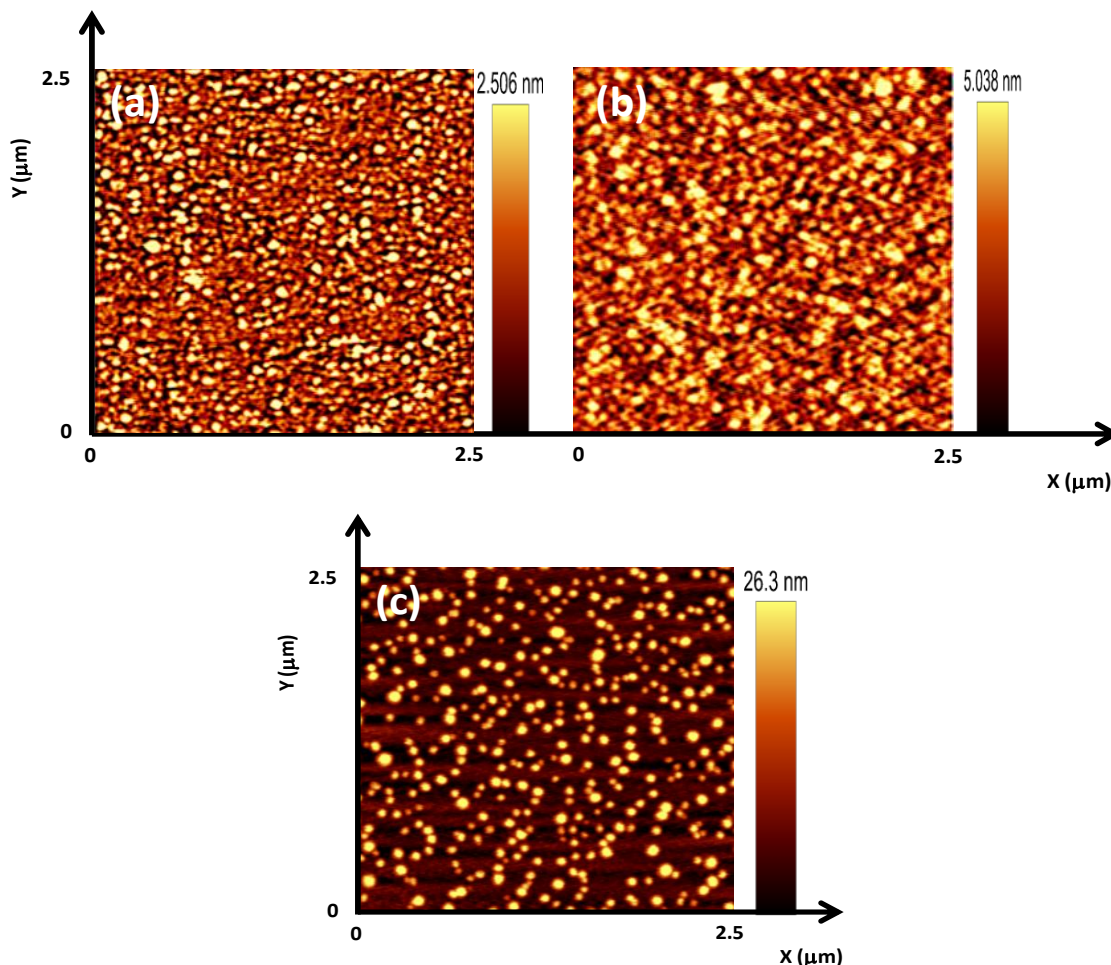


Fig. 3.19: AFM topographic images of (a) as-deposited, (b) air-annealed and (c) glove box annealed np-Cu's. Thermal annealing was carried out at 300°C for 1 hour in each case

In order to understand the predominant process leading to the formation of nanoparticle islands during thermal treatment, we carried out additional experiments by varying both the annealing time and the temperature. The sample used for this study was grown at the conditions shown in Table 3.5. Preliminary morphological study carried out on np-Cu's deposited with the perforated stage show that the sputtering rate in this case is relatively low. Unfortunately, the surface topography of these samples appears very flat, which implies that the deposited np-Cu's are mainly thin films. Thin films of metals can be used to study the effects of annealing

conditions on particle growth [13, 14]. In our case, the sample stage temperature rose dramatically from 28°C to 284°C during these depositions, an indication that sputtering was also taking place from the sample stage. The surface topography of the samples of this set annealed for 1 hour at different temperatures in the glove box is shown in Fig. 3.20, together with the topography of the as-deposited sample, showing a network of np-Cu's, much like a thin film.

Table 3.5: Sputtering parameters for samples to be annealed under different environment

Ar flow rate (SCCM)	RF power (W)	Sputtering time (min)	Substrate bias voltage (V)	Stage used (see Fig. 3.1)
25	60	5	-800	perforated

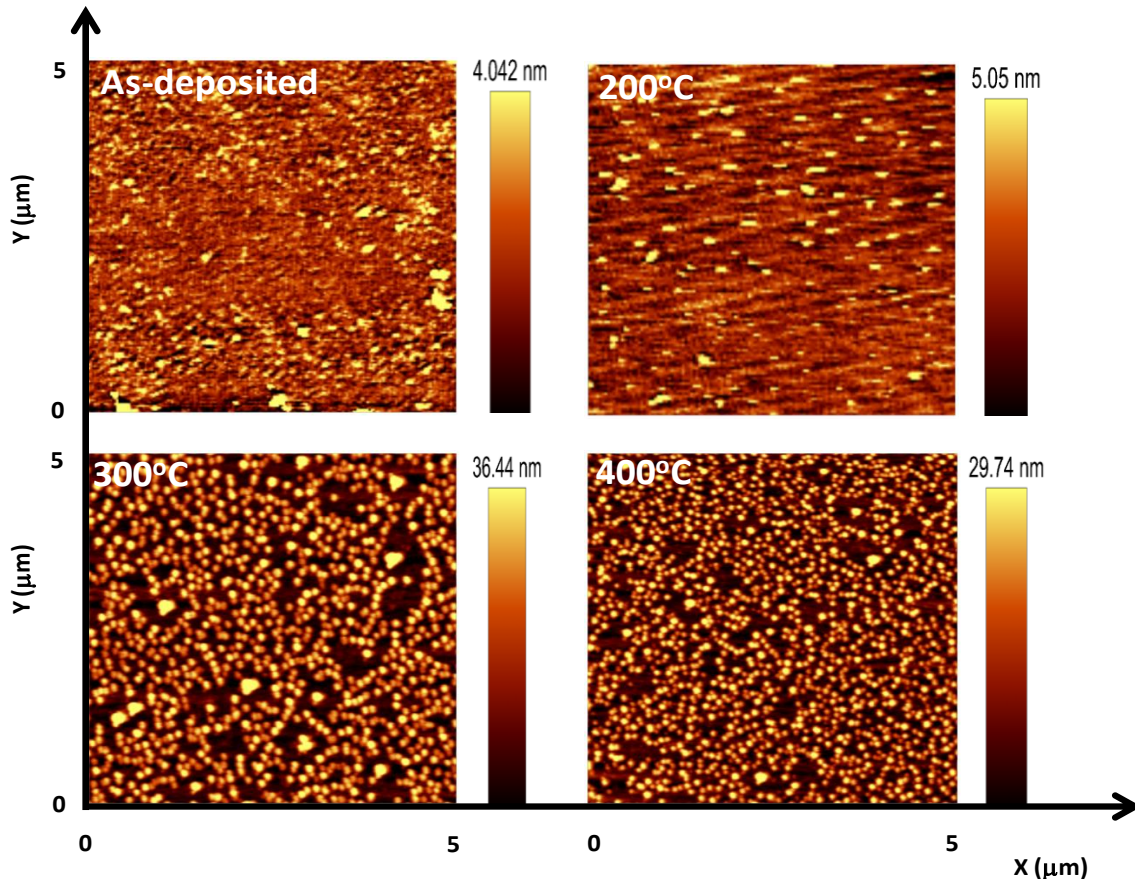


Fig.3.20: AFM topography of np-Cu's annealed in the glove box for 1 hour at different temperatures. The as-grown sample has been included for reference.

The topography of the sample annealed at 200°C did not show any improvements towards formation of isolated np-Cu's, an indication that thermal treatment carried out at this temperature is inadequate to induce the formation of individual particle. However, at 300°C and above, nucleation of copper island occurs, leading to the growth of nanoparticles in both in- and out-of-plane direction, with the subsequent formation of nano-sphere of copper as seen in Fig. 3.20. The AFM image of the sample annealed at 400°C shows an increase in the density of the nanoparticles and a decrease of the particle size from the sample annealed at 300°C. The result of the analysis of these two AFM images using Image J software is summarized in Table 3.6

Table 3.6: Average particles diameter and area fraction of np- Cu's annealed in the glove box at 300°C and 400°C for 1 hour

Annealing temperature (°C)	Average particle diameter (nm)	Area fraction	Plasmonic position (nm)
300	84	0.35	549
400	68	0.29	546

3.4.2 Parametric study as a function of treatment time

While keeping the treatment temperature constant, we also studied the condition of np-Cu's annealed at 300°C as a function of the treatment time.

From Fig. 3.21, we observe that more dispersed np-Cu's are obtained when the annealing time is increased from 30 minutes to 120 minutes. The dependence of particle size on the annealing time as obtained from Image J analysis is displayed in Fig. 3.22 for np-Cu's annealed at 300°C. The initial stage of thermal treatment is characterized by a decrease in particles size while the fraction of the substrate area covered by the particles gets increased. There is limited particles growth in the z-direction as observed in the AFM images.

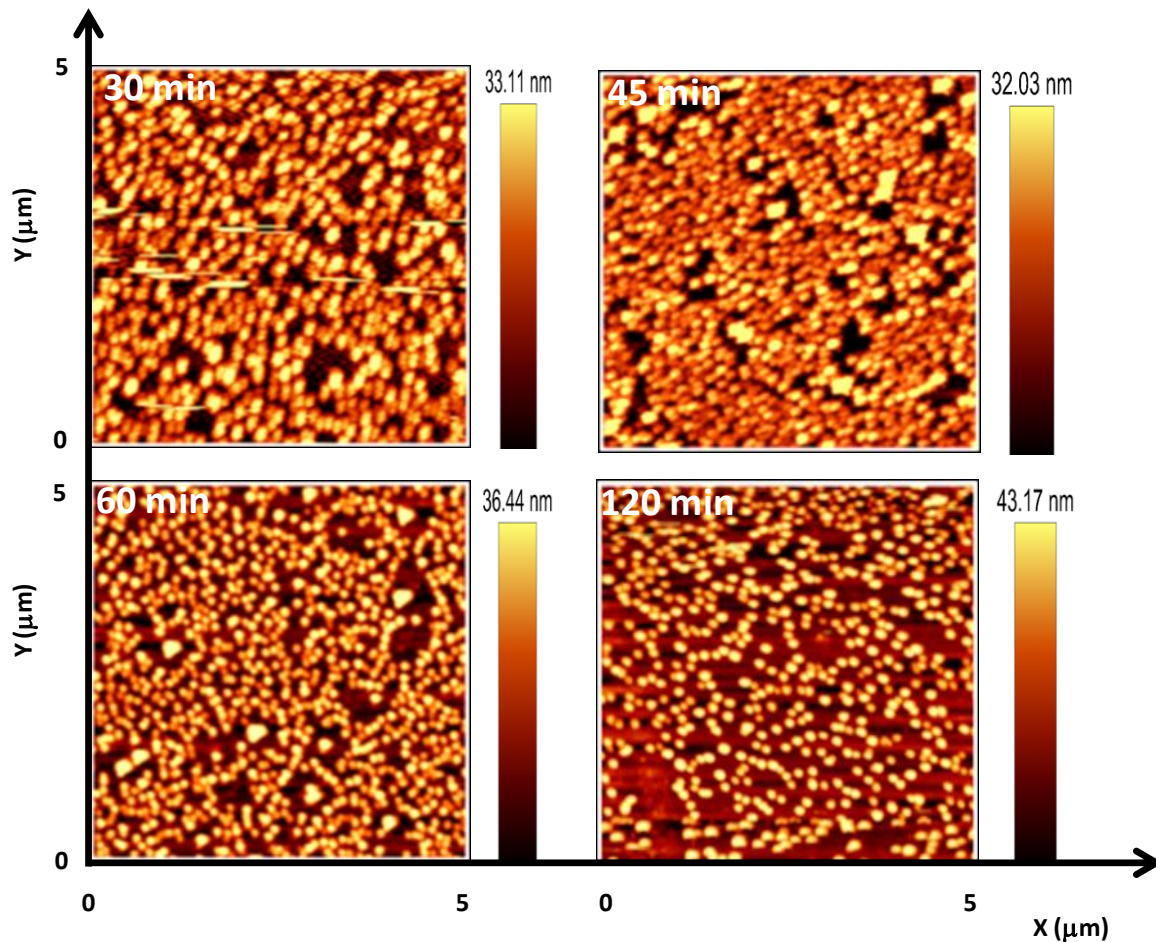


Fig. 3.21: AFM topographic images of np-Cu's annealed at 300°C in the glove box at different time intervals

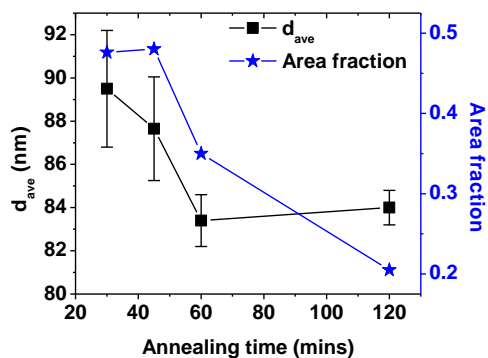


Fig. 3.22: Plot of average particle diameter and area fraction against the annealing time for np-Cu's annealed at 300°C

With increased annealing time, from 60 to 120 minutes, the size of the particles increases while the density of the nanoparticles decreases. These observations indicate that at the extended annealing time, particles coalescence is the most important mechanism of growth. This is consistent with the particles size distribution shown in Fig 3.23. The distribution has been fitted to a Gaussian function. As a conclusion, the thermal activation of particle coalescence leading to well dispersed np-Cu's is better realized within the range of temperature 300 – 400°C for annealing time, $t \geq 60$ minutes.

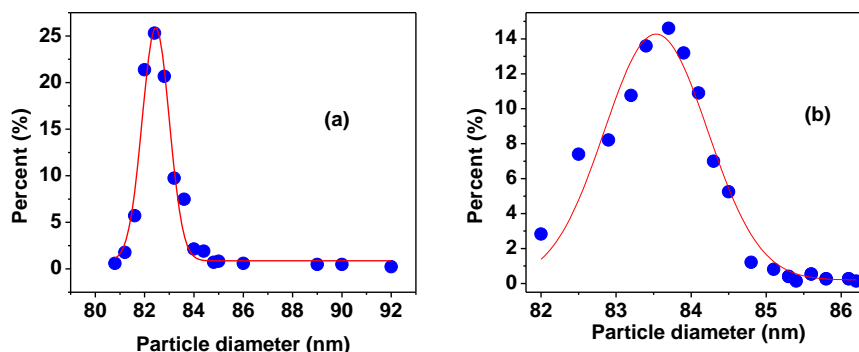


Fig.3.23: Particles size distribution of np-Cu's obtained from AFM topographic images displayed in Fig. 3.21 for the samples annealed in the glove box for (a) 60 mins and (b) 120 mins. The distribution has been fitted with a Gaussian function (solid curve).

3.4.3 Transmittance of thermally treated copper nanoparticles

In the following section, I will show the result of our optical transmittance measurement. Our experimental result reveals that besides a peak, it is possible to obtain also a dip in the transmittance spectra that is associated with plasmonic behavior [8, 15]. We present in Fig. 3.24, the optical transmission spectra of the sample annealed under different atmospheric conditions. We observe plasmonic behavior, corresponding to a peak and a dip in the transmittance spectra of the as-deposited and glove box annealed samples respectively. The observed maxima and minima are caused by resonant excitation of the particles plasmons. However, no plasmonic character can be associated with the sample annealed in air. In later section, I will show that scattered/transmitted light waves can be studied in details in the near field using the SNOM technique.

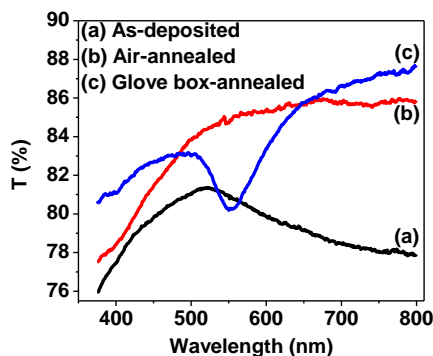


Fig.3.24: Variation of optical transmittance with wavelength for (a) as-deposited, (b) air-annealed and (c) glove box annealed np-Cu's. Thermal annealing was carried out at 300°C for 1 hour in each case

The wavelength dependence of the transmittance of samples of np-Cu's for different annealing temperatures and times is shown in Fig. 3.25. In optical transmission spectra, a dip (or peak in case of absorption spectra) situated at around 560 – 590 nm is associated with surface plasmon resonance absorption of np-Cu's [12, 16-21]. However, the position of the plasmon resonance can be blue or red shifted based on the particles size distribution [12]. Here, the positions of the plasmonic peak were blue shifted in all the annealed islands of np-Cu ensembles. In Fig. 3.25(a), no transmission dip can be associated with samples annealed at 200°C and the as-deposited. This is not surprising since the samples topography, as presented in Fig.3.20 shows mainly evidence of semi-continuous film. Analysis of np-Cu's obtained from the samples annealed at 300°C and 400°C shows that the full width at half maximum (FWHM) in the transmittance spectra decreased from 43.26 nm to 33.96 nm just as the average particle size decreased from 83.5 nm to 67.7 nm (see Table 3.5). The associated transmission dips occur at 550 nm and 546 nm for the np-Cu island annealed at 300°C and 400°C respectively. This corresponds to a blue shift in the surface plasmon resonance position of 4 nm.

It can be observed from Fig. 3.25(b) that the transmittance spectrum of np-Cu's depends on the annealing time. The transmittance decreases with the annealing time and the position of the dip shifts slightly. For relatively small annealing time, copper islands cover most of the substrate surface area and this result in broadening of the linewidth of the transmittance dip. By changing the annealing time, the position of the dip follows more closely the area fraction of the

islands of np-Cu's. This is summarized in Fig.3.26, where it is shown that both the full width at half maximum (FWHM) and the area fraction decrease with annealing time.

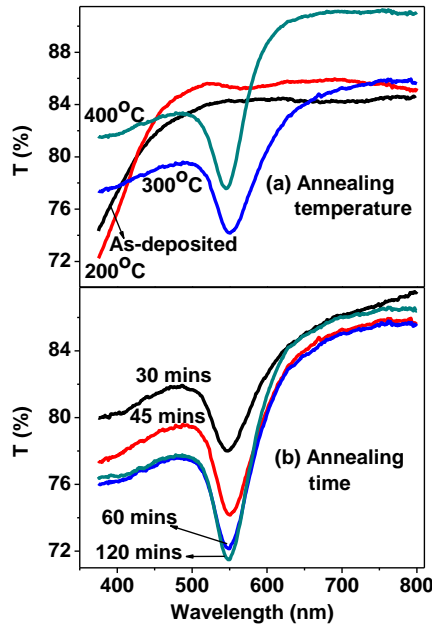


Fig.3.25: Plots of transmittance against wavelength for thermally treated np-Cu's under different conditions: (a) np-Cu's annealed at different temperatures and (b) np-Cu's annealed at different duration.

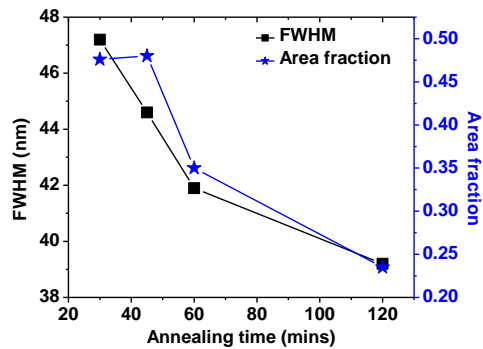


Fig. 3.26: Full linewidth at half maximum and the area fraction of island of np-Cu's vs. annealing time.

3.5 Properties of thermally treated copper nanoparticles grown at different RF power

In section 3.3.1, we showed that particle coalescence does not result in complete island formation in the case of as-deposited np-Cu's sputtered with different RF powers at relatively low argon flow rate. In order to initiate further nucleation sufficient for island formation, we annealed a set of five samples deposited with 25, 33, 55, 75, and 100W RF powers at 20 SCCM argon flow rate and for 3 mins. Thermal annealing was carried out in the glove box at 400°C for two hours. The topographic images of the set of five samples are shown in Fig. 3.27. The figure shows that samples deposited with lower RF power have better dispersed particles after thermal treatment. Both the particle size and the area of the substrate that is covered by the particles increases with RF power. Before and after the annealing operation, the sample deposited with 25 W of power appears plain to my visual inspection. However, the same sample turns out to be the most dispersed. Implying that thinner as-deposited np-Cu's is essentially important in order to achieve well-separated and small sized Cu nanoparticles. The average size of the particles as estimated from image J are 46, 68 and 77 nm for the samples deposited with 25, 33 and 55 W respectively. Fig.3.28 shows the dispersion of np-Cu's obtained from the sample deposited with 25 W of RF power. The figure shows that the particle dispersion follows a Gaussian distribution.

The optical transmittance of the samples deposited at different RF powers is shown in Fig. 3.29. We observe from this figure a broadening of the spectral line width as well as a shift in the transmittance minimum towards larger wavelength with increasing RF power. The variation of the plasmonic resonance (transmittance minimum) position and the FWHM with the area fraction of the substrate covered with np-Cu's is displayed in Fig. 3.30. The variation of the resonance position follows more closely the area fraction but the broadening of the transmittance spectra, which is shown as FWHM does not follow similar trend. Though, it is not feasible to determine accurately the particle size and dispersion from each of the AFM images, it can be observed that samples deposited with higher RF power exhibit higher particles variance and hence broadening of the transmittance spectra.

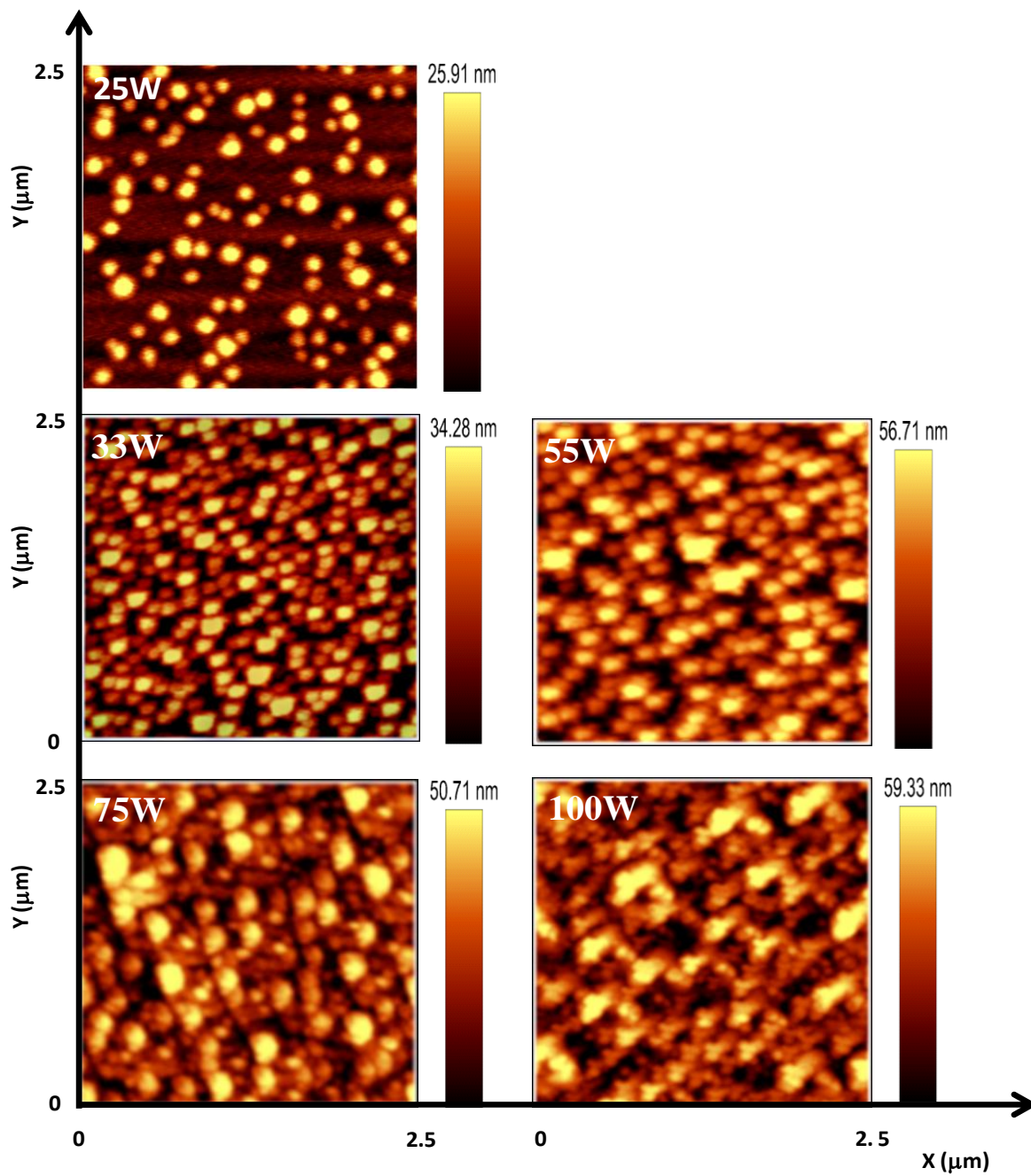


Fig. 3.27: AFM topographic images of thermally treated np-Cu's deposited with different RF powers.

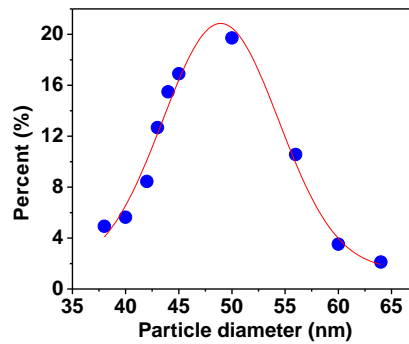


Fig.3.28: Particles size distribution of np-Cu’s obtained from AFM topographic images displayed in Fig. 3.27 for the sample sputtered with 25 W RF power and thermally treated in the glove box at 400°C for 2 hrs. The distribution has been fitted with a Gaussian function (solid curve).

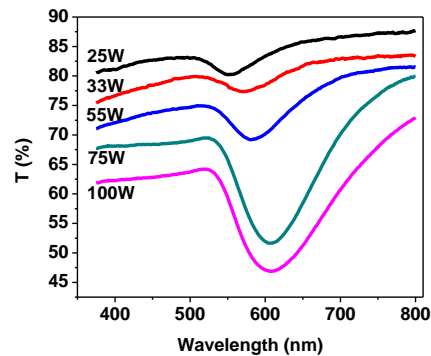


Fig. 3.29: Transmittance vs. wavelength of thermally treated np-Cu’s deposited with different RF powers.

We can conclude that lowering the sputtering rate by using a lower power during sputtering operation results in a thin copper layer that can be annealed to obtain small sized and well dispersed np-Cu’s. These isolated np-Cu’s exhibit a transmission minimum corresponding to a plasmon resonance frequency of 553 – 580 nm. This wavelength range is optimal for the application of these particles in plasmonic solar cell because it approximately correspond to the peak of the solar spectrum under AM 1.5 conditions [22].

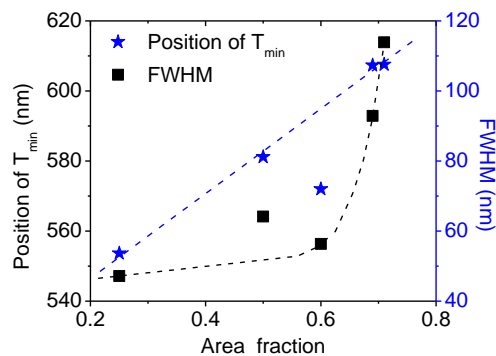


Fig.3.30: Plots of the plasmonic resonance peak (transmittance minimum) position and the FWHM of transmittance spectra against the area fraction for np-Cu's obtained from thermal treatment of samples deposited with different RF powers.

3.6. Conclusion

In this chapter, the influence of the deposition conditions (RF power, chamber pressure and substrate bias voltage) on the morphological and optical properties of np-Cu's has been explored in details. Better dispersed np-Cu's were obtained for deposition carried out under different conditions of chamber pressure with an average np-Cu diameter within 30 nm – 50 nm range. These np-Cu's exhibit enhancement of transmitted light in the spectral position corresponding to 548 – 580 nm. The results of the experiment showed that the combined effects of low RF power (25 W – 75 W), high chamber pressure (17 Pa – 23 Pa) and substrate DC bias voltage (300 V – 400 V) are required to grow dispersed np-Cu's. Under these conditions, copper nanoparticles grow by aggregation of initial island nuclei due to a reduction in sputtering rate.

Significantly, higher dispersed np-Cu's is obtained when a set of samples grown at 25 W and 33 W RF power is subjected to thermal treatment in oxygen-free glove box. Optical properties of np-Cu's show improvement in the visible region (535 – 580 nm) related to transmission enhancement in as-deposited samples and plasmonic enhancement in thermally treated ones.

3.7 References

- [1] C. Salzemann, I. Lisiecki, A. Brioude, J. Urban, and M. P. Pileni, *J. Phys. Chem. B*, **108**, 13242 (2004)
- [2] http://www.eng.utah.edu/~lzung/images/Lecture_10_AFM.pdf
- [3] <http://www.witec.de/>
- [4] <http://rsb.info.nih.gov/ij/>
- [5] V. Chawla, R. Jayaganthan and R. Chandra, *J. Mater. Sci. Technol.*, **26(8)**, 673 (2010)
- [6] T. Ghodselahi, M. A. Vesaghi, A. Shafiekhani, A. Baradaran, A. Karimi and Z. Mobini, *Surf. & Coatings Tech.* **202**, 2731 (2008)
- [7] J. Robertson, *Mater. Sci Eng.* **R37**, 129 (2002)
- [8] V. Halte and J. Y. Bigot, <http://www-ipcms.u-strasbg.fr/spip.php?rubrique311>
- [9] X. H. Yang, F. G. Zeng and X. J. Li, *Mat. Sci. in Semiconductor Proc.* (2012), <http://dx.doi.org/10.11016/l.mssp.2012.07.007>
- [10] O. A. Yeshchenko, I. M. Dmitruk, A. M. Dmytruk and A. A. Alexeenko, *Mat. Sci. & Eng. B* **137**, 247 (2007)
- [12] U. Pal, A. Bautista-Hernandez, L. R. Fernandez, J.C. Cheang-Wong, *J. of Non-Crystalline Solids* **275**, 65 (2000)
- [13] D. Manikandan, S. Mohan, P. Magudapathy, K.G.M. Nair, *Physica B* **325**, 86–91(2003)
- [14] M Shariati, M. Ghoranneviss, H. Hosseini, M. R. Hantehzadeh, *Surf. & Coat. Tech.* **201 (9-11)**, 5570 (2007)
- [15] E.D. Mozrzymas and P. Bieganski, *App. Oprics*, **32(13)**, 2345 (1993)
- [16] E. Anno, M. Tanimoto, T. Yamaguchi, *Phys. Rev. B*, **38**, 3521 (1988)
- [17] R. Bertonecello, F. Trivillin, E. Cattaruzza, P. Mazzoldi, G.W. Arnold, G. Battaglin, M. Catalano, *J. Appl. Phys.* **77**, 1294 (1995)
- [18] R.H. Magruder III, R.F. Haglund Jr., L. Yang, J. E. Witting, R. A. Zuhr, *J. Appl. Phys.* **76**, 708 (1994)

- [19] K. Fukumi, A. Chayahara, K Kadono, T. Sakaguchi, Y. Horino, M. Miya, K Fujii, J. Hayakawa, M. Satou. *J. Appl. Phys.* **75**, 3075 (1994)
- [20] R.A. Wood, P.D. Townsend, N.D. Skelland, D.E. Hole, J. Barton, C.N. Afonso, *J. Appl. Phys.* **74**, 5754 (1993)
- [21] P.K. Khanna, P. More, J. Jawalker, Y. Patil and N. K. Rao, *J. Nanopart Res* **11**, 793 (2009)
- [22] Y. Afsar, J. Sarik, M. Gorlatova, G. Zussman, and I. Kymissis, <http://enhants.ee.columbia.edu/images/papers/EvaluatingYafsarIPSC2012.pdf>

Chapter 4

4 Scanning near field optical studies of copper nanoparticles

4.1 Scanning near field optical microscopy (SNOM)

Resolution in conventional optical microscopes is diffraction-limited. Thus, these instruments are not suited for studying individual nanoparticles. This limit can be quantified by considering the resolving power of an optical instrument, which is given by the Rayleigh criterion [1]

$$R \approx \frac{\lambda}{2.NA} \quad (4.1)$$

where NA is the numerical aperture of the objective used for collecting the light beam. Therefore, for visible light ($\lambda = 400 - 700$ nm) R is determined by the numerical aperture (that, for construction reasons, is generally not much larger than 1), but is rarely better than 200 nm.

Scanning near-field optical microscopes (SNOM) circumvent the intrinsic limitations of the resolving power of conventional optical microscopes and, therefore, are better suited for high-resolution studies of individual np-Cu's. In SNOM, subwavelength resolution is achieved by using an evanescent wave, generated in the proximity of nanoholes or nanoparticles, as an optical probe to scan the surface of a sample. An example of evanescent field is the electric field exponentially decaying in a dielectric medium interfaced to a metallic thin film or a metallic nanoparticle, as discussed in Sect. 1.1.2 and 1.1.3, respectively.

Fig. 4.1 (adapted from ref. 1) depicts the non-propagating and propagating electric field components generated as a consequence of the interaction of an incident plane wave with a nanoparticle of diameter d . In Sect. 1.1.3, we have discussed that the electric field scattered at a distances r from a particle of finite diameter is multipolar in nature, with only the dipolar component that is not vanishing at sufficiently large distances and results in spherical waves that are isotropically propagating in any direction of the free space. Such a component of the electric field is associated to the smallest value of n (i.e. $n = 1$) in the summation given by eq. (1.20) and corresponds to the so called 'far field' that is generally observed by optical instruments of limited resolution. A number of higher-order terms of eq. (1.20) typically at small values of n , also correspond to propagating components of the electric field, but they are highly anisotropic in nature and their intensity strongly depends on the angle with respect to the direction of

propagation of incident light, as demonstrated in ref. [2]. These components are typically responsible for light diffracted by a particle (or hole) at $d \sim \lambda$. At even higher values of n in eq. (1.20), stationary waves strongly localized in the vicinity of a nanoparticle (or nanohole) will appear, if $d \ll \lambda$ [2]. These evanescent wave components, that form the so called ‘near field’, exponentially decay away from the surface of the nanoparticle (or nanohole) and are uniquely suited for probing objects of nanometric size located near the scattering nanoparticle (or nanohole), because the strong localization of these modes warrants ultra-high optical resolution.

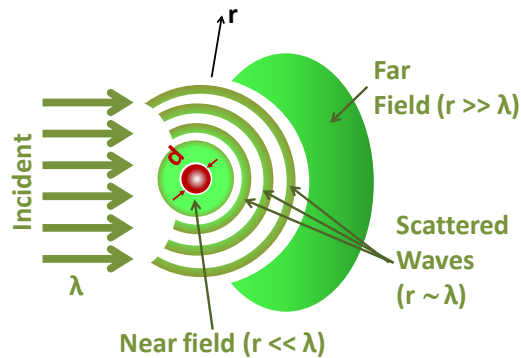


Fig. 4.1: Light scattered from a particle as a source of near field. The electric field close to the particle is formed by evanescent (near field) and scattered propagating components.

Far from the particle ($r \gg \lambda$) the field is radiating by spherical waves.

Near-field optical microscopes using nanoholes for generating, or collecting, the evanescent field are called aperture-type SNOMs, while near-field optical microscopes using nanoparticles for generating, or collecting, the evanescent field are denominated apertureless-type SNOMs. An advantage of modern near-field microscopes, which brought this nano-optical technique to commercial maturity [3] is the possibility to integrate them into atomic force microscopes (Sect 3.2). For apertureless-type SNOMs, a metal nanoparticle is attached at the bottom of an AFM tip while, for aperture-type SNOMs, a nano-hole is drilled through the AFM tip using a focused ion beam (FIB) such as the one available at the Western Nanofabrication Facility. In this way, SNOM images can be recorded by moving the nanoparticle (or nanohole) relative to the sample using a computer-controlled AFM piezo-scanner. The nano-optical image of the sample is then formed by assigning the measured optical intensity to the corresponding scanning position [4].

4.2 The Witec Alfa 300S SNOM system

Figure 4.2 is a schematic of the aperture-type, AFM-integrated, SNOM instrument (Witec Alfa 300S) that has been used for our near field optical study of np-Cu's. With this instrument, light from a 532 nm green laser operated up to 50 mW (Excelsior, Spectra Physics Inc., serial no. 10398) is directed, by a system of optical fibers, into a high-resolution confocal optical microscope that focuses the laser light inside the nanohole ($d \approx 80$ nm) located at the end of an AFM hollow tip. The sample is positioned on a $100 \times 100 \mu\text{m}$ piezo-scanner that has a maximum excursion of $10 \mu\text{m}$ in the z-direction. All three AFM scanning operation modes (contact, non-contact and tapping mode) are possible for recording SNOM images and, simultaneously, AFM topographic images of a sample. In addition, the mechanical arm on which the confocal microscope is mounted can also be moved in z-direction for optimizing the focal plane at the level of the AFM tip hole. Below the sample stage, an inverted microscope is used to collect the light transmitted through the sample, which is subsequently launched into an optical fiber that is connected to a photomultiplier tube (U-68000, Hamamatsu) operating in photon-counting mode.

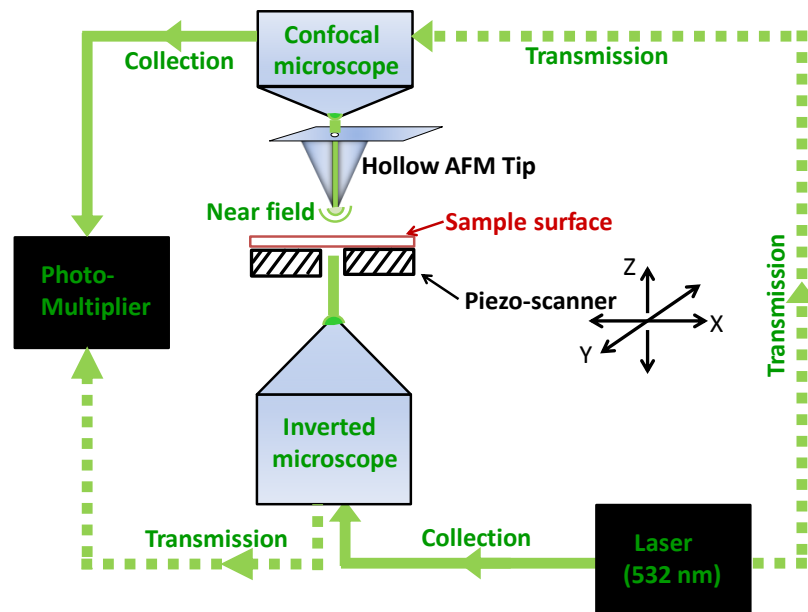


Fig. 4.2: Schematic of the operation configurations of the Witec Alfa 300S system that was used for the SNOM study of np-Cu's: transmission mode and collection mode.

In addition to the operation mode described above, that is known as ‘transmission mode’ and is sketched in Fig. 4.2 with dotted lines, the Witec Alfa 300S can record SNOM images in another configuration, known as ‘collection mode’, that differs in the way the sample is illuminated and the scattered light is collected. In collection mode (also known as back-illumination mode) the sample is back-illuminated in the far-field, by directing the laser light into the inverted microscope, and the optical response of the sample is collected by the nanohole in the AFM cantilever. Specific tests can be performed for ensuring that subwavelength objects can be resolved in this configuration [3, 5]. If the hollow tip is sufficiently close to the sample surface, only the near-field optical response from the sample surface will be collected. However, if the hollow tip is lifted up at a controlled distance r from a nanoparticle that is located at the sample surface, all of the other normal modes shown in Fig. 4.1 (and representing, via eq. (1.2), the n components of the optical response of a nanoparticle) can be detected.

Therefore, in SNOM collection mode operation, the sample surface can be scanned along the (x, y) plane at $z = 0$, or in the (x, z) direction at $y = \text{constant}$, in order to obtain relevant information about the amount of light scattered by the particle at a distance $z = r$ from its surface, as demonstrated in Fig. 4.3. With this three-dimensional optical imaging procedure, specifically designed for this thesis work, the electromagnetic field around the particle can be entirely reconstructed.

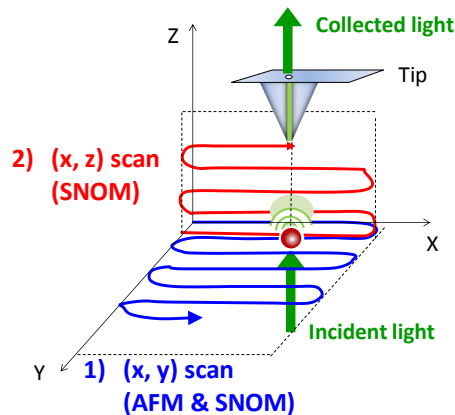


Fig. 4.3: Schematic diagram of the SNOM configuration during measurements of nanoparticle topography and light scattering in the near field. Collection-mode and topography images are obtained from an (x, y) AFM/SNOM scan at $z = 0$ while an (x, z) SNOM cross section scan at $y = \text{const.}$ has been used to gain insight on light scattering processes at different heights (determined by the piezo-scanner) from the sample surface.

Ultimately, SNOM is always about the electromagnetic interaction of two distinct nano-objects, for which the principle of linear superposition can be invoked: a ‘probe’ nano-object (that, in our case, is the nano-hole at the end of the tip) and a ‘sample’ nano-object (that, in our case, is a np-Cu in our sample). For the np-Cu that are the subject of the present study, collection mode SNOM analysis is carried out first to obtain the (x, y) nano-optical and topographic (contact-mode AFM) images of our sample, which are recorded simultaneously. We then choose a line at $y = \text{const.}$ from the (x, y) images and change the distance z from the tip to the sample surface. This can be done reproducibly because the piezo-scanner stage on which the sample is mounted allows to control the sample–tip distance with a ± 1 nm reproducibility. Before each (x, z) scan at $y = \text{constant}$ (see Fig. 4.3), the topographic and optical images of the sample were determined using $5 \times 5 \mu\text{m}$, contact mode scan in which the AFM and SNOM images are recorded at the sample surface.

4.3 Role of (X, Z) SNOM images in designing np-Cu for plasmonic solar cell applications

Thin film solar cells are made of doped semiconductors forming a p-n junction. In this architecture, (typical of a number of photovoltaic devices including organic and amorphous solar cells) the p-n junction where photocurrent is generated is sandwiched between two electrodes that help to transport the carriers to the external load (Fig.4.4). Through thinning down the active layer, the internal charge separation may be enhanced but not without compromising the amount of light that is absorbed inside the active layer. One method which has been explored for the development of thin film solar cells with improved performance is based on the incorporation of nanoparticles in the active layer of the so-called plasmonic solar cells [6]. With this method, light is scattered into the active layer by using nanoparticles excited at their surface plasmon resonances, thereby allowing light to be absorbed more directly without necessarily compromising the thickness of the active layer.

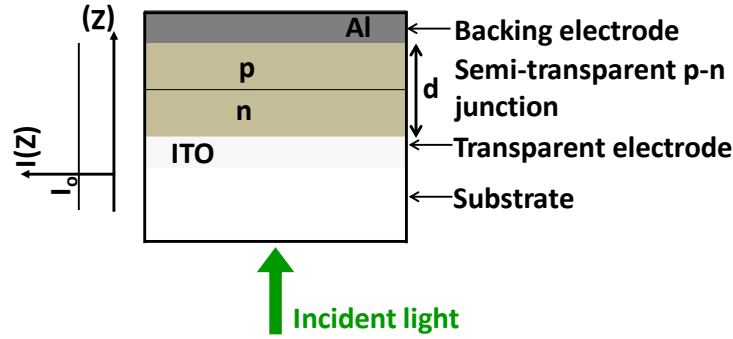


Fig. 4.4: Thin film solar cell comprising semi-transparent p-n junction sandwiched between two electrodes. $I(z) - z$ graph on the left shows the variation of intensity of the incident light over the entire p-n junction that serves as the active layer of the cell.

Fig. 4.5 shows a common design of plasmonic solar cell in which metal nanoparticles are deposited on the top of ITO electrode beneath the active layer of the cell. When light is incident on these nanoparticles at their surface plasmon resonances the dominant process induced by the nanoparticles is strong forward scattering of the incident radiation that results in three regions of scattered fields as previously mentioned.

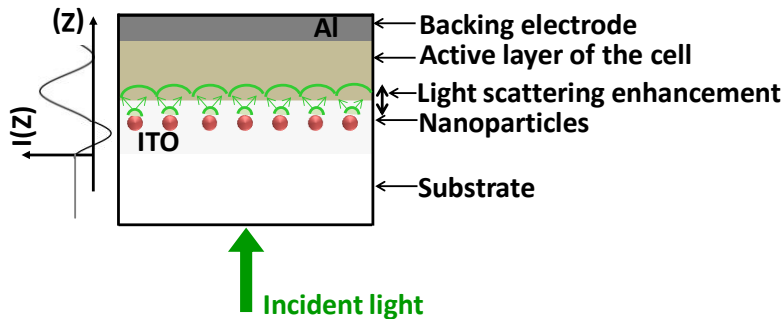


Fig. 4.5: Thin film plasmonic solar cell showing region of light scattering enhancement using metal nanoparticles. $I(z) - z$ curve on the left represents the variation of the scattered wave amplitude due to the embedded np. Amplitude of the scattered wave is enhanced at specific position from np surface.

Close to a nanoparticle, the scattered light is mainly evanescent in nature, which transfers non-propagating field in the near field into scattered waves at distances near the surface plasmon wavelength ($r \sim \lambda$). Hence, the forward scattering increases the electromagnetic field intensity at a considerable distance above the particles. This effect can increase the electron-hole pair

generation rate in the cell when the active layer is placed in the region of maximum scattered light intensity. Therefore, it is extremely important to determine the positions of this scattered light intensity in order to maximize the benefit of light scattering enhancement from the nanoparticles. It is within the above consideration that this study is important.

Our SNOM (x, z) scan are very useful to predict the amount of light that is scattered in waves at a distance, z from a np-Cu and by extension, which specific sets of the nanoparticles we have grown can be useful to convey light inside the active layer of a thin film solar cell. We have specifically chosen to perform our SNOM measurements at 532 nm wavelength, approximately corresponding to the maximum of the AM 1.5 solar spectrum [7], at which commercial solar cells are generally optimized, in order to make our results on the characterization of np-Cu's meaningful for solar applications.

4.4 Results and Discussion

The scattering effect associated with our np-Cu's was studied using SNOM measurement on a range of samples deposited at different chamber pressures. Deposition at different chamber pressure was previously shown to alter the area fraction as well as the np-Cu size. The (x, z) scan was employed to determine the positions of scattered waves as a series of bright regions atop the np-Cu surface. The bright regions are mapped on x - y plane along z -direction while the scattered wave intensity corresponding to the bright regions is plotted as a function of the distance from the sample surface, z .

Figs. 4.6 and 4.7 show the results from the SNOM measurements carried out on np-Cu's deposited at lower chamber pressures of 9 and 12 Pa respectively. It can be observed from these two figures that the scattered wave increases in intensity as the distance between the np-Cu scattering centre and the tip widens. The scattered wave closest to the sample surface is low in intensity compared to what can be observed at further distances from np-Cu surface. However, for the samples deposited at relatively higher pressures of 17, 21 and 23 Pa shown respectively in Figs. 4.8, 4.9 and 4.10, the interaction of light with the particles result in scattered waves that decreases in intensity from the sample surface. Contrary to what was observed from Figs. 4.6 and 4.7, these SNOM (x, z) measurements show that the intensity of the scattered wave has a maximum at position closest to the sample surface. The peak position of the scattered waves

closest to the np-Cu surface for all five samples has been plotted and is shown in Fig. 4.11. The error bars in the plot has been obtained from the standard deviation of 6 different values extracted from each of the (x, z) SNOM maps.

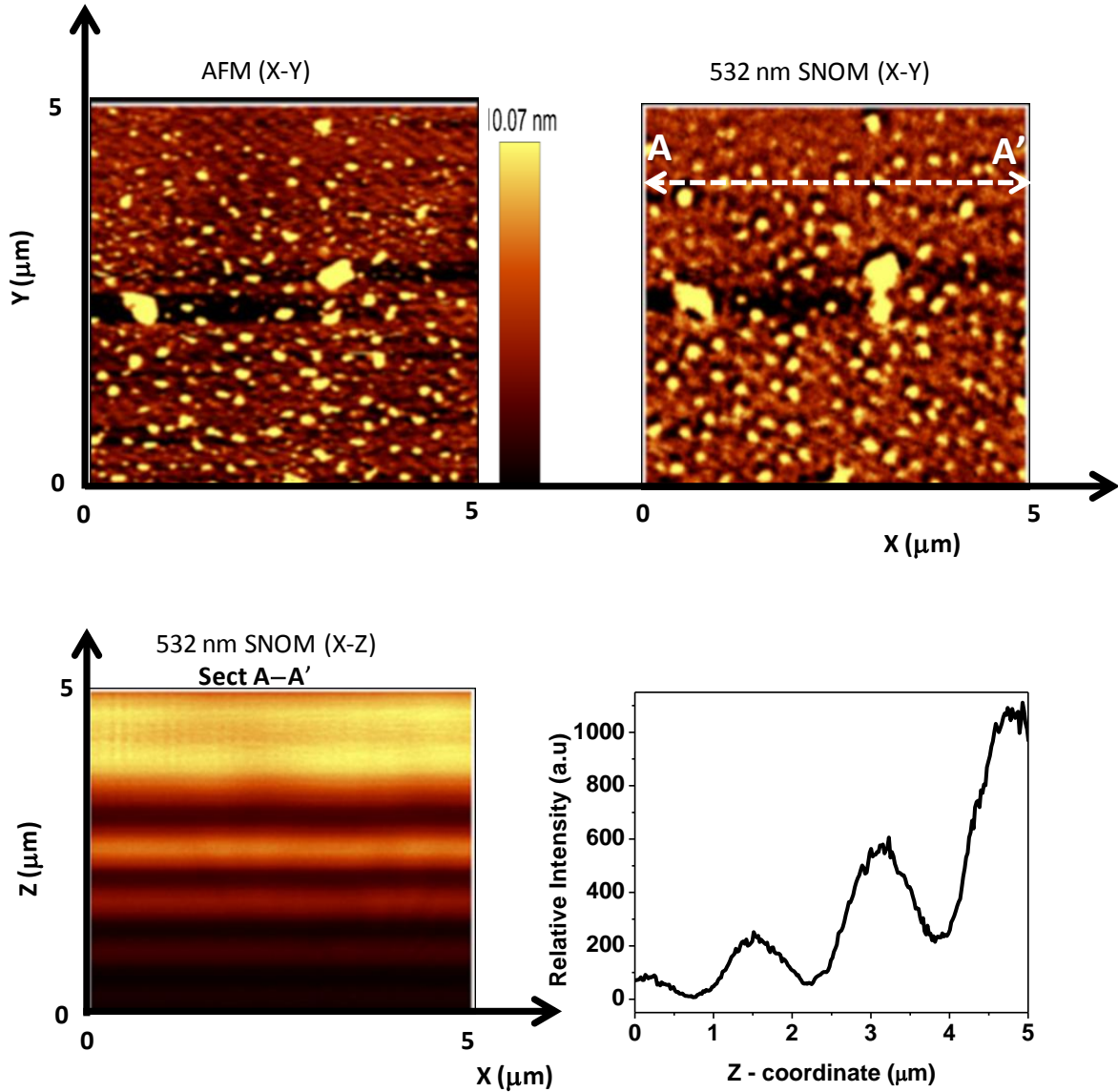


Fig. 4.6: Topographic (top left) and optical (top right) images obtained from SNOM operation for semi-continuous np-Cu's sputtered at chamber pressure of 9 Pa. Also displayed are the x – z intensity mapping (bottom left) and the intensity plot (bottom right) showing the positions of the scattered wave.

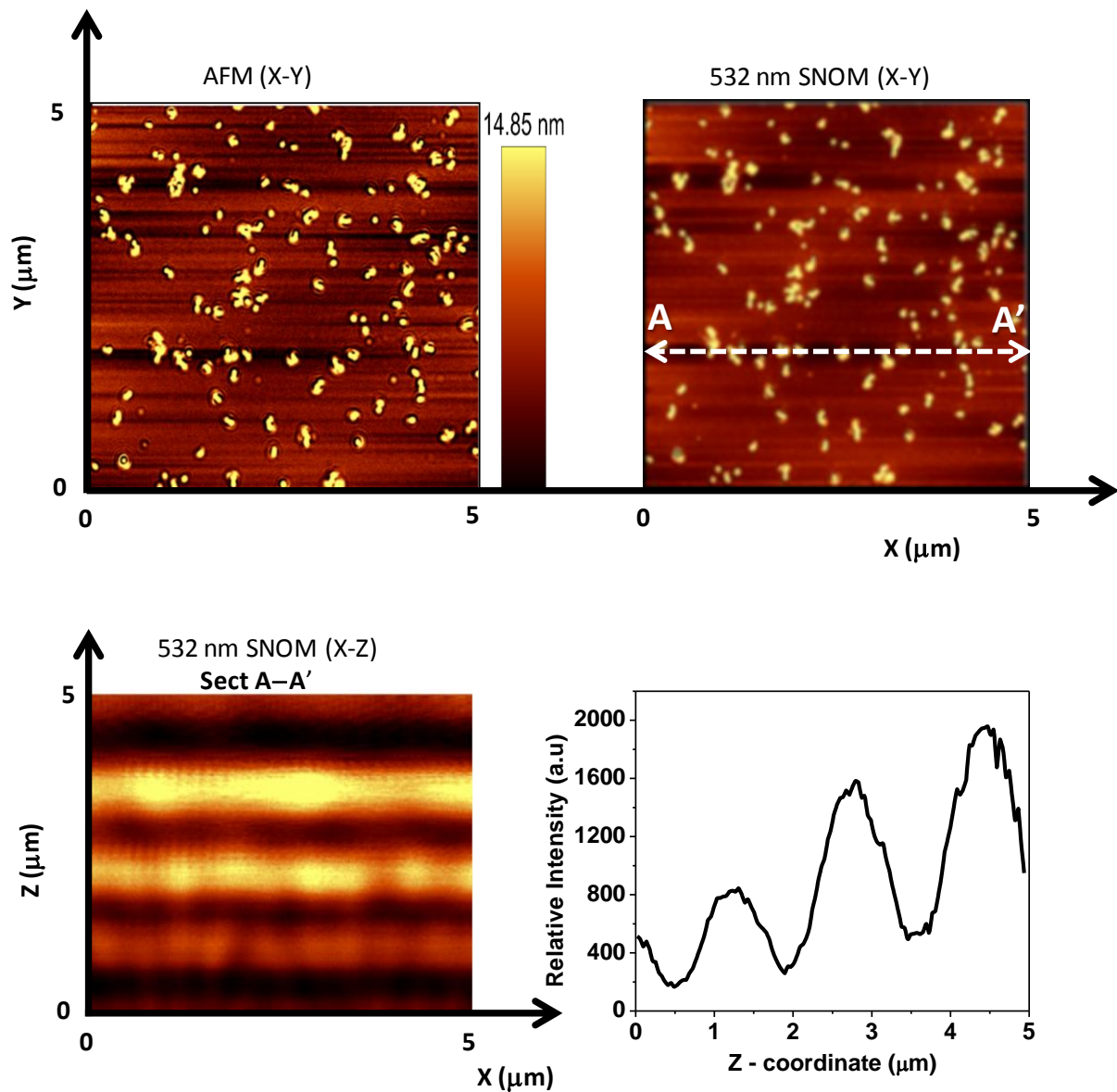


Fig. 4.7: Topographic (top left) and optical (top right) images obtained from SNOM measurement on np-Cu's sputtered at chamber pressure of 12 Pa. Also displayed are the x – z intensity mapping (bottom left) and the intensity plot (bottom right) showing the positions of the scattered wave.

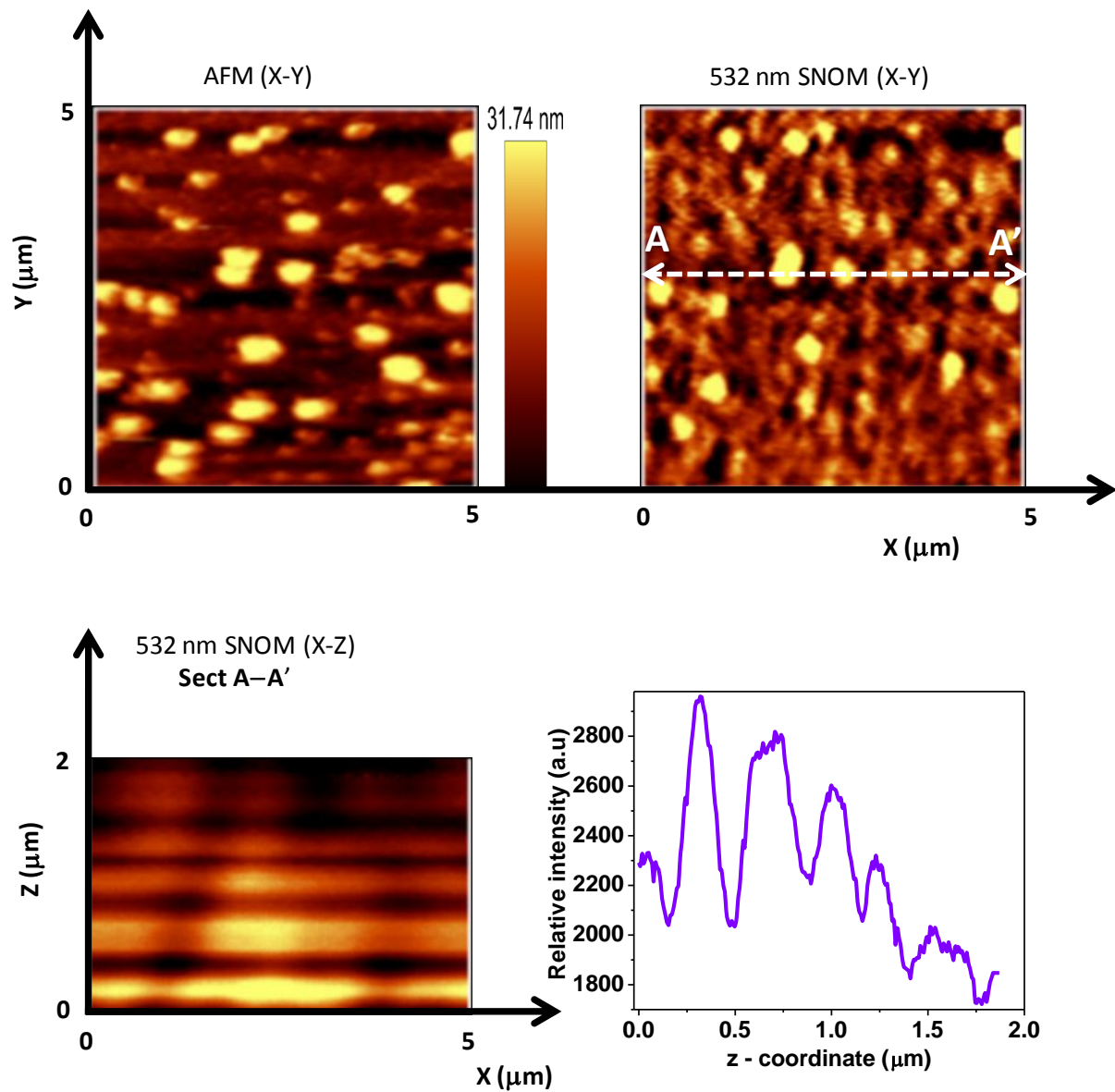


Fig. 4.8: Topographic (top left) and optical (top right) images obtained from SNOM measurement for semi-continuous np-Cu's sputtered at chamber pressure of 17 Pa. Also displayed are the x – z intensity mapping (bottom left) and the intensity plot (bottom right) showing the positions of the scattered wave.

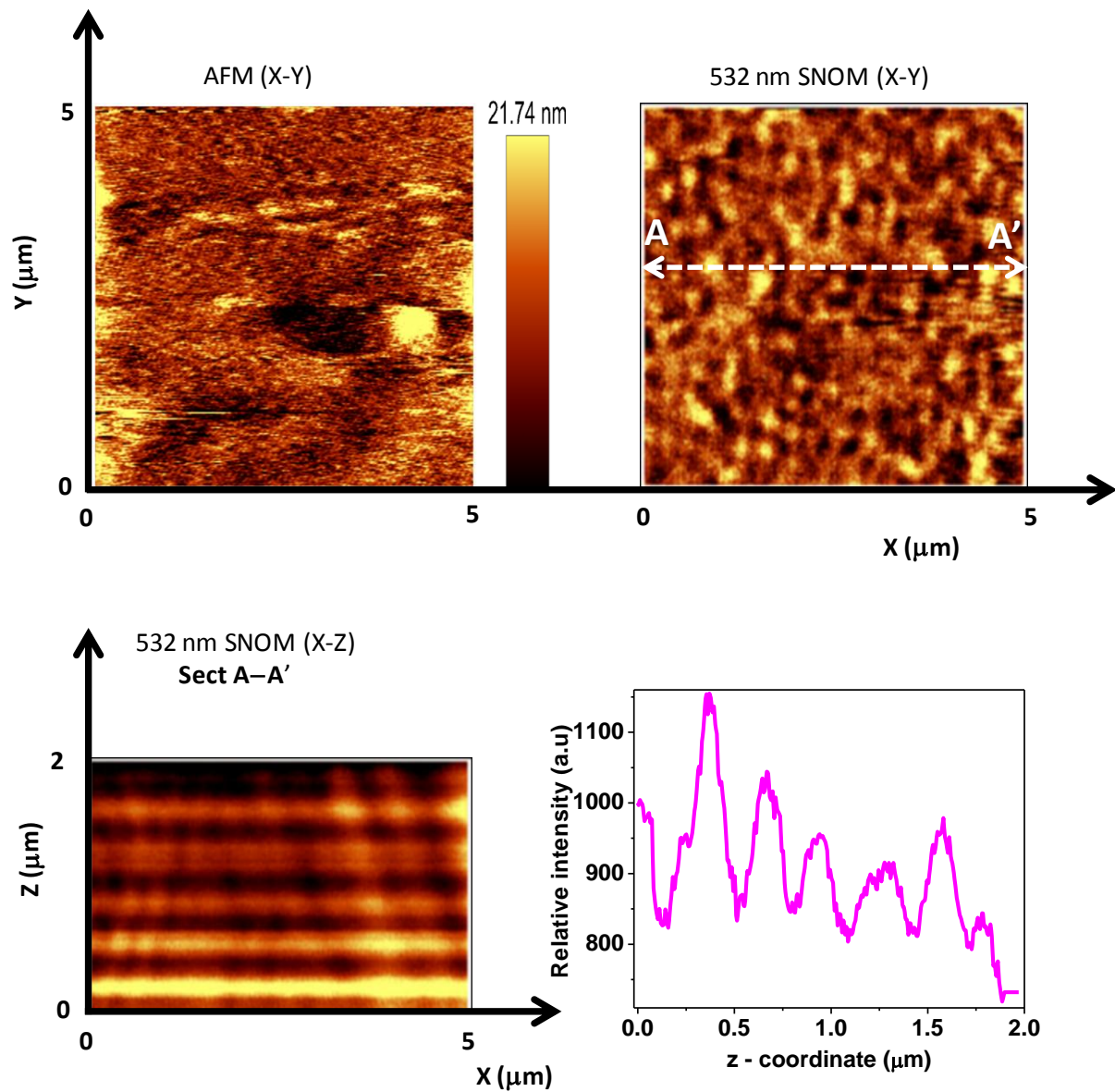


Fig. 4.9: Topographic (top left) and optical (top right) images obtained from SNOM measurement for semi-continuous np-Cu's sputtered at chamber pressure of 21 Pa. Also displayed are the x – z intensity mapping (bottom left) and the intensity plot (bottom right) showing the positions of the scattered wave.

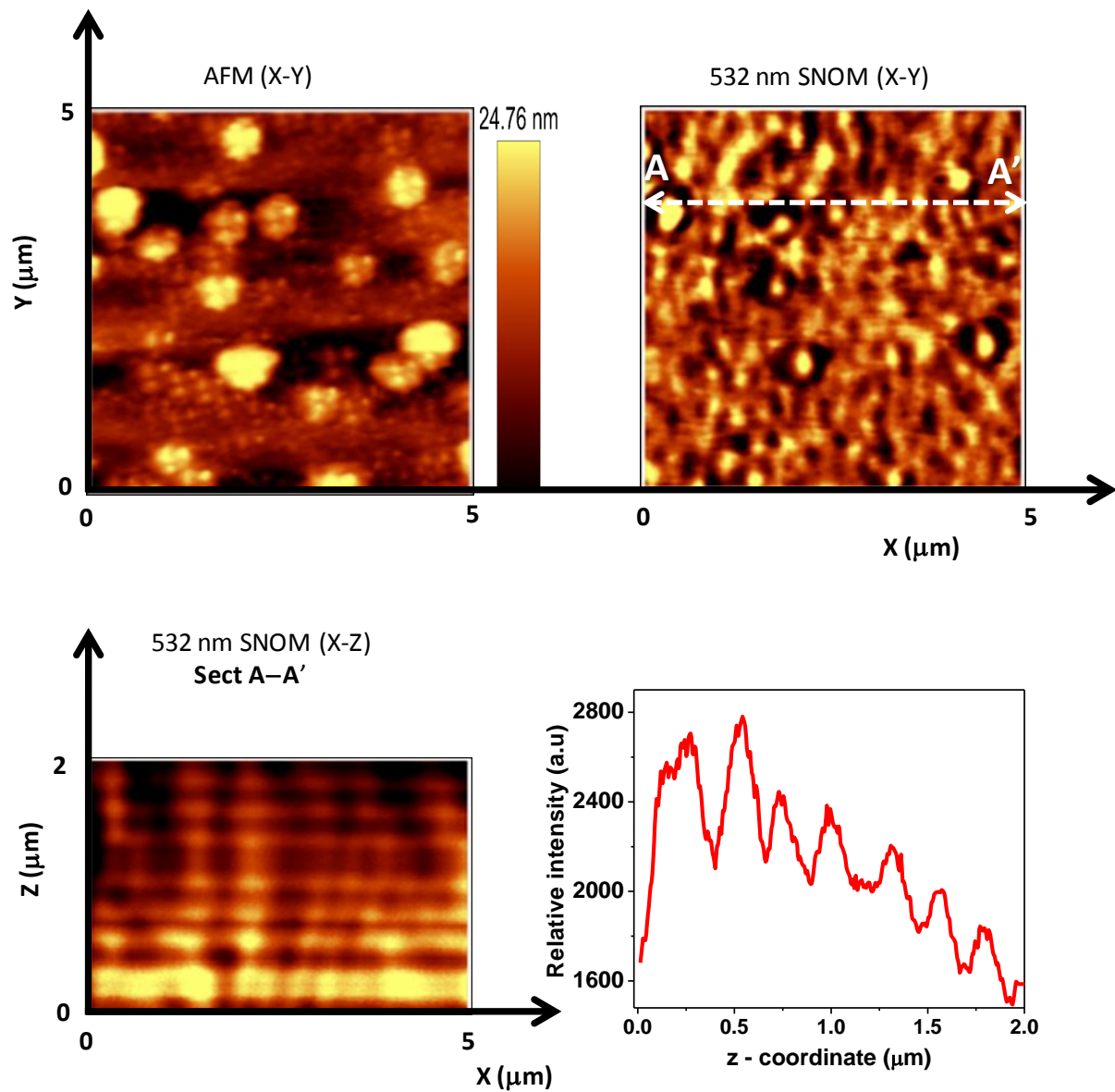


Fig. 4.10: Topographic (top left) and optical (top right) images obtained from SNOM measurement for semi-continuous np-Cu's sputtered at chamber pressure of 23 Pa. Also displayed are the x – z intensity mapping (bottom left) and the intensity plot (bottom right) showing the positions of the scattered wave.

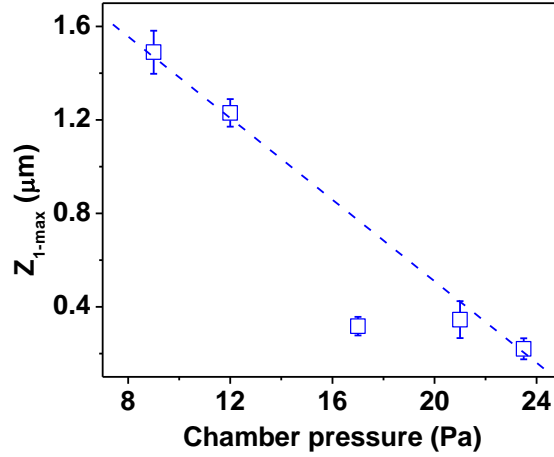


Fig. 4.11: Variation of scattered wave peak position with the deposition chamber pressure. Z_{1-max} represents the first significant peak intensity position of the scattered wave obtained from (x, z) SNOM map. The error bar corresponds to the standard deviation of 6 different intensity plots obtained from SNOM map.

As we observe from Fig. 4.11, the scattered wave from np-Cu's deposited at high chamber pressure is more closely coupled to the np surface compared to their counterpart obtained from RF sputtering carried out at lower chamber pressure. For instance, np-Cu's deposited at 23 Pa chamber pressure shows scattered wave peaks at 220 and 540 ± 50 nm as against the observed peak position at 1490 ± 100 nm for the particles obtained at 9 Pa chamber pressure. This observation can be attributed to the dependence of nanoparticles cross-section for optical absorption (Q_{abs}) and scattering (Q_{sca}) on the particle size. We have previously demonstrated in chapter 3 that increasing the chamber pressure results in particles with larger size but with reduced area fraction. Hence, for larger particles, $Q_{sca} \gg Q_{abs}$ since Q_{sca} is proportional to the square of the nanoparticle volume (see chapter 1) and the dominant process induced by np-Cu's is strong forward scattering of incident plane waves at different positions from the np surface. Unfortunately, the forward scattering is observed at positions that are considerably inadequate for overall transmission of electromagnetic energy into the active layer of a photoactive device, for instance plasmonic solar cell, where the particles have potential application. Therefore, to use these np-Cu's to increase performance in a plasmonic solar cell it is most desirable to have the active layer of the cell formed at the observed peak intensity positions for efficient coupling of the scattered light into the active layer of the cell. The above

consideration means that it would be beneficial to employ dielectric material for which the desired scattering effects are still present but for which surface plasmon resonances do not occur. We explored the prospect of this concept, depositing SiO₂ thin film on our np-Cu's, to be adapted as a spacer between the np's and the active layer of a plasmonic solar cell.

4.5 Properties of np-Cu/SiO₂ nanocomposites

We obtained SiO₂ by RF sputtering of a glass target. Different thicknesses of SiO₂ can be deposited atop np-Cu's surface by varying the deposition time. The deposited np-Cu/SiO₂ composites were characterized using similar procedure as describe in the previous section.

The result from the SNOM measurement is shown in Fig. 4.12. From the intensity map (*x-z* plot) of Fig. 4.12, we observed initial broadening of the scattered wave in the vicinity of np-Cu/SiO₂ composite that extend up to 550 nm from the composite surface. The first intensity peak from reference bare np-Cu's was observed at 250 nm from the sample surface, similar to what has previously been observed. Thus, we associate the observed broadening of the scattered wave in the vicinity of the composite structure with coupling of the plane wave, incident normal to the composite surface into lateral propagation paths (parallel to the SiO₂ surface) which results from introduction of a lateral wave vector component [8] in the scattered wave. This concept has been studied using metallic nanoparticles deposited on a low-surface-energy dielectric material to enhance photocurrent response in silicon-on-insulator photodetectors [9]. Superposition of the lateral and transverse components of the wave vector can lead to increased intensity of the scattered light wave.

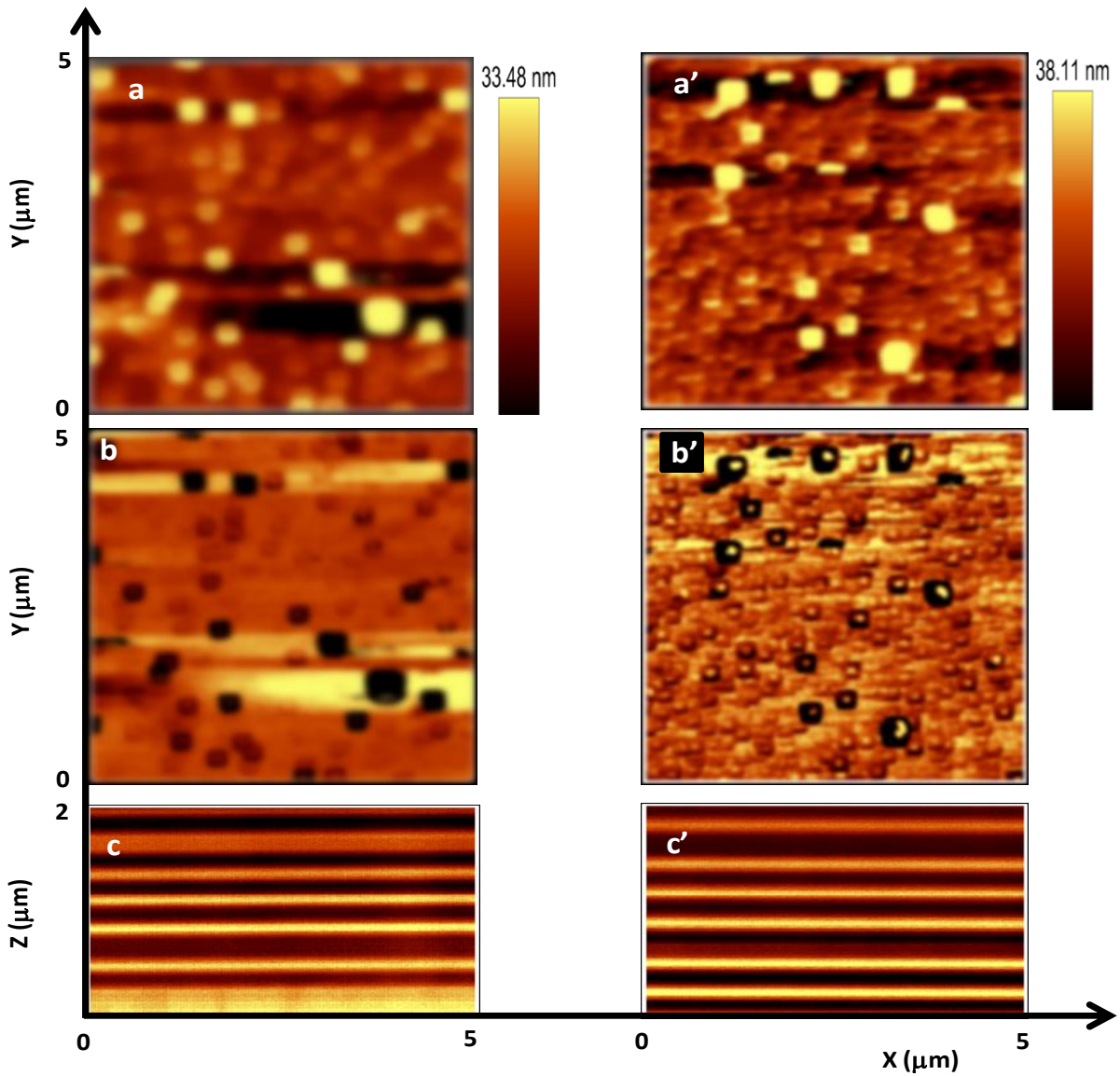


Fig. 4.12: x-y topographic images (top), x-y optical images (middle) and x-z intensity map (bottom) of np-Cu's measured by SNOM technique. The images on the right were obtained from reference bare np-Cu sample on glass substrate while the images on the left are for the np-Cu/SiO₂ composite.

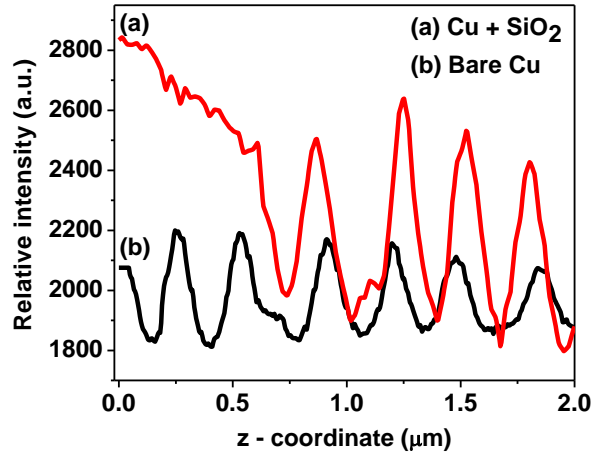


Fig. 4.13: Plot of the scattered wave intensity as a function of the distance from the sample surface (out of plane) for bare np-Cu's and np-Cu/SiO₂ composite.

Fig. 4.13 shows the intensity plot for the two samples as extracted from the (x-z) SNOM map. It is seen that, besides showing an extended scattered wave, the composite structure also exhibit high amplitude of the scattered light intensity along the entire 2 μ m-distance scanned compared to what can be observed from the reference sample. This effect has been extended to far field, observed from the UV-VIS measurement carried out on reference bare np-Cu's and np-Cu/SiO₂ composites. As is evident from Fig. 4.14, the incorporation of SiO₂ atop np-Cu does indeed result in a substantially higher value of the transmitted light, even in the far field. For the composite formed after 6 hours sputtering of SiO₂, we observe as well a dip at around 457 nm in the transmission spectra. The lower value of the transmitted light and the appearance of dip in the UV-VIS of this sample compared to the results of other composites suggest that at reasonably large thickness of SiO₂ we can associate with the experimentally observed spectra an inter-band transition at higher photon energy.

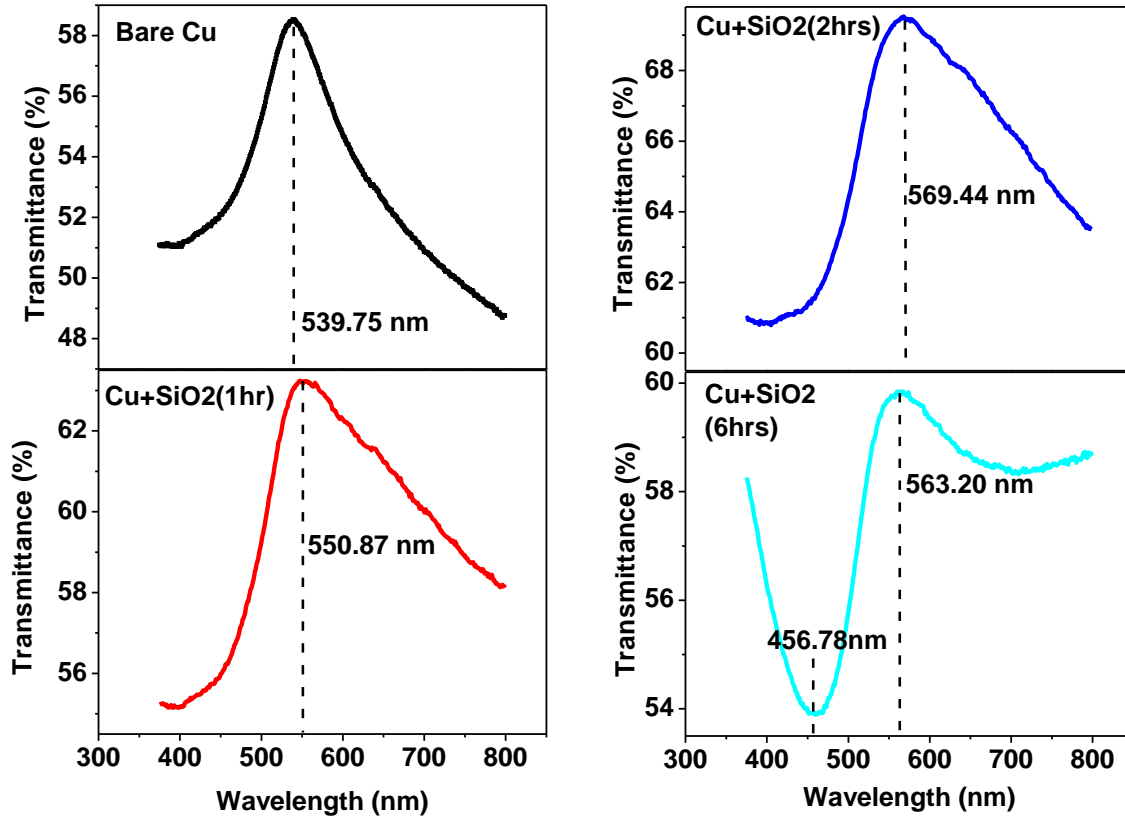


Fig. 4.14: Plot of optical transmittance against wavelength for bare np-Cu's and np-Cu/SiO₂ composites. The duration for sputtering of each SiO₂ and the plasmon resonance positions are indicated on the graph.

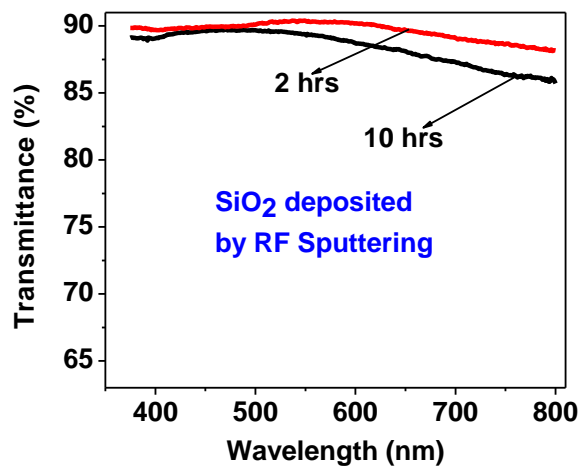


Fig. 4.15: Plot of optical transmittance against wavelength for SiO₂ sputtered on bare glass substrate for two different sputtering times.

On the other hand Fig. 4.15 gives the transmission spectra of SiO_2 sputtered on bare microscopic glass substrate for different sputtering time of 2 hrs (~ 134 nm thickness) and 10 hrs (~ 350 nm thickness). The transmission spectra of the two samples did not show any substantial change in intensity. This observation is crucial for implementing the composite structure in plasmonic solar cell where is it desirable to achieve maximum coupling of light wave into the active layer of the cell. Besides, the fact that the optical transmittance of SiO_2 does not vary appreciably with thickness can be viewed as experimental evidence that our RF sputtered SiO_2 is low in impurity.

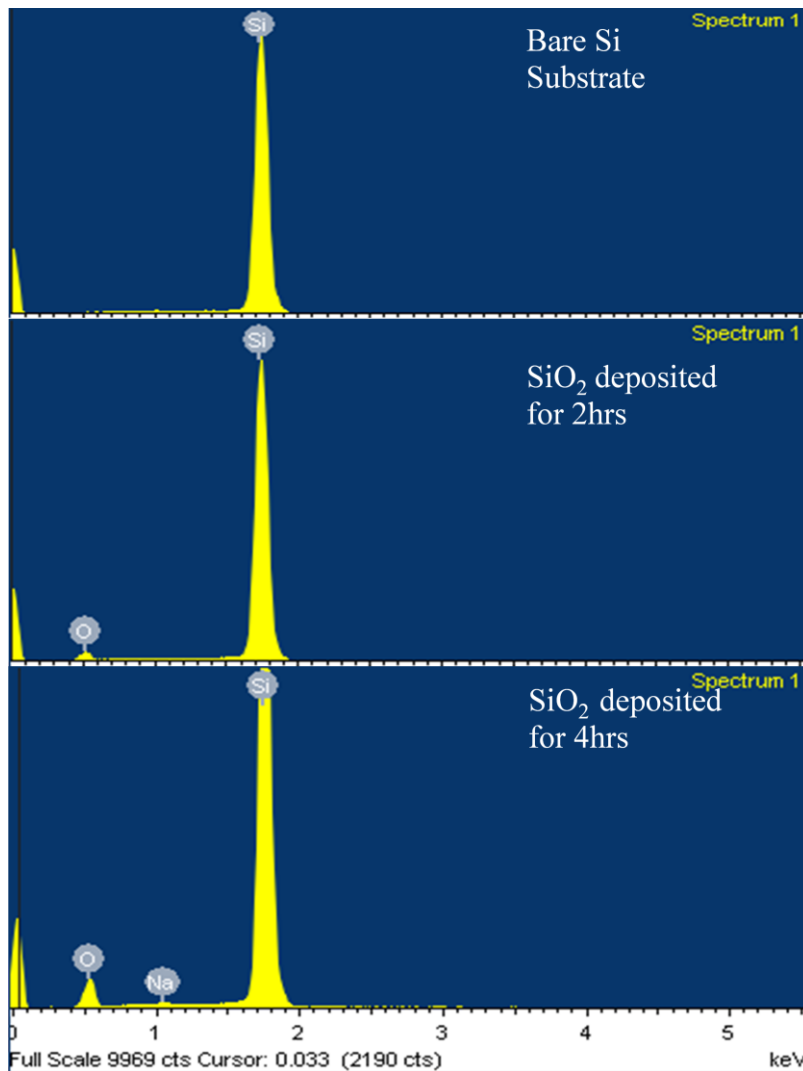


Fig. 4.16: EDX spectra of SiO_2 sputtered on Si (100) for two different sputtering times. The bare Si substrate has been included for comparison.

In order to verify the composition of the SiO₂ obtained by RF sputtering, we carried out energy dispersive x-ray spectroscopy (EDX) measurements on two samples deposited for 2 hrs and 4 hrs respectively. The result which is shown in Fig. 4.16 gives the elemental composition of the bare Si substrate and those of the SiO₂ deposited on it. The percentage of atomic contents obtained from this measurement is shown in Tables 4.2 and 4.3, where it can be seen that, although Na appears in the spectrum of the sample deposited for 4 hours, its content (which is in trace amount) may not affect the optical properties of our RF sputtered SiO₂ significantly. However, the low oxygen content in the samples, as observed in Tables 4.1 and 4.2, may imply that the thin films are porous, and not completely smooth. So, part of the Si seen in the SiO₂ spectra comes from the Si substrate.

Table 4.1: Weight and atomic % of elements observed from the EDX for SiO₂ sputtered on Si (100) for 2 hrs

Element	Weight%	Atomic%
O K	5.58	9.40
Si K	94.42	90.60
Totals	100.00	

Table 4.2: Weight and atomic % of elements observed from the EDX spectra for SiO₂ sputtered on Si (100) for 4 hrs

Element	Weight%	Atomic%
O K	11.40	18.41
Na K	0.27	0.31
Si K	88.33	81.28
Totals	100.00	

Furthermore, we carried out a study to determine the effect of thermal treatment on our np-Cu/SiO₂ composite by subjecting the samples to different annealing temperatures from 200 to 500°C for 1hr. The thermal treatment was carried out in the glove box. Fig 3.41 shows the topographic and optical images as well as the intensity map of the np-Cu/SiO₂ composite annealed at 500°C for 1hr.

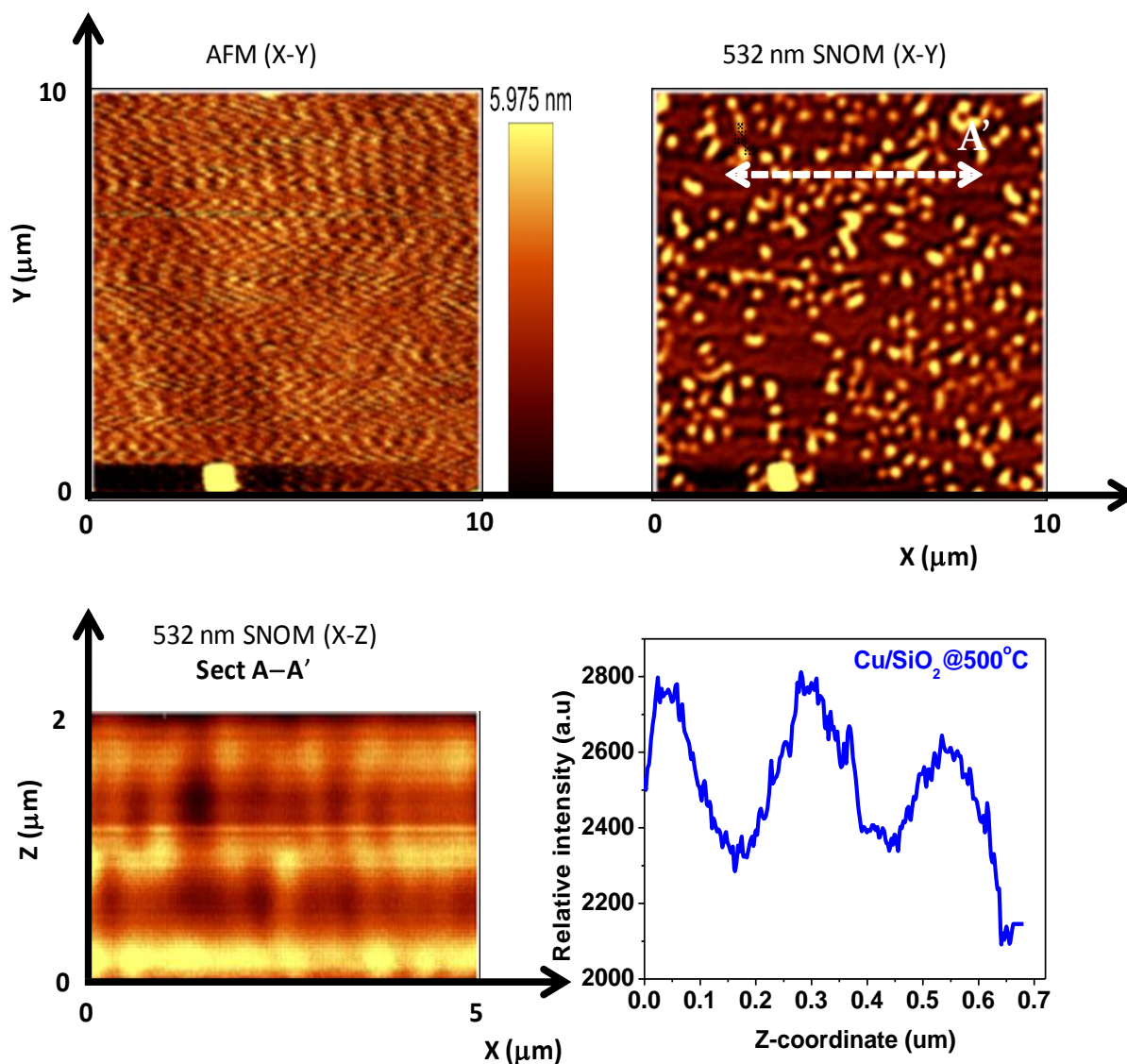


Fig. 4.17: x-y topographic images (top left), x-y optical image (top right), x-z intensity map (bottom left) and scattered wave intensity as a function of the distance from the sample surface (bottom right) of np-Cu/SiO₂ composite annealed at 500°C for 1 hr.

The intensity remains high but the position of the first peak of scattered wave has been reduced to 100 nm from the composite surface. The scattered wave also appears noisy and can be an indication that the composite structure may no longer be optically homogenous after annealing at 500°C. However, the far field UV-VIS spectra given in Fig. 4.18 shows that thermal treatment of the composite does not result in any significant change in the UV-VIS transmittance spectra. Similar to what we observed in Fig. 4.14, the peak position shifts to longer wavelength, compared to the reference bare np-Cu spectrum. This is an indication that np-Cu's may have grown in size as it forms a composite structure with the SiO₂ during sputtering.

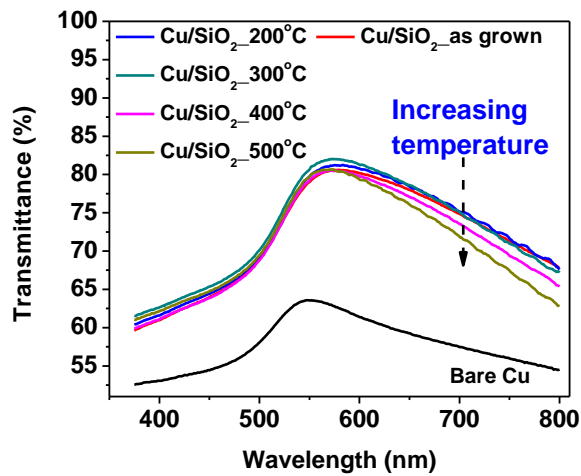


Fig. 4.18: Plot of optical transmittance against wavelength for bare np-Cu's on glass substrate and np-Cu/SiO₂ composite fast-annealed at different temperatures for 5 mins.

4.6 Concluding remarks

We explored and determined experimentally, using a collection mode SNOM technique, the positions of scattered light associated with the propagating component of the electric field that results from the interaction of plane waves with np-Cu's. These propagating higher order modes observed at position orthogonal to np-Cu's surface occurs at $z \geq 200$ nm. In order to reduce the height, and, induce strong localization of these modes in the proximity of np-Cu's, SiO₂ has been incorporated atop the nanoparticles. Consequently, larger amplitude and broadened scattered wave that extends up to $z = 500$ nm, was observed from the sample surface. The study provides an improved insight that helps to understand the physical mechanisms that may hinder the

expected efficiency when these particles are used to enhance performance in photoactive devices, for instance in plasmonic solar cells. The observed coupling of the scattered light to the np-Cu/SiO₂ surface is a step in the right direction for gainful use of these particles in plasmonic thin film organic solar cell architecture.

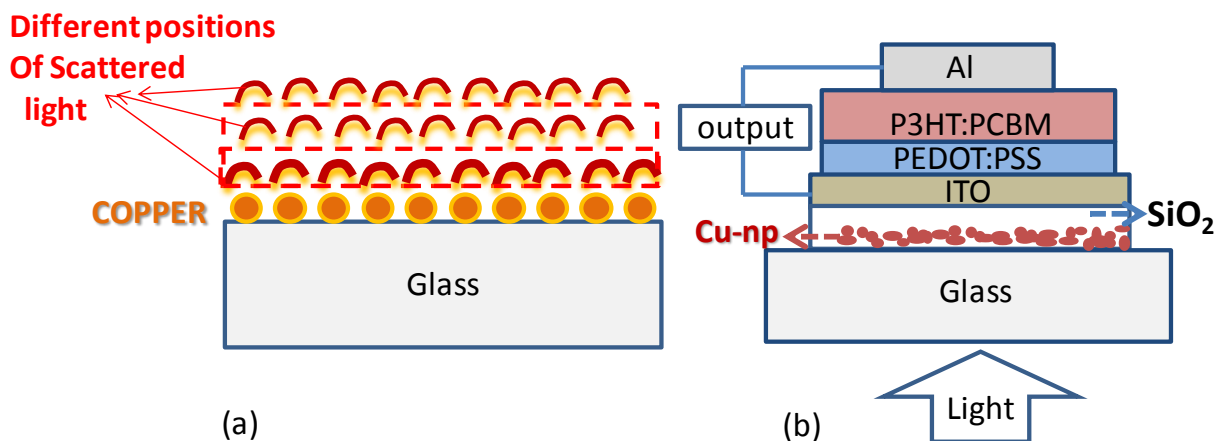


Fig. 4.19: Schematic illustration of (a) possible positions of light scattered from np-Cu and (b) organic solar cell architectural design aimed at maximizing the light scattered by these np-Cu's.

For this reason, we propose a new architectural design aimed at maximizing the result from this study. The proposed architecture shown in Fig. 4.19, is different, because the nanoparticles are deposited outside, and separated from the bulk layer by SiO₂ spacer, from where the np-Cu's can scatter light into the active layer of the cell. Since excitons generally travel short distance during their lifetime in polymer semiconducting materials, the organic photoactive layer can therefore be made sufficiently thin, with the reduction in the thickness complemented by enhanced scattering cross-section of these particles. The large amplitude of the scattered light is absorbed in the active layer to generate excitons that can be dissociated and collected to produce photocurrent.

4.7 References

- [1] D. Courjon and C. Bainier, Rep. Prog. Phys. 57, 989-1028(1994).
- [2] C. F. Bohren, D. R. Huffman, *Absorption and Scattering of Light by Small Particles*, Wiley, New York (1983)
- [3] <http://www.witec.de/>
- [4] M. De Serio, R. Zenobi, V. Deckert, Trends in Analytical Chemistry. 22(2), 70 - 77 (2003).
- [5] <http://www.nanonics.co.il/>
- [6] K.R. Catchpole and A. Polman, Opt. Express. 16, 21793 – 21800 (2008).
- [7] Y. Afsar, J. Sarik, M. Gorlatova, G. Zussman, and I. Kymissis, <http://enhants.ee.columbia.edu/images/papers/EvaluatingYafsarIPSC2012.pdf>
- [8] E. T. Yu, D. Derkacs, S. H. Lim, P. Matheu and D. M. Schaadt, Proc. of SPIE. 7033 70331V-1 (2008).
- [9] H. R. Stuart and D. G. Hall, Appl. Phys. Lett. 69(16), 2327-9 (1996).

Chapter 5

5 Electro-optical properties of metal- polymer and polymer-polymer nanocomposites

In the previous chapters we discussed in detail the properties of np-Cu's as they relate to the deposition and annealing conditions and we showed the physical mechanisms and the most promising structural design that will lead to plasmonic thin film solar cells with embedded np-Cu's. In this chapter, we turn to a component of the architecture of a thin film solar cell, which is considered to be important for efficient collection of photogenerated charges and, namely, the transparent electrode. We explored transparent electrodes based on nanocomposites incorporating np-Cu's and fabricated on flexible polyethylene terephthalate (PET) substrates.

In the first section of this chapter, we show that we can fabricate polymer-metal nanoparticle composites by incorporating np-Cu's on graphite nanosheets produced by vacuum filtration of exfoliated nanographite suspensions. In the subsequent section, we will discuss the fabrication and properties of nanocomposite thin films produced by spin coating poly(3,4-ethylenedioxy-thiophene):poly(styrenesulfonate) (PEDOT:PSS), a standard solar grade material, on flexible plastic substrates coated by a commercial-grade transparent carbon film (TCF) based on multilayer graphene flakes. These substrates can also be used as transparent electrodes for thin film plasmonic solar cells and to incorporate np-Cu's.

5.1 Graphite nanosheet with embedded copper nanoparticles

5.1.1 Preparation of nanocomposite of Graphite nanosheet and copper nanoparticles

Graphite nanosheets with embedded copper nanoparticles were fabricated by incorporating via sputtering, np-Cu's on solution processed graphitic nanosheets. The preparation of graphite nanosheet films has been carried on by means of a well established procedure that is available in the literature [1]. The procedure starts with the exfoliation of nanographite in a water based solution using sodium dodecylbenzenesulfonate (SDBS) as surfactant. The solution (Sigma-Aldrich: Cat. # 28995-7) was prepared by dissolving 500 mg of SDBS in 1000 ml of distilled water, followed by 30 minutes of sonication. This is done in order to dissolve completely the

surfactant in distilled water and form a homogenous solution. Next, 0.1g of nanographite (Aldrich: lot. # 332461) was added to the surfactant solution. The top portion of the mixture is collected after sonication for 4 hours and allowed it to sit for 8 hours. The decanted upper part of the mixture is used for centrifugation (Fisher Scientific; accuSpin™ 400) at 6000 rpm for 1 hr. Graphite nanosheet film was prepared by vacuum filtration of 20 ml of suspension of exfoliated nanographite on a cellulose membrane. The choice of 20 ml of suspension to be filtered was made for optimizing the transmittance and conductivity of the films. We desire to fabricate a film that covers the most part of the substrate while at the same time maintaining good transmission of light. This will help to deposit the np-Cu's only on the graphite nanosheets. Reducing the filtration volume leads to films with high transmittance (see Fig. 5.1) but with low fraction of covered area. After filtration, the film on the filter membrane is transferred onto a glass substrate and baked in an oven at 50°C for 5 hrs. Etching of the sample (to eliminate the filter membrane) was carried out using consecutive acetone and methanol baths. The resulting graphite nanosheet film on glass is used as the substrate for sputtering copper to form graphite /copper nanocomposites. The nanocomposite sample was characterized using AFM, SEM and UV-VIS.

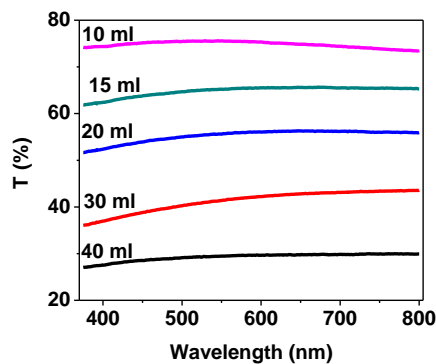


Fig. 5. 1: Transmittance spectra of graphite nanosheets obtained from vacuum filtration of different volumes of solution as indicated.

5.1.2 Morphology and composition of Graphite nanosheets with embedded copper nanoparticles

The morphology of the composite structure formed by sputtering copper particles on solution processed graphite nanosheets was investigated with the aid of scanning electron microscope (SEM). We performed using a LEO (Zeiss) 1530 field emission microscope operating at 5-KV electron acceleration voltage. Fig. 5.2 shows the SEM images obtained after annealing our sample at 300°C for 1 hr. in the glove box. Panel (a) and (b) represent the same image at different magnifications. The two images were taken from a side of the sample where no graphite nanosheets were deposited. From Panels (a) and (b) we observe well-separated copper particles on glass, Panels (c) and (d) show the investigated nanocomposite, comprising homogeneous np-Cu's on graphite nanosheets. The particles appear larger than the ones grown on the bare glass substrate.

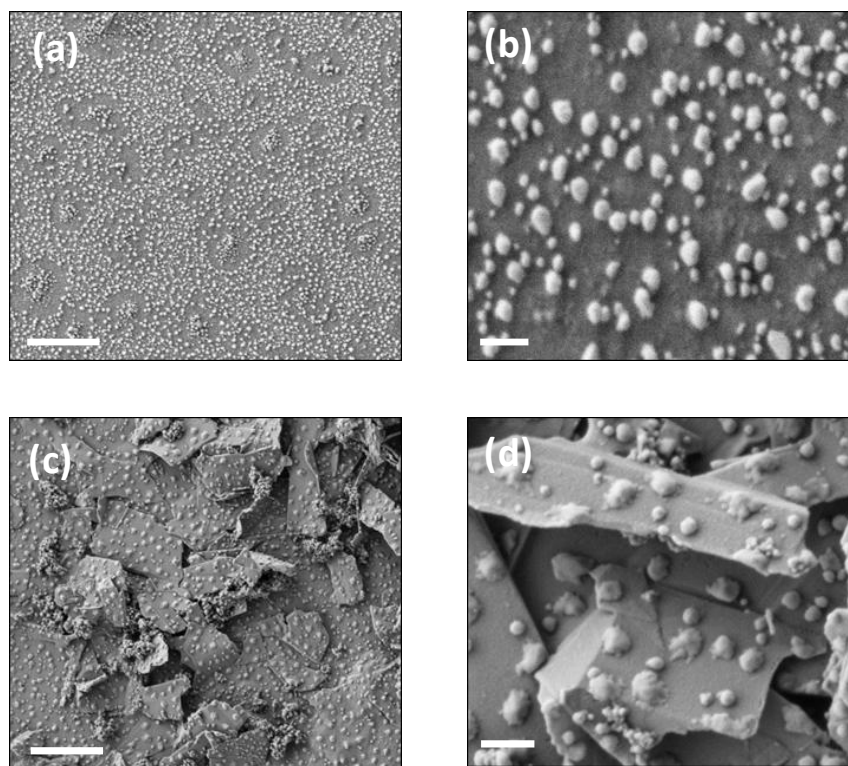


Fig. 5. 2: SEM image of thermally treated np-Cu's on bare glass substrate at magnification of (a) 10K and (b) 72K and that of graphite nanosheet with embedded np-Cu's at magnification of (c) 10 K and (d) 50K. The scale bar in the left images represents 1 μ m (a, c) and in the right images (b, d) 200 nm.

Similar results were obtained from AFM scans as shown in Fig. 5.3. However, what appears in the SEM images as np-Cu on bare glass substrate actually contains some fibrous carbon-like material beneath. The appearance of the fibrous carbon-like material was confirmed by the energy dispersive x-ray spectroscopy (EDX) analysis carried out on both sides of the sample as well as on plain glass substrate. The result of this analysis is shown in Fig. 5.4. Table 5.1 shows that carbon content of the sample is about 14% in the region occupied by graphite nanosheets compared to ~ 4% obtained from plain glass. The table also shows that copper nanoparticles obtained after thermal treatment in the glove box suffer little or no oxidation.

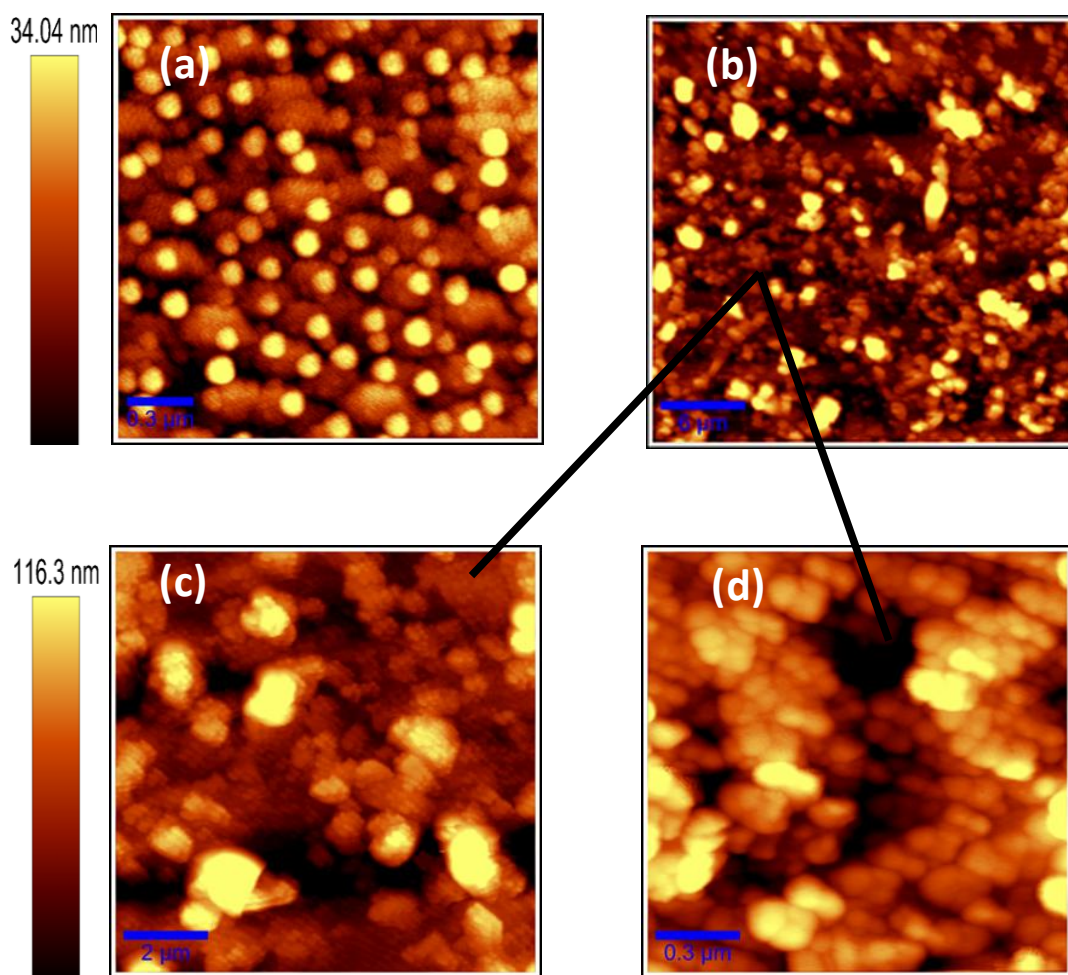


Fig. 5. 3: AFM images of thermally treated (a) np-Cu's and (b) composite of graphite nanosheet/np-Cu on glass substrate. Sample (b) has been scanned at higher resolutions as indicated in panel (c) and (d).

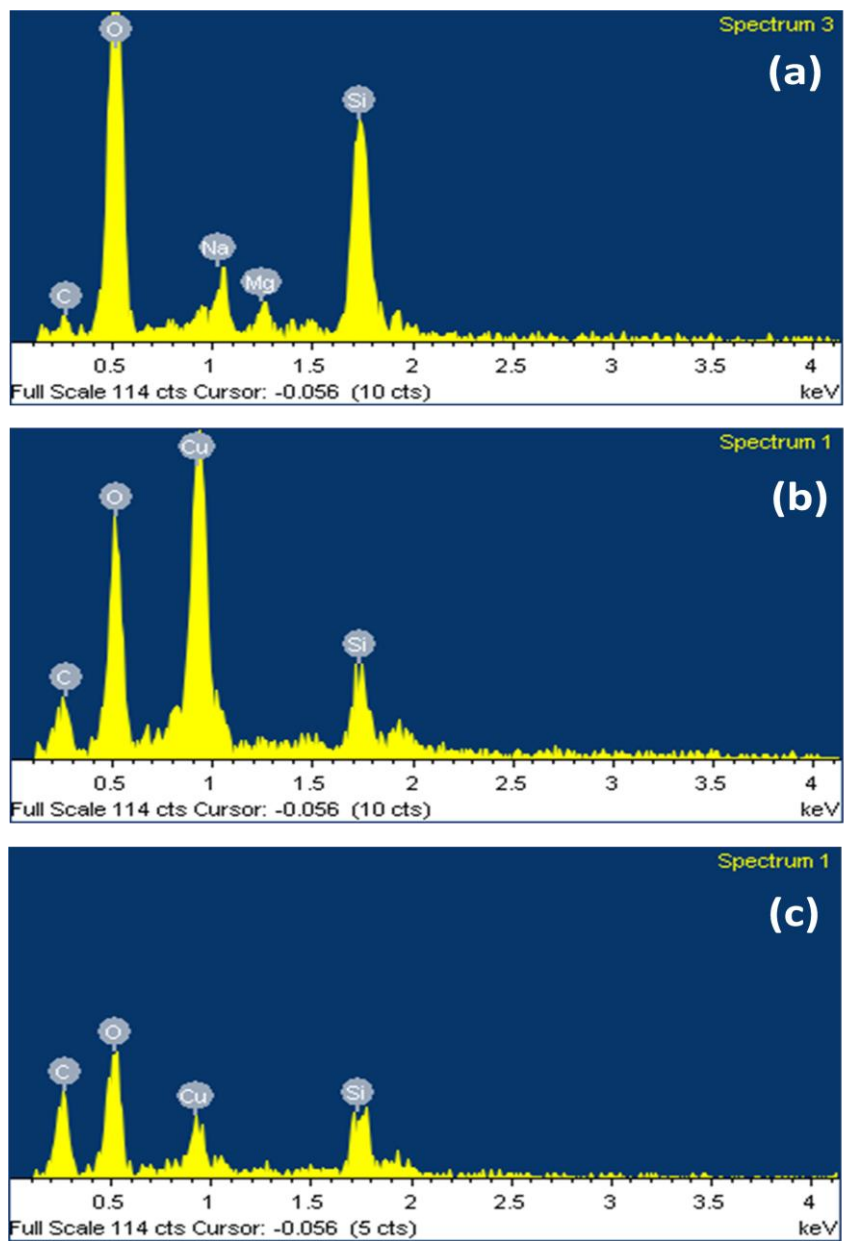


Fig. 5. 4: EDX spectra of (a) bare glass substrate, (b) np-Cu deposited on glass and (c) nanocomposite on glass composed of graphite nanosheets and np-Cu's. The EDX analysis was carried out after the sample has been annealed in the glove box at 300 nm for 1 hr.

Table 5. 1: The elemental composition of bare glass substrate, np-Cu's and graphite nanosheet/np-Cu nanocomposite obtained from EDX analysis shown in Fig. 4.2

Elements	Carbon	Oxygen	Sodium	Magnesium	Silicon	Copper
Atomic %						
Bare glass substrate	3.87	55.78	3.93	2.80	33.62	-
Copper sample	13.51	30.97	-	-	15.37	40.15
Nanocomposite	36.60	38.34	-	-	18.61	6.45

In order to obtain the size distribution of np-Cu's, the SEM micrograph (Fig. 5.2, panel b) was analyzed using Image J software and the result is given in Fig. 5.5, where it is seen that the particle distribution follows very closely a Gaussian function. The average particle size obtained from this analysis is 65 nm, with area coverage of about 20%.

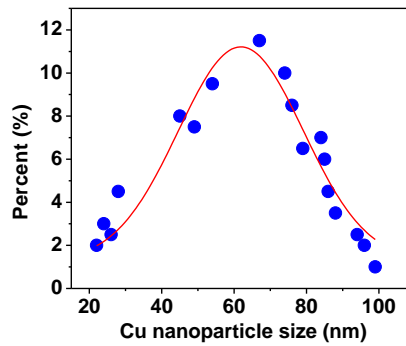


Fig. 5. 5: Copper nanoparticle size distribution obtained from the SEM image presented in Fig. 4.1 (b). The distribution has been fit to a Gaussian function (solid line).

5.1.3 Measured Optical spectra of Graphite nanosheets with embedded copper nanoparticles

In Fig. 5.6, the transmittance spectra before and after thermal annealing are plotted for the bare graphite nanosheet, the nanocomposite structure and bare np-Cu's. The spectra were measured in the spectra region between 375 nm and 800 nm wavelength.

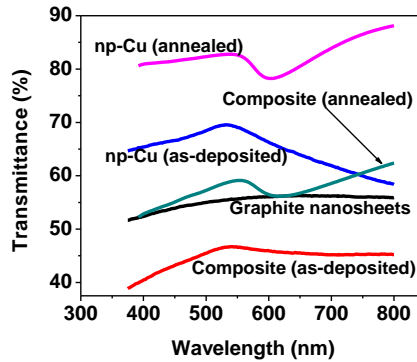


Fig. 5. 6: Transmittance spectra of graphite nanosheets on glass, np-Cu's on bare glass and graphite nanosheets with embedded copper nanoparticles before and after thermal treatment in the glove box.

The transmittance spectrum of the bare graphite nanosheet did not show any evidence of plasmonic behavior. The inclusion of np-Cu's modifies the optical spectrum, which now shows collective resonance effects. For np-Cu's grown on graphite nanosheets, a shift of the resonance position to higher wavelengths and broadening of the spectra plasmon line were found, in comparison to the spectrum of bare np-Cu's. The resonance position in bare np-Cu's and the graphite nanosheet coated with np-Cu's is observed at 601 nm and 617 nm, respectively. This means that the resonance position shifts to longer wavelengths when np-Cu's are deposited on graphite nanosheets. According to the SEM and AFM images in Fig. 5.2 and Fig. 5.3, the particle sizes are bigger in the composite structure. Therefore, we attribute the shift to large np-Cu's when they are grown on graphite nanosheets. In addition, a transmittance enhancement is observed in both the annealed and as-deposited composite structures. The appearance of such a transmittance enhancement is associated with the metallic properties of np-Cu's near the

percolation threshold [2]. The peak position shifts from 541 nm to 554 nm, representing a red shift of 13 nm.

In conclusion, the observed optical behavior due to the inclusion of np-Cu's is critical in determining the optical absorption in the nanocomposite.

5.1.4 Electrical characterization of Graphite nanosheets with embedded copper nanoparticles

The sheet resistance of thermally treated graphite nanosheets and np-Cu/graphite nanosheets was measured from I-V curves recorded on a Signatone S-725 probe station using a Keithley 2400 source meter. Voltages in the ± 2 V range were applied in order to obtain the current – voltage curves shown in Fig. 5.7.

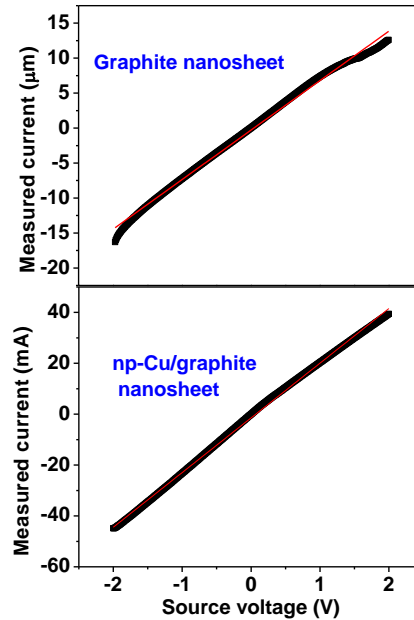


Fig. 5.7: I-V curves of graphite nanosheets and np-Cu/graphite nanosheets composite recorded from a probe station.

We observed a three-fold increase in the measured current from ± 15 μ A in the bare graphite nanosheets to ± 40 mA in the nanocomposite. The associated sheet resistance dropped from ~ 140 K Ω to ~ 46 Ω , signifying a huge enhancement in the electrical conductivity of the composite. This enhancement can be attributed to the deposition of the np-Cu's nanoparticles on the graphite

nanosheet, enabling the formation of conduction pathways for electron transport. The observed enhancement can be beneficial, for the application of these materials in organic solar cells where they can be used as hole collector electrodes.

5.2 Properties of a Poly(3,4-ethylenedioxythiophene):poly(styrenesulfonate) composite medium with graphene nanoplatelet inclusions

Poly(3,4-ethylenedioxy-thiophene):poly(styrenesulfonate) (PEDOT:PSS) is an organic polymer that can be used to prepare transparent and conducting thin films combining the physical properties of indium-tin oxide (ITO) with the advantageous properties of plastics, including low weight, high flexibility and ease in processability [2-4]. For these reasons, PEDOT:PSS is widely used as a hole-transporting layer in organic solar cells (OSC) [7, 8] and organic light-emitting devices (OLED) [9, 10]. In this section we present the results of our investigation on the optical and electrical properties of nanocomposite thin films produced by spin coating a layer of PEDOT:PSS on flexible plastic substrates coated by a commercial-grade transparent carbon film (TCF) prototyped by 3M Canada Company, which has the potential to be used as another substrate for growing np-Cu's.

5.2.1 The spin coating operation and sample characterization

Transparent carbon film (TCF) on polyethylene terephthalate (PET), directly provided by 3M Canada Co., were filled by PEDOT:PSS in ambient conditions using a commercial spin coater (Laurell Co.). PEDOT:PSS ink (Aldrich) was filtered through a 0.8 μm -pore filter and mixed with methanol at 1:1 ratio in volume prior to use. In order to promote adhesion, the TCF-coated PET substrate was made hydrophilic using ozone treatment (UV3 Novascan apparatus). The PEDOT:PSS ink was allowed to rest on the TCF-coated PET substrate for 5 min before spinning for 3 min. A set of samples was made by varying the spinning speed from 500 to 2500 rpm. This coating stage was followed by fast spinning (8000 rpm, 1 min) in order to expedite drying of the samples. Reference samples were spun on bare PET under similar conditions.

5.2.2 Morphology characterization of PEDOT:PSS/TCF nanocomposites

Figure 5.8 compares the thickness of our PEDOT:PSS samples grown on TCF-coated PET substrates with similar PEDOT:PSS samples spin-coated on bare PET. This figure shows that the thicknesses of TCF coated with PEDOT:PSS are always higher than the thickness of bare TCF, and decreases at increasing spinning speed. Thickness control is a primary concern for the efficient use of PEDOT:PSS as an interlayer in organic solar cells and organic light emitting devices. Therefore, the possibility to tune the thicknesses of our composite films is of primary importance for their practical applications.

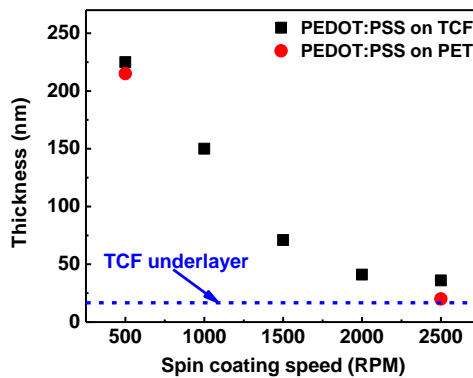


Fig. 5.8: Variation of the thickness of the films with the spin coating speed. The dotted line is the thickness of graphene based TCF on a bare PET substrate.

On the other hand, the range of thicknesses of PEDOT:PSS films produced in this work exhibits a strong dependence on the spinning speed. PEDOT:PSS films spun on TCF-coated PET have thicknesses $d_{tot} = 225 \pm 5$ nm at 500 rpm and $d_{tot} = 32 \pm 5$ nm at 2,500 rpm, respectively. Our data show that films spun on TCF-coated PET are slightly thinner than the sum of the thicknesses of bare TCF films ($d_{TCF} \approx 22 \pm 5$ nm) and the thickness, d_{bare} , of PEDOT:PSS layers spun on bare PET. For instance, at 500 rpm, $d_{TCF} + d_{bare} = 237 \pm 5 > d_{tot} = 225 \pm 5$ nm and, at 2500 rpm, $d_{TCF} + d_{bare} = 43 \pm 5$ nm $> d_{tot} = 32 \pm 5$ nm. These results elucidate the contribution of the substrate surface to the final film thickness and indicate that, during the spinning operation, a significant fraction of PEDOT:PSS penetrates in between the few-layer graphene flakes forming the TCF film. Accordingly to these results, we infer that, when TCF-coated PET substrates are spun with PEDOT:PSS, a bi-layer thin film is formed, with a bottom layer comprising a nanocomposite formed by graphene flakes interpenetrated by PEDOT:PSS and a top layer of

pure PEDOT:PSS. The fact that the top surface of our films is always formed by PEDOT:PSS and is completely free from floating graphite nanoplatelets is confirmed by SEM micrographs, as shown in Fig. 5.9.

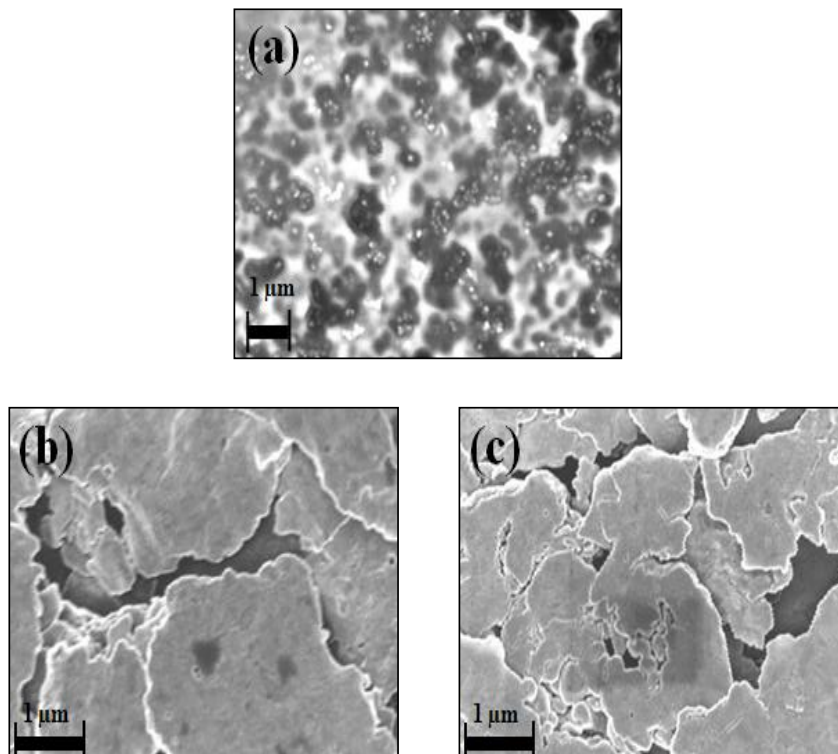


Fig 5. 9: Scanning electron micrographs of (a) Graphene based TCF on bare PET and PEDOT:PSS films spun at 2500 rpm on (b) Bare PET and (c) Graphene based TCF.

In this figure, panel (a) shows the morphology of a bare TCF prior to deposition of PEDOT:PSS by spin coating. It can be observed that, although these industrial-grade films present a relatively large fraction of few-layer graphene platelets, they also contain a number of graphitic nanoparticles. In the same figure, panels (b) and (c) compare PEDOT:PSS films spun at 2500 rpm on bare and TCF-coated PET substrates and demonstrate that graphitic nanoparticles have a quite limited effect on the surface morphology of PEDOT:PSS, which is basically the same in the two cases. In both panels (b) and (c), top surfaces are formed by relatively large and closely packed PEDOT:PSS domains, with the islands being only slightly smaller in the presence of an underlying TCF film. An explanation for the morphology of PEDOT:PSS in the absence of carbon flakes can be inferred from the model proposed by Nardes et al. [13], who suggested that the structure of spin-coated PEDOT:PSS thin films consists of particles containing both PEDOT

and PSS chains surrounded by a shell formed only by PSS. Our samples are in good agreement with this model, also in the case of PEDOT:PSS incorporating graphene flakes. PEDOT chains tend to stick to themselves, forming relatively large, electrically conducting, agglomerates and domains irrespectively of the presence of graphene platelets from the TCF.

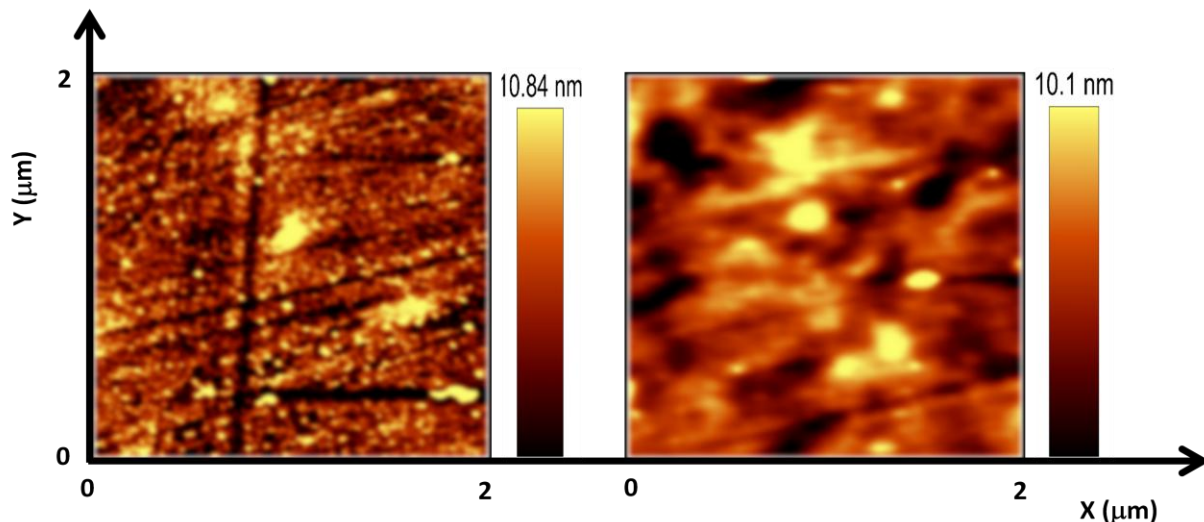


Fig. 5. 10: AFM micrographs of bare PET substrate (left) and Graphene based TCF on PET substrate (right).

Figure 5.10 shows the AFM micrographs for the bare PET substrate (left), and a TCF-coated PET substrate in the absence of PEDOT:PSS (image on the right hand side). Similarly, we display in Fig. 5.11 our PEDOT:PSS-coated samples prepared at the two extreme spinning speeds, 2500 rpm (panel a and b) and 500 rpm (panels c and d). Panels a and c refer to PEDOT:PSS films spun on bare PET substrates, while panels b and d are micrographs from PEDOT:PSS spun on TCF-coated PET. Since our AFM images ($1.5 \times 1.5 \mu\text{m}$) are taken at larger magnification than the SEM images, the grain-like structures observed in figure 4.10 represent a distribution of the PEDOT and the PSS species within the individual domains, with a level of details that cannot be resolved by SEM.

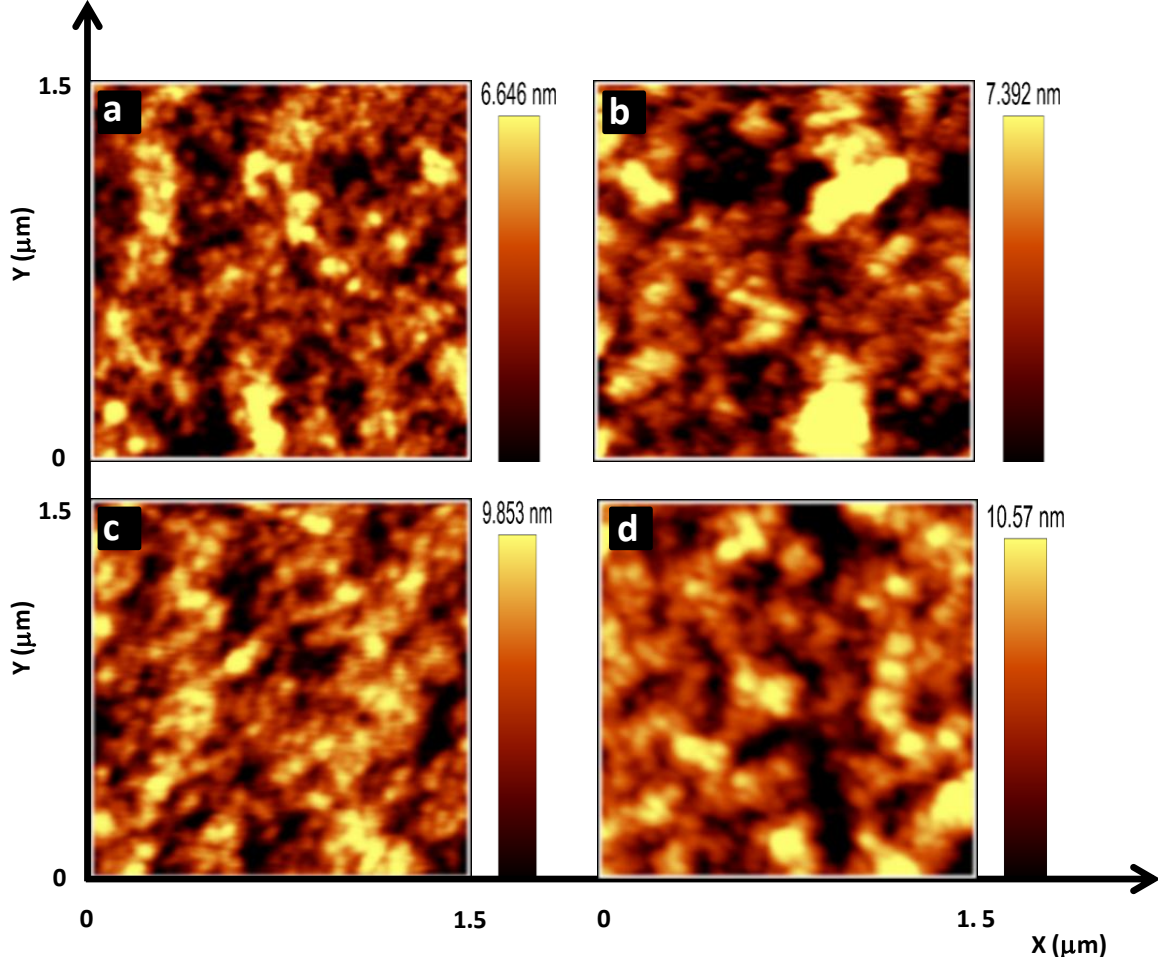


Fig. 5. 7: AFM topography images of PEDOT:PSS spin-coated on (a) bare PET at 2500 rpm, (b) TCF coated PET at 2500 rpm, (c) bare PET at 500 rpm and (d) TCF coated PET.

From visual observations, each PEDOT:PSS film spun on TCF-coated PET substrates does not appear to be rougher than the corresponding film on bare PET. Only the PEDOT:PSS domains appear to be smaller in size in the case of TCF-coated PET substrates. Such observation suggested us to perform a more quantitative analysis of roughness in a larger set of micrographs such as those demonstrated in Figs 5.10 and 5.11. The root mean squared (RMS) roughness for domains of PEDOT:PSS in different samples was determined as:

$$\text{RMS} = \sqrt{\frac{1}{N} \cdot \left(\sum_{i=1}^N |z_i - z_{av}|^2 \right)} \quad (5.1)$$

where $N = 512 \times 512$ is the number of pixels contained in each AFM image, z_i is the topographic height of the i -th pixel and z_{av} is the average height of the AFM image. The surface skewness (SSK) is defined as the asymmetry of the height distribution histogram by the equation:

$$SSK = \frac{1}{N \cdot (RMS)^3} \cdot \left(\sum_{i=1}^N |z_i - z_{av}|^3 \right) \quad (5.2)$$

where $SSK = 0$ indicates a symmetric distribution of z_i , with the same amount of voids and pinholes in the sample, while positive and negative values of SSK are indicative of a flat surface with peaks or potholes, respectively. Results obtained using eqs. 1 and 2 are shown in Fig. 5.12. For each sample, this figure represents the average over the RMS roughness values obtained from ten different scanned regions.

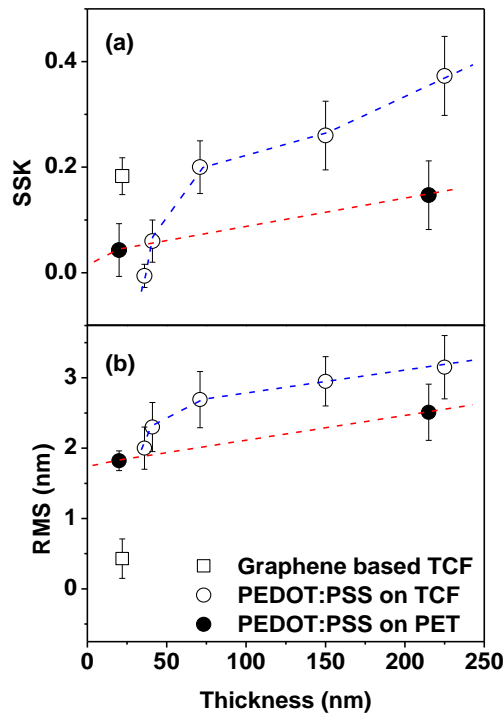


Fig. 5.12: Average values of (a) Surface skewness (SSK) and (b) Root mean squared roughness (RMS) of graphene based TCF layer and PEDOT:PSS films spin coated on bare PET and TCF-coated PET. Measured values of SSK and RMS for bare PET are 0.04 ± 0.01 and 0.21 ± 0.05 nm, respectively. The error bars account for the standard deviation for several measurements carried out on different areas of the same sample.

The bare TCF layer is relatively smooth with an RMS roughness of about 0.4 nm which is nearly comparable to that of the PET substrate. It can be observed from Fig. 5.12(b) that the surface roughness of the overlying PEDOT:PSS coating increases almost linearly with the thickness of the film, and is less significantly influenced by the type of surfaces used during the spin coating process. This can be seen from the relative increase in the RMS values of the films having the extreme thickness values. At 2500 rpm, the increase in the surface roughness is about 10% between the films spin coated on bare PET and TCF-coated PET. The increase is approximately 25% for films spun at 500 rpm. However, we observe more significant increases in RMS roughness, by 38% when the thickness increases from 20 to 225 nm on bare PET and by 58% when the thickness increases from 32 to 225 nm on TCF-coated PET, respectively. This is an indication of the fact that the most relevant influence factor controlling the roughness of the films is not the presence of graphene flakes, but the lack of coalescence of PEDOT:PSS domains as the thickness of the film increases.

On the other hand, while the underlying graphene layer has a limited effects on the RMS roughness of the top PEDOT:PSS surface, the surface skewness is mostly determined by the spinning speed, irrespectively of the presence of the underlying TCF film. This consideration supports the idea that, during the spin coating process, PEDOT:PSS inter-mingles with the underlying TCF layer and, potentially, forms a composite that does not disturb the distinct layer forming on top of it. We anticipate that this observation is crucial in order to understand the interference effects observed in the optical transmission spectra.

5.2.3 Optical properties of PEDOT:PSS composite medium with graphene nanoplatelet inclusion

Figure 5.13 shows the transmission spectra of PEDOT:PSS spun on bare PET and TCF-coated PET substrates. The range of wavelengths in this figure has been chosen in order to observe the presence of interference fringes. By comparison with the spectrum of bare TCF (also included in Fig. 5.13) it can be suspected that the differences that are noticeable in the interference fringes are a result of the formation of an interface between the bottom layer comprising an effective medium of PEDOT:PSS and graphene and the top layer of pure PEDOT:PSS (see Fig. 5.14). The presence of such an interface results in a significant phase shift for the light crossing the films,

which superimposes, resulting to an increase in the absorbance of the films as the thickness of the PEDOT:PSS top layer increases.

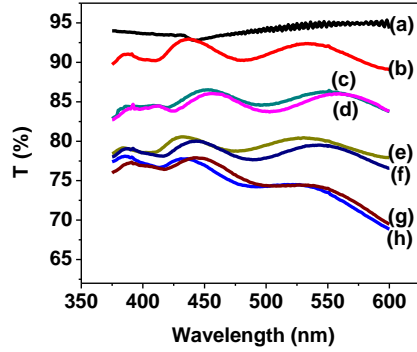


Fig. 5.13: Normal incidence transmission spectra of (a) bare TCF and PEDOT:PSS spun at varying spinning speeds on bare PET at (b) 2500 RPM and on TCF-coated PET substrates at (c) 2500 RPM, (d) 2000 RPM, (e) 1500 RPM, (f) 1000 RPM (g) 500 RPM. The spectral line labeled (h) is for PEDOT:PSS spun on bare PET at 500 RPM. These spectra were used to extract the optical constants of the films.

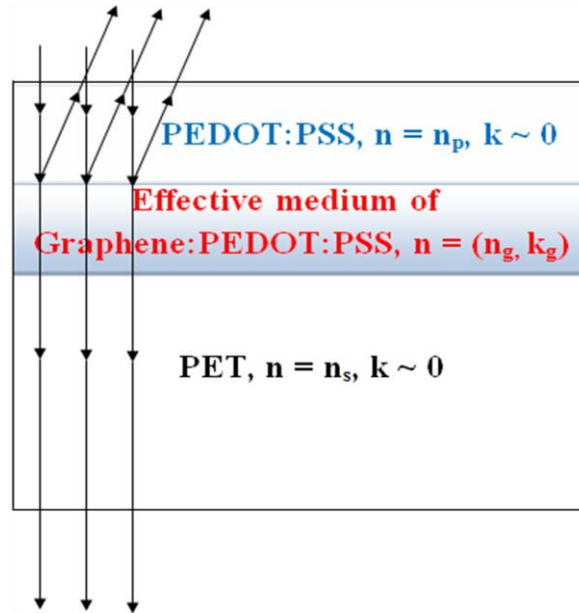


Fig. 5.14: Structural diagram of our composite films showing a bottom layer formed by an effective medium composed by a TCF and PEDOT:PSS and a top layer of pure PEDOT:PSS.

The refractive indices of our bilayer films have been determined on the basis of the interference fringes observed in their transmission spectra. For these estimates, we used an empirical optical model based on the Swanepoel's method of envelopes between maxima and minima of the interference fringes [13]. From fringes produced by multiple reflections of light between the air–PEDOT:PSS and PET–PEDOT:PSS interfaces, we calculated n_p , the refractive index of the PEDOT:PSS top layer. In order to determine n_g , the refractive index of our bottom layer, comprising an effective medium of TCF and PEDOT:PSS, we assumed that such layer is sandwiched between PET substrate and PEDOT:PSS layers, with known refractive indices.

The equation suitable for this laminated structure, shown in Fig. 5.14, can be obtained [15], assuming that:

$$n_g^2 \gg k_g^2 \quad (5.3)$$

$$(n_g - n_p)^2 \gg k_g^2 \quad (5.4)$$

$$(n_g - n_s)^2 \gg k_g^2 \quad (5.5)$$

where k_g is the extinction coefficient of TCF and $n_s = 1.52$ is the refractive index of the bare PET substrate. From the interference maxima (T_{max}) and minima (T_{min}), we obtained the refractive index of the bottom layer according to the equation

$$n_g = \left[N_g + \left(N_g^2 - n_p^2 \cdot n_s^2 \right)^{\frac{1}{2}} \right]^{\frac{1}{2}} \quad (5.6)$$

where

$$N_g = \frac{1}{2} \cdot (n_p^2 + n_s^2) + 2 \cdot n_p \cdot n_s \cdot \left(\frac{T_{max} - T_{min}}{T_{max} \cdot T_{min}} \right) \quad (5.7)$$

From these equations, the effective refractive index of the bottom layer is found to be $n_g = 2.02 \pm 0.06$. We also determined $n_p = 1.78 \pm 0.05$ for PEDOT:PSS, in good agreement with refs. 14-15 and the value that can be inferred from interference fringes in the reference thin film prepared

from pure PEDOT:PSS. Fig. 5.15 confirms that the refractive index of the TCF layer only negligibly changes with the thickness of the PEDOT:PSS top layer.

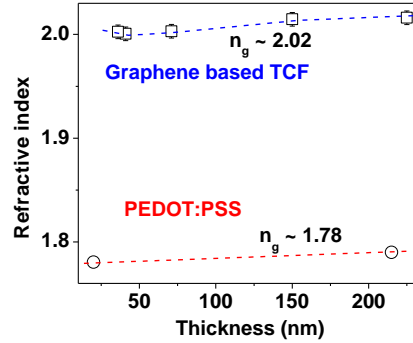


Fig. 5.15: Refractive indices versus thickness of graphene-based TCF and PEDOT:PSS, calculated from the envelope of transmission maxima and minima.

5.2.4 Electrical characterization of the nanocomposite of PEDOT:PSS and graphene nanoplatelet inclusion

Fig. 5.16 compares the sheet resistance (R_{sh}) of PEDOT:PSS spun on bare PET and TCF-coated PET at different thicknesses of the top layer of pure PEDOT:PSS. As can be noticed from this figure, the thickness of PEDOT:PSS strongly influences the electrical properties of the films.

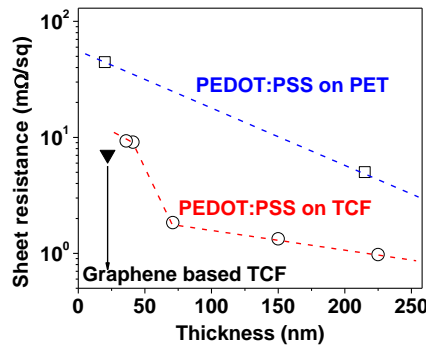


Fig. 5.16: Electrical sheet resistance vs. thickness for films spun at varying spinning speeds on bare PET and TCF-coated PET substrates. The sheet resistance of a bare graphene based TCF on PET has also been included.

A significant improvement is observed when the thickness of PEDOT:PSS increases from 32 nm to 225 nm, resulting to a drop in the value of sheet resistance from $R_{sh} = 9.3 \text{ M}\Omega$ to $R_{sh} = 970 \text{ k}\Omega$. The highest value, $R_{sh} = 44.4 \text{ M}\Omega$, is observed in the thinnest PEDOT:PSS films spun on bare PET, with improvements of a factor 4.5 when a TCF layer is incorporated. Consequently, also the decrease in R_{sh} may be understood by adopting a bi-layer model, on the bases of a parallel between two resistors, where R_{TCF} is the resistance of the bottom layer (controlled by the resistivity of graphene platelets) and R_{PEDOT} is the resistance of the top layer, controlled by the resistivity of PEDOT. In this arrangement, the effective sheet resistance R_{sh} can be written as:

$$\frac{1}{R_{eff}} = \frac{1}{R_{TCF}} + \frac{1}{R_{PEDOT}} \quad (5.8)$$

Since R_{TCF} is independent of the spin coating speed and the total film thickness, the observed change in R_{sh} is mainly caused by the decrease of R_{PEDOT} , which is proportional to the film thickness. This is in agreement with Fig. 5.16 that shows that the increase of R_{sh} becomes linear as the thickness of the PEDOT:PSS component of the bilayer film exceeds that of the TCF sublayer (i.e. for $d_{tot} \geq 50 \text{ nm}$). Therefore, adding a TCF bottom layer, which was beneficial for improving the optical properties of the films, is found to not significantly improve the electrical properties.

5.3 Conclusion

We demonstrated methods to obtain nanocomposites with improved properties. Improvement was obtained in the optical transmittance of graphite nanosheet which showed resonance absorption at 617 nm spectral position, associated with np-Cu inclusion. Improvement was also recorded on the electrical properties of the nanocomposites with a reduction in the sheet resistance from 140 $\text{K}\Omega$ to 46 Ω as a result of np-Cu inclusion. This observation suggests to us that the incorporation of np-Cu's on the graphite nanosheets provides the interface or conduction pathways for improved charge transfer between the nanosheets and, together with the transmittance enhancement, the nanocomposite can be a good candidate as hole collector electrode in thin film organic solar cell.

Furthermore, we showed that PEDOT:PSS can be used to coat commercial nanographite sheets on flexible substrate such as PET and provide good adhesion with thickness ranging from

~200 nm down to ~20-30 nm (close to the thickness of the graphene-based TCF). The coated films are optically homogeneous and continuous in the visible region, as witnessed by the interference fringes on the transmission spectra. By creating the envelope of the interference maxima and minima, we found the refractive indices of our graphene based TCF and PEDOT:PSS in the range of 2.02 ± 0.6 and 1.78 ± 0.1 respectively. We showed that the reduction in the optical transparency could be linked to the attenuation at the interfacial layer due to reflection, scattering and absorption within the PEDOT:PSS domains. Many of the other properties (electrical, morphological) were also studied on the bases of two-layer model, with one layer formed by an effective medium of Graphene based TCF/PEDOT:PSS and a second layer of pure PEDOT:PSS layer superimposed to it. There were small beneficial effects of having TCF underlayer on the electrical properties of the composite films. However, these effects are dominated by the electrical properties of PEDOT:PSS, as the thickness of the latter increases beyond 50 nm. The good adhesion of PEDOT:PSS on graphene and the homogeneity of these films suggest that they can be suitable substrates, alternative to “pure” graphene nanosheets, for growing np-Cu’s for plasmonic solar cell applications.

5.4 References

- [1] M. Lotya, Y. Hernandez, P.J. King, R. J. Smith, V. Nicolosi, L.S. Karlsson, J. AM. Chem. Soc. 2009, **131**, 3611 (2009)
- [2] S. Ding, X. Wang, D.J. Chen and Q.Q. Wang, Optics Express, **14(4)** 1541 (2006)
- [3] M. Shibusawa, M. Kobayashi, J. Hanari, K. Sunohara, and N. Ibaraki. IEEE Transactions on Electronics, vol. E86C, pp. 2269-2274, 2003.
- [4] J. Huang, P.F. Miller, J.S. Wilson, A. J. de Mello, J.C. de Mello and D.D. Bradley, Adv. Funct. Mater. **15**, 290 (2005)
- [5] E. Vitoratos, S. Sakkopoulos, E. Dalas, N. Patiatsas, D. Karageorgopoulos, F. Petraki, S. Kennou and S.A. Choulis, Organic Electron. **10**, 61 (2009)
- [6] L. B. Groenendaal, F. Jonas, D. Freitag, H. Pielartzik and J.R. Reynolds, Adv. Mater. **12**, 481(2000)
- [7] S. H. Park, A. Roy, S. Beaupré, S. Cho, N. Coates, J. S. Moon, D. Moses, M. Leclerc, K. Lee and A. J. Heeger. Nature Photonics **3**, 297 (2009)
- [8] G. Zotti, S. Zecchin, G. Schiavon, F. Louwet, L. Groenendaal, X. Crispin, W. Salaneck and M. Fahlman, Macromolecule **36**, 3337 (2003)

- [9] K. Gurunathan, A. Vadivel Murugan, R. Marimuthu, U.P. Mulik and D.P. Amalanerkar, *Mater. Chem. Phys.* **61**, 173, (1999)
- [10] A. M. Nardes, R. A. J. Janssen, and M. Kemerink, *Adv. Funct. Mater.* **18**, 865 (2008)
- [11] R. Swanepoel, *J. Phys. E: Sci. Instrum.* **16**, 1214 (1983)
- [12] D. S. Germack, C. K. Chan, R. J. Kline, D. A. Fischer, D. J. Gundlach, M. F. Toney, L. J. Richter, and D. M. DeLongchamp. *Macromolecules*, **43**, 3828 (2010)

Chapter 6

6.1 Conclusions and Future work

Copper nanoparticles are exhibiting plasmonic excitation in the visible, which is the spectral region of interest for their applications in plasmonic solar cells. The work completed in this thesis includes the identification of the parameters that are necessary to obtain solar grade copper nanoparticles by radio frequency sputtering. By optimizing the sputter growth parameters, we determined the conditions that led to the deposition of np-Cu's with suitable size and optimal substrate area coverage. Increasing the sputtering power benefits the sputtering efficiency, but with limited number of voids between the copper nanoparticles that are interconnected. The spectral maximum of the transmittance enhancement peak is therefore not significantly affected by varying the radio frequency power. However, both the plasma pressure and the substrate biasing voltage proved useful in controlling the degree of dispersion of the particles and, hence, the spectral position of the transmittance enhancement peak. The observed spectral position increased with increasing bias voltage from 547 nm – 562 nm.

Since as-grown copper nanoparticles were interconnected, it was important to consider the effect of thermal treatment in promoting their isolation. It was observed that particle migration and coalescence enhanced the formation of isolated particles. Resonant excitation of plasmon modes is dependent on the nanoparticle size and the degree of isolation as seen for thermally annealed copper nanoparticles. Previous investigations reported surface plasmon absorption in copper nanoparticles in the 553 nm – 576 nm spectral range. In our case, plasmon resonance excitation spans from 553 nm to 608 nm. This has been assigned to the broad distribution of copper nanoparticles that can be obtained our method. The distribution of the particles follows very closely a Gaussian distribution function.

By using collection mode (x, z) SNOM images, we observed the intensity of scattered light at different height from the np-Cu surface. Bright and dark regions corresponding to the enhancement and depletion of the scattered light intensity were obtained and mapped. No enhancement was observed at a distance less than 200 nm from the bare np-Cu surface. This position is too far away from the nanoparticles for enabling plasmonic enhancement in thin film solar cells and would lead to poor performance of these devices. However, np-Cu/SiO₂ composites obtained by sputtering showed an extended electromagnetic field enhancement in the

vicinity of the sample surface. Such observation leads to a new form of architectural design that is required to obtain enhanced performance in plasmonic solar cells.

The results from this work, provides new insight that awaits to be used to improve the performance of thin film cells. Plasmonic organic solar cells incorporating np-Cu's are being constructed and tested in our laboratory.

CURRICULUM VITAE

SABASTINE CHUKWUEMEKA EZUGWU

Education:

2011 – 2012 Western University, Canada

M.Sc. Physics (in view)

2007-2009 University of Nigeria Nsukka, Enugu State, Nigeria

M.Sc. Solar Energy Physics

1999-2004 Federal University of Technology Owerri, Imo state, Nigeria

B. Tech (Hons.) Industrial physics

Referred Proceedings:

- [1] F.I. Ezema, R.U. Osuji, **S.C. Ezugwu**, P.U. Asogwa, A.B.C. Ekwealor, B.A. Ezekoye; *Chemical bath deposition of heterojunction thin films for solar cell application*. International Conference on Photonics, Nanotechnology and Computer Application, India (ICOPNAC 2009), 1, 144-150.
- [2] F.I. Ezema, **S.C. Ezugwu**, S.N. Agbo, A.B.C. Ekwealor, P.U. Asogwa and R.U. Osuji; *Synthesis and characterization of thallium sulphide/cadmium sulphide and lead sulphide/cadmium sulphide thin films grown in a polymer matrix by CBD method*. 24th European Photovoltaic Solar Energy Conference, 21 – 25 September 2009, Hamburg, Germany, 295 – 298 (2009)

Publications:

- [1] **S.C. Ezugwu**, F.I. Ezema, R.U. Osuji, P.U. Asogwa, A.B.C. Ekwealor, B.A. Ezekoye; *Effect of deposition time on the band-gap and optical properties of chemical bath deposited CdNiS thin films*. Optoelectronics and Advanced Materials – Rapid Communications, 3(2), 141 – 144 (2009).
- [2] **S.C. Ezugwu**, F.I. Ezema, R.U. Osuji, P.U. Asogwa, B.A. Ezekoye, A.B.C. Ekwealor, C. Chigbo, M. Anusuya, M. Mahaboob Beevi; *Optical studies of chemically deposited PVA-capped PbS nanoparticle thin films*. Optoelectronics and Advanced Materials – Rapid Communications, 3(6), 528 – 532 (2009)

- [3] **S.C. Ezugwu**, P.U. Asogwa and F.I. Ezema; *Structural and optical characterization of PVP-capped lead oxide nanocrystalline thin films*. Journal of Optoelectronics and Advanced Materials, 12(8), 1765 – 1771 (2010).
- [4] **S.C. Ezugwu**, F.I. Ezema and P.U. Asogwa; *Synthesis and characterization of ternary CuSbS₂ thin films: effect of deposition time*. Chalcogenide Letters, 7(5), (369 – 376) 2010
- [5] **S.C. Ezugwu**, F.I. Ezema and P.U. Asogwa; *Effects of deposition time on the structural and optical properties of ZnO thin films by aqueous chemical growth technique*. Digest Journal of Nanomaterials and Biostructures, 6(3), 1301 – 1310 (2011).
- [6] **S.C. Ezugwu**, M.S. Ahmed, R. Bauld, R. Divigalpitiya and G. Fanchini; *Influence of the addition of graphene-based materials on the thermophysical properties of Poly(3,4-ethylenedioxythiophene):poly(styrenesulfonate) thin film nanocomposites* (under review in Thin Solid Films) 2012.
- [7] **S.C. Ezugwu**, G. Fanchini and R. Divigalpitiya; *Carbon coated articles and methods for making the same* (provisional US patent application no. 69590US002) 2012.
- [8] M.S. Ahmed, **S.C. Ezugwu**, R. Divigalpitiya and G. Fanchini; *Relationship between electrical and thermal conductivity in graphene-based transparent and conducting thin films* (under review in Carbon) 2012.
- [9] **S.C. Ezugwu** and G. Fanchini; *Fabrication of copper nanoparticles by radio frequency sputtering for plasmonic photovoltaic applications* (in progress).

Related work experience:

2008 - 2009: Physics Demonstrator, University of Nigeria, Nsukka.

2011 – 2012: Graduate Teaching Assistant, Western University Canada

Professional Membership

Nigerian Institute of Physics